

June 4, 2004

Interaction Dynamics of Singular Wave Fronts

Darryl D. Holm^{1,2} and Martin F. Staley¹

¹Theoretical Division

Los Alamos National Laboratory, MS B284

Los Alamos, NM 87545

email: dholm@lanl.gov

email: staley@lanl.gov

²Mathematics Department

Imperial College London

SW7 2AZ, UK

email: d.holm@imperial.ac.uk

Abstract

Some of the most impressive singular wave fronts seen in Nature are the transbasin oceanic internal waves, which may be observed from the Space Shuttle as they propagate and interact with each other, for example, in the South China Sea. The characteristic feature of these strongly nonlinear wavefronts is that they reconnect when two of them collide transversely. We derive the EPDiff equation, and use it to model this phenomenon as elastic collisions between singular wave fronts (solitons) whose momentum is distributed along curves moving in the plane. Numerical methods for EPDiff based on compatible differencing algorithms (CDAs) are used for simulating these collisions among curves. The numerical results show the same nonlinear behavior of wavefront reconnections as that observed for internal waves in the South China Sea. We generalize the singular solutions of EPDiff for other applications, in computational anatomy and in imaging science, where the singular wavefronts are evolving image outlines, whose

momentum may be distributed on surfaces moving through space in *three dimensions*. The key idea is always momentum exchange during collisions of the wavefronts. A suite of 2d and 3d numerical simulations provide collision rules for the wavefront reconnection phenomenon in a variety of scenarios.

Contents

1	Synopsis	3
2	Problem statement, approach, and main results	7
3	Preview of numerical results	16
3.1	CFD methods for fluid singularities	16
3.2	Numerical approach	17
3.3	Interaction dynamics of contacts	18
4	History of modeling internal wave fronts	26
5	Nonhydrostatic multilayer columnar motion (MLCM) equations	29
5.1	Implications of the columnar motion ansatz	29
5.2	Variational derivatives of the Lagrangian	31
5.3	Euler-Poincaré motion equation for MLCM	32
6	Weakly nonlinear limit equations	36
6.1	EP derivation of Boussinesq-like equations	36
6.2	Other weakly nonlinear EP equations	38
7	Kinetic energy Lagrangians and the EPDiff geodesic equation	39
7.1	Kinetic energy Lagrangians	39
7.2	Momentum maps for singular solutions of EPDiff	41
8	Numerical approach	42
9	Numerical results for EPDiff in 2d	46
9.1	Plate	47
9.2	Parallel	50

9.3	Skew	55
9.4	Wedge	61
9.5	Head-on	67
9.6	Star	72
9.7	Rotate	72
9.8	Right	83
9.9	Inout	89
9.10	Time reversal	99
10	Numerical results for EPDiff in 3d	99
10.1	Plate	101
10.2	Parallel	102
10.3	Skew	107
10.4	Wedge	107
10.5	Head-on	107
10.6	Rotate	112
10.7	Right	112
10.8	Inout	117
10.9	Wheel	117
10.10	Wheels	124
10.11	Torus	124
10.12	Tori	124
10.13	Time reversal	131
11	Conclusions, future directions, and outstanding problems	131

1 Synopsis

Space Shuttle observations show great lines in the sea, which show up in Synthetic Aperture Radar (SAR) images as in Figure 1. These are internal waves, whose fronts appear in SAR images as unbroken curves extending for hundreds of kilometers. For example, tidal flows and undulations of the Japanese Current in the region of the Luzon Strait between Taiwan and the Philippines generate internal wavefronts which are well over one hundred kilometers in length and which propagate westward for hundreds of kilometers all the way across the South China Sea. These wave fronts show strong coherence and possess the characteristic feature of reconnecting with each other whenever

any two of them intersect transversely. This reconnection is the hallmark of a nonlinear process. Weaker waves may intersect, but not reconnect. We seek to encode the motion of these internal wave fronts and their collision rules mathematically in a minimal PDE (partial differential equation) model, and to investigate these wave front reconnections in numerical simulations of the model. Establishing a simplified PDE model whose solutions encode the motion of these internal wave fronts and their collision rules will enable understanding the effects of the nonhydrostatic processes that govern them, without requiring the full numerical simulation and analysis of the 3d fluid motion equations.

We shall also derive more detailed PDE models for the interactions of these nonlinear wavefronts when topography and boundaries are also included. However, we shall defer developing the numerical methods needed to deal with these additional effects until elsewhere.

Our derivation of the 2d multilayer Euler-Poincaré (EP) equations begins by vertically integrating the variational principle for Euler's equations in 3d. These 2d equations must be nonhydrostatic, because the wave fronts they model possess strong horizontal gradients of vertical acceleration. These nonhydrostatic terms are included in a hierarchy of EP equations which is derived by making a series of simplifying approximations in the exact variational principle. The resulting multilayer 2d equations preserve the EP properties of energy balance, circulation laws and potential vorticity (PV) conservation. PV analysis in a multilayer fluid system is essential for assessing its baroclinic instability [49]. However, PV for wave fronts is a new concept, whose implications are hardly understood yet. We will show that the new hierarchy of EP equations recovers a sequence of previously known models of internal wave dynamics when specialized in various ways.

Next, from the full hierarchy we extract a simple, minimal PDE description, called EPDiff, which models internal wave fronts as delta functions of momentum distributed on moving curves in the plane. This corresponds to modeling internal wave fronts as contact discontinuities in velocity. EPDiff thus explains the creation and stability of wave fronts as the development of singular momentum solutions from continuous velocity distributions in a PDE initial value problem (IVP). This description links the shape of the wavefront velocity profiles to the Green's function associated with the non-local relation in the PDE between its singular momentum and its continuous

velocity. Hence, EPDiff explains the uniform width of the wave front velocity profiles that is observed in internal wave trains. Namely, the momentum of the wavefront is concentrated on delta functions supported on the curved evolving wavefronts. The corresponding velocity profile is then obtained via a Green's function relation between wave momentum and fluid velocity. This minimal description of internal wave fronts as singular momentum solutions of the evolutionary equation EPDiff encompasses their reconnections and provides the geometric mechanism underlying their propagation and collision interactions. In 1d, these collisions are understood as elastic soliton collisions, whose solutions are obtained by the inverse scattering transform (IST) for an associated isospectral linear eigenvalue problem. As far as we know, the machinery of IST is not available in higher spatial dimensions for EPDiff. However, the elastic scattering interactions seen in its wavefront solutions in 2d (and in 3d) are explained by another geometric mechanism. As we shall explain, this geometric mechanism for propagation and collisions turns out to be Hamiltonian geodesic flow on the time-dependent smooth maps (diffeomorphisms), defined with respect to the kinetic energy metric that also determines the wave profile.

To solve the EPDiff equation, we develop a numerical method called the compatible differencing algorithm (CDA) that is able to capture the collisions among these weak solutions of EPDiff, and we characterize the wave front interactions we observed numerically in a variety of scenarios.

In summary, we use EP variational theory to derive the EPDiff equation, whose solution shows singular wave fronts, and we use new CDAs for its numerical simulations. EPDiff is the first mathematical explanation of the observed 2d internal wave front reconnections.

Geometric setting. We have found that modeling the reconnection process in internal wave front dynamics requires a class of PDEs that are both nonlinear and nonlocal. EPDiff is not exactly a hyperbolic equation. It has a characteristic velocity, but the relation its EP variational principle defines between the fluid's velocity and momentum in Newton's Law is nonlocal. That is, the fluid's velocity is determined from its momentum by solving an elliptic equation. Physically, the elliptic equation arises from nonhydrostatic processes that cause linear, or nonlinear, dispersion or focusing. This

nonlocal relationship between velocity and momentum is reminiscent of the Biot-Savart relationship between velocity and vorticity. However, like solitons, internal wave fronts carry momentum and inertia, while fluid vortices do not.

Our work has some close similarities with soliton theory and some important differences from it. The Korteweg-de Vries (KdV) equation at linear order in the asymptotic expansion for shallow water waves and the Camassa-Holm (CH) equation at quadratic order are both soliton equations, and they are both associated with geodesic flow [33, 34, 47]. That is, they each make optimal use of their kinetic energy, which provides a norm for their velocity. The EPDiff equation has this same characteristic. Moreover, the singular solution ansatz for the geodesic flow of momentum associated with the EPDiff equation which we discuss below turns out to be a momentum map, as discovered in Holm and Marsden [22]. The momentum map property of these singular solutions means they comprise an invariant manifold, preserved by the flow of EPDiff. This property allows us to reduce the dimension of the wave front interactions to an invariant manifold of singular momentum solutions of EPDiff. These solutions describe the observed propagation and reconnection phenomena of the wave fronts, but they have no internal degrees of freedom, and thus they have no mechanism for wave breaking to occur.

In this paper, we model internal wave fronts as contact discontinuities in velocity, whose motion is governed by applying time-dependent smooth maps which act on the curves in the plane that outline the wave fronts and specify their momentum vectors at points along these curves. The motion of the internal wave fronts is governed by the EPDiff equation. This equation is the condition for the smooth maps that act on these curves to evolve by geodesic flow, with respect to a metric determined by their kinetic energy, which also determines the functional form of their wave profile. The wave front motion may thus be determined numerically as an initial value problem by solving the EPDiff equation.

In such a strongly geometric setting, we expect that combining finite element methods and discrete exterior calculus may provide future improvements in both modeling and simulations, by providing a useful setting for integration of the analysis with the numerics in the description of internal

wave fronts as singular weak solutions, or limiting solutions (contacts) for nonlinear, nonlocal PDEs. However, we defer the full use of discrete exterior calculus methods for numerically solving EPDiff until these methods have been further developed. See [19, 35] for introductions to these methods.

Outline of the paper. Mathematical modeling problems for internal wave fronts, and our approaches to solving them, are summarized in Section 2. A preview of our numerical results appears in Section 3. Previous work in multilayer descriptions of internal waves is reviewed in Section 4. The columnar motion ansatz for multilayer fluids is explained in Section 5, and is used there to derive the nonhydrostatic 2d MultiLayer Columnar Motion (MLCM) equations and their natural boundary conditions. A series of weakly nonlinear approximations is introduced into the EP variational principle for the MLCM equations in Section 6. The resulting weakly nonlinear 2d multilayer equations are also compared to the 1d multilayer equations of Choi and Camassa [11] and others. In Section 7, we derive the EPDiff geodesic equation by neglecting dispersion due to potential energy. Singular solutions of EPDiff and their canonical dynamics in the Lagrangian fluid representation are also introduced in Section 7.

The main numerical results of this paper are given in Sections 8, 9 and 10. Section 8 describes our numerical approach using compatible differencing algorithms. Section 9 provides a large suite of numerical simulations investigating the collision rules for the interactions of wave-front solutions of EPDiff in 2d. Section 10 extends our numerical solutions of EPDiff to 3d, and shows that its stable codimension-one singular solution behavior persists in higher dimensions. Finally, we discuss conclusions, future directions and remaining outstanding problems for internal wavefront interactions in Section 11.

2 Problem statement, approach, and main results

Space Shuttle observations of the South China Sea surface show a sequence of large amplitude internal waves at basin scale moving westward after being created by tides and currents running through the Luzon Strait on the eastern side of the basin. These internal waves appear in Synthetic Aperture Radar (SAR) images as long, slightly curved, internal wave fronts 100-200 *km* in

length and separated by 50-80 *km*. When these isolated internal wave fronts sweep across Dongsha Atoll in the middle of the South China Sea, they are perturbed and subsequently re-radiated as two sets of wave front trains propagating westward, each with greater curvature than the incoming wave front. The SAR images of this process are shown in Figure 1. The transverse interactions of the re-radiated wave fronts are so strong that they reconnect, rather than pass through each other. This reconnection is shown in Figure 2. The reconnection phenomenon for nonlinear internal wave fronts in the ocean indicates transfer of momentum and is one of the primary motivations of the present study. Internal wave interactions have been well studied in one dimension, often by using the weakly nonlinear Boussinesq approximation, usually resulting in a variant of the Korteweg-de Vries (KdV) equation and its soliton solutions [51]. However, the complex wave front interactions shown in Figures 1 and 2 are plainly two dimensional. Moreover, their reconnection is not captured by the 2d extension of KdV for weakly nonlinear waves with slow transverse variations, known as the Kadomsev-Petviashvili (KP) equation. (The KP equation assumes weak gradients in the direction transverse to propagation. However, this assumption does not hold during the wavefront reconnections we seek to model.) Thus, we begin our study of internal wave front reconnection by developing a new set of equations that extends, to multilayer fluids in two dimensions, the Su-Gardner [50] or Green-Naghdi [18] equations for fully nonlinear waves on the free surface of a single-layer fluid in one dimension. Related earlier derivations of one dimensional equations for multilayer fluids appear in [11, 38, 39].

Our approach to developing these equations takes advantage of the Euler-Poincaré (EP) theory of Hamilton’s variational principle for ideal fluids, in the Eulerian representation [23], expressed as $\delta S = 0$ with $S = \int \ell(\mathbf{u}) dt$ for Eulerian horizontal fluid velocity \mathbf{u} . The advantage of the EP approach for our present purpose is that it provides a hierarchy of equations at various levels of approximation that preserves the EP mathematical structure of the highest level theory. This approach enables us to strike the appropriate balance between accuracy and computational tractability, by choosing the appropriate level in the hierarchy of approximations. The symmetries of the EP variational principle at each level then endow its resulting evolutionary equations with conservation laws via the Kelvin-Noether theorem [23]. For example, Kelvin’s circulation theorem for the multilayer fluid theory in 2d leads to local conservation of potential vorticity (PV) in each fluid layer, even though these layers are strongly coupled.

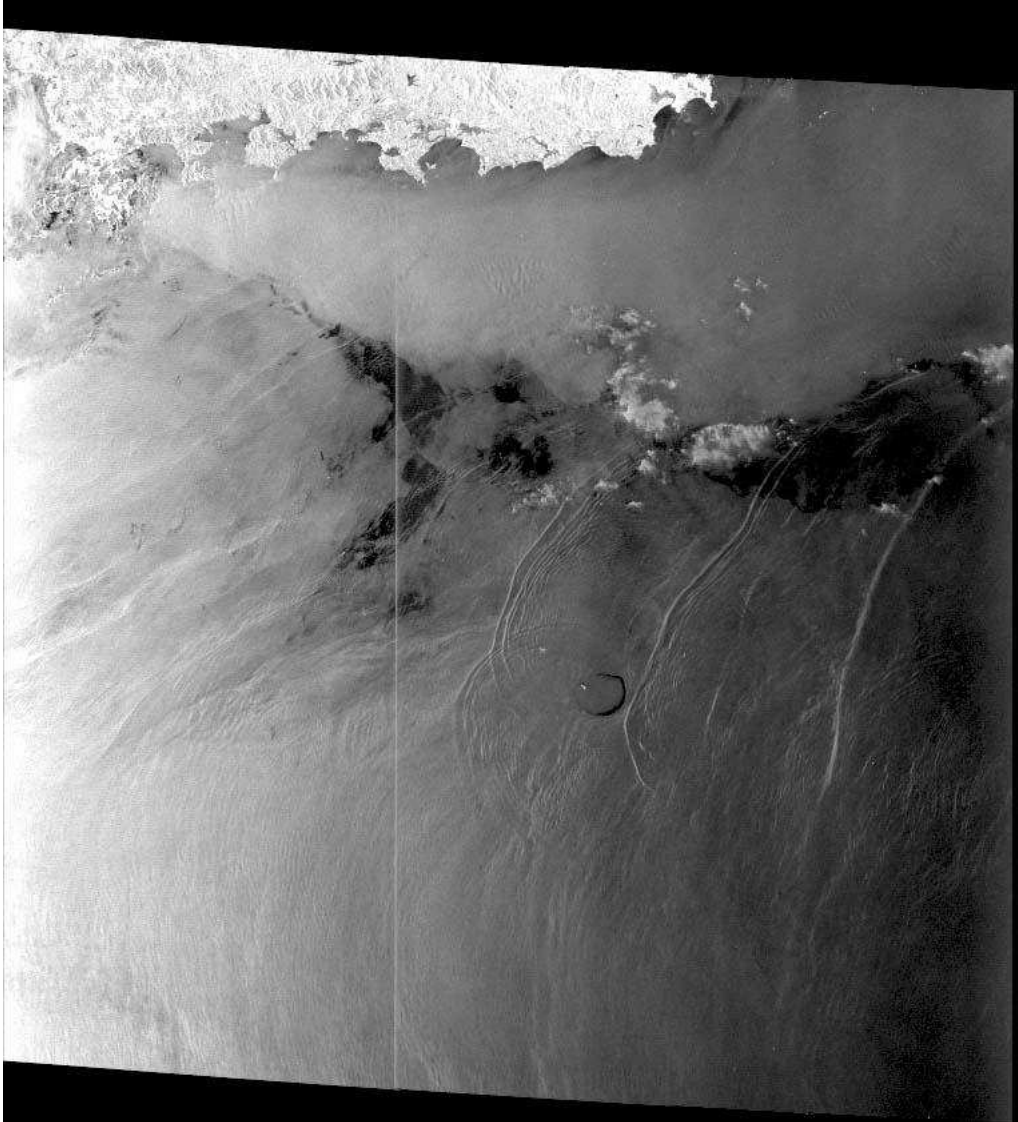


Figure 1: Synthetic Aperture Radar (SAR) images of the South China Sea surface taken from the Space Shuttle show a sequence of large amplitude internal waves at basin scale. These wave fronts are moving westward after being created by tides and currents running through the Luzon Strait on the eastern side of the basin. These wave fronts encounter the Dongsha Atoll in the center of the basin and re-emerge after colliding with it.

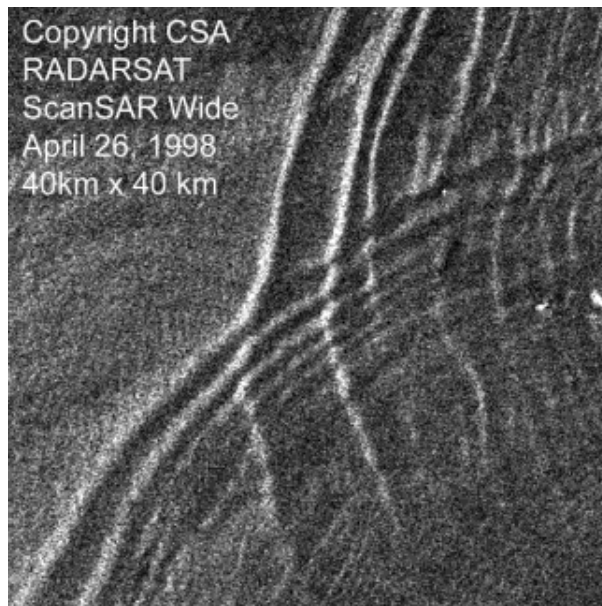


Figure 2: The transverse interactions of the wave fronts re-emerging from their encounter with the Dongsha Atoll are so strong that the wave fronts reconnect, rather than pass through each other. This indicates transfer of momentum.

The starting point in the derivation of these equations is the assumption of columnar motion; so that the horizontal velocity in each layer is independent of the vertical coordinate. We explain how substituting this columnarity into the EP Hamilton's principle for multilayer fluids reduces their description from 3d to 2d, and results in a hierarchy of equations which arises when a sequence of further approximations are introduced into Hamilton's principle in the EP framework.

The common features of the equations in this hierarchy are (1) they express Newton's Law for the evolution of momentum in the Eulerian fluid representation; (2) their nonlinearity involves both momentum and fluid velocity; and (3) their momentum and fluid velocity satisfy a nonlocal relationship, which must be solved by inversion of an elliptic operator at each time step. While keeping these features, we simplify the description by making a series of approximations in Hamilton's principle, until we finally arrive at a minimal description which still captures the wave front reconnection phenomenon. We then employ this minimal description to investigate and classify the wave front interactions analytically and in numerical simulations. Our application is for internal wave fronts, which we compare with our numerical simulations in two dimensions. In a further developmental step, we also consider numerical solutions of our description in three dimensions. As mentioned earlier, this 3d extension yields singular solutions of EPDiff whose momentum is defined on contact surfaces.

The EPDiff equation and its weak wavefront solutions. The EP equation at which we eventually arrive by this sequence of variational approximations is the following evolutionary integral-partial differential equation, expressed in vector form as [28, 22],

$$\frac{\partial}{\partial t} \mathbf{m} + \mathbf{u} \cdot \nabla \mathbf{m} + \nabla \mathbf{u}^T \cdot \mathbf{m} + \mathbf{m}(\operatorname{div} \mathbf{u}) = 0, \quad \text{with} \quad \mathbf{m} = \mathbf{u} - \alpha^2 \Delta \mathbf{u}, \quad (1)$$

for which we assume periodic boundary conditions. This is the EPDiff equation, for "Euler-Poincaré equation on the diffeomorphisms," where \mathbf{m} and \mathbf{u} are vectors, $\partial_t \mathbf{m}$ denotes the time derivative of \mathbf{m} , and α is a constant parameter with dimensions of length. EPDiff is the n -dimensional version of the 1d shallow water equation introduced in [6]. EPDiff arises from a variational principle based on the fundamental dynamical properties of fluids. Mathematically, EPDiff describes *geodesic* motion on the diffeomorphism group

with respect to $\|\mathbf{u}\|_{H^1}^2$, the H^1 norm of the fluid velocity, which is the kinetic energy of this vertically averaged model fluid [23].

The EPDiff equation (1) may be written equivalently as *differential Riemann invariance*; namely, as invariance of the momentum one-form density along the fluid velocity characteristics. That is,

$$\frac{d}{dt}(\mathbf{m} \cdot d\mathbf{x} \otimes dVol) = 0, \quad \text{along} \quad \frac{d\mathbf{x}}{dt} = \mathbf{u} \equiv G * \mathbf{m}, \quad (2)$$

where $\mathbf{u} = G * \mathbf{m}$ denotes convolution of the momentum \mathbf{m} with the Green's function G to produce the fluid velocity \mathbf{u} . This convolution is the elliptic-solve step in the determination of the fluid's velocity from its momentum for this class of equations. This property is the nonlocal relationship mentioned above. In the particular case of EPDiff, we use the elliptic Helmholtz operator in $\mathbf{m} = \mathbf{u} - \alpha^2 \Delta \mathbf{u}$, with length scale α . The Helmholtz operator relationship between velocity \mathbf{u} and momentum \mathbf{m} is derived in Section 5 for strongly nonlinear columnar motion of shallow water.

The relation of EPDiff to 1d soliton equations. In 1d, EPDiff becomes

$$\partial_t m + m \partial_x u + \partial_x(mu) = 0, \quad \text{with} \quad m = u - \alpha^2 \partial_x^2 u.$$

This is the dispersionless limit of the Camassa-Holm (CH) equation

$$\partial_t m + m \partial_x u + \partial_x(mu) = -c_0 \partial_x u - \Gamma \partial_x^3 u, \quad \text{with} \quad m = u - \alpha^2 \partial_x^2 u,$$

which is a completely integrable soliton equation [6]. The CH equation reduces to the familiar KdV equation when $\alpha^2 \rightarrow 0$.

EPDiff in 1d with viscosity ν is expressed as

$$\partial_t m + m \partial_x u + \partial_x(mu) = \nu \partial_x^2 m, \quad \text{with} \quad m = u - \alpha^2 \partial_x^2 u.$$

When $\alpha^2 \rightarrow 0$ this becomes the well known Burgers equation,

$$\partial_t u + \partial_x\left(\frac{3}{2}u^2\right) = \nu \partial_x^2 u.$$

The Burgers equation is hyperbolic and supports weak solutions (shocks) in the limit $\nu \rightarrow 0$.

EPDiff is a new departure for nonlinear hyperbolic equations. It is conservative in the absence of viscosity and it may then be written in Riemann

invariant form (2). However, it is nonlocal, because obtaining its characteristic velocity \mathbf{u} from its momentum \mathbf{m} by inverting the Helmholtz operator via $\mathbf{u} = G * \mathbf{m}$ requires an elliptic solve at each time step when $\alpha \neq 0$. Our analysis [28, 22] shows that EPDiff has interesting and unusual solution properties which are only beginning to be studied. The properties of its solutions will provide great challenges for analysis and numerics.

Singular momentum solutions of EPDiff. For example, EPDiff has weak *singular momentum solutions* that are expressed as [28, 22],

$$\mathbf{m}(\mathbf{x}, t) = \sum_{a=1}^N \int_{S_a} \mathbf{P}_a(t, S_a) \delta(\mathbf{x} - \mathbf{Q}_a(t, S_a)) dS_a, \quad (3)$$

where S_a is a Lagrangian coordinate defined along a set of curves in the plane by the equations $\mathbf{x} = \mathbf{Q}_a(t, S_a)$ supported on the delta functions in the EPDiff solution (3). Thus, the singular momentum solutions of EPDiff are vector valued curves representing evolving wave fronts defined by the Lagrange-to-Euler map (3) for their momentum.

The Green's function for the Helmholtz operator relates the fluid velocity to the momentum in EPDiff (1). Thus, substituting the defining relation $\mathbf{u} \equiv G * \mathbf{m}$ into the singular momentum solution (3) yields the velocity representation for the wave fronts as another superposition of integrals,

$$\mathbf{u}(\mathbf{x}, t) = \sum_{a=1}^N \int_{S_a} \mathbf{P}_a(t, S_a) G(\mathbf{x}, \mathbf{Q}_a(t, S_a)) dS_a. \quad (4)$$

The Green's function G for the second order Helmholtz operator in this expression has a discontinuity in slope across each Lagrangian curve moving with the velocity of the flow. Being discontinuities in the gradient of velocity that move along with the flow, these singular solutions for the velocity at the wave fronts are classified as *contact discontinuities* in the fluid.

Thus, the weak solutions of EPDiff are contacts, rather than shocks. This behavior challenges numerics and leads to a wide range of potential physical applications. In addition to describing internal wave fronts, the EPDiff equation describes the interaction of contacts in a variety of other situations ranging from solitons [6] to turbulence [9, 16] to computational anatomy [27, 46]. The EPDiff fluid dynamics equation in (1) describes the limiting (pressureless) cases of *all* of these applications.

Relation between contact solutions of EPDiff and solitons. The EPDiff singular solutions (4) for the velocities of the internal wave fronts represent the third of the three known types of fluid singularities: shocks, vortices and contacts. The key feature of these contacts is that they carry momentum; so the wave front interactions they represent are *collisions*, in which momentum is exchanged. This is very reminiscent of the soliton paradigm in one dimension. Indeed, in one dimension the singular solutions (4) of EPDiff are true solitons that undergo elastic collisions and are solvable by the inverse scattering transform for an isospectral eigenvalue problem [6].

Applications of EPDiff in turbulence. Lagrangian averaging is a promising approach in turbulence closure modeling. This approach has the advantage that Lagrangian averaging commutes with the advective time derivative in fluid mechanics. Thus, Lagrangian averaging preserves the vorticity stretching process in the resulting approximate equations. For example, after Lagrangian averaging the Navier-Stokes equation and using Taylor's hypothesis that the fluctuations move with the mean flow, one finds the following turbulence closure model [9],

$$\begin{aligned} \frac{\partial}{\partial t} \mathbf{v} + \mathbf{u} \cdot \nabla \mathbf{v} + \nabla \mathbf{u}^T \cdot \mathbf{v} + \nabla p &= \nu \Delta \mathbf{v} + \mathbf{F}, \\ \text{with } \mathbf{v} &= \mathbf{u} - \alpha^2 \Delta \mathbf{u} \quad \text{and} \quad \nabla \cdot \mathbf{u} = 0. \end{aligned} \quad (5)$$

These are the equations of the Lagrangian averaged Navier-Stokes alpha (LANS-alpha) model of turbulence, whose properties are reviewed, for example, in [16]. EPDiff (1) is recovered from the LANS-alpha equations (5) when the constraint of incompressibility ($\nabla \cdot \mathbf{u} = 0$) is relaxed (so that pressure gradient ∇p may be dropped), and the viscous and forcing terms on the right hand side are absent. Thus, these equations possess the following analogy: EPDiff is to LANS-alpha, as Burgers is to Navier-Stokes. Namely, Burgers is a simplified model of compressible Navier-Stokes which allows shocks as singular solutions of its initial value problem, when \mathbf{F} is absent and $\nu \rightarrow 0$; and EPDiff is a simplified model of compressible LANS-alpha which allows contact discontinuities as singular solutions of its initial value problem, when \mathbf{F} is absent and $\nu \rightarrow 0$. The reduction of the singular solutions from Burgers shocks to EPDiff contacts is a result of the Lagrangian averaging process, which tempers the nonlinearity in the Navier-Stokes equations.

Applications of EPDiff in computational anatomy. Applications of EPDiff (1) in computational image science (CIS) focus on computational anatomy, based on pattern matching algorithms and smooth morphing of planar figure outlines, called templates. For a review of this approach, see [46]. An interesting objective of this CIS application is to reconstruct a 3d map of the brain in the spatial region between two parallel 2d PET Scans. In this application, the figure outlines are contact curves, which form a finite-dimensional invariant manifold of EPDiff, as in equation (3). A 3d brain map is constructed by treating two 2d PET scans in parallel planes as initial and final conditions, and then flowing by EPDiff to interpolate in the 3d region between them as an optimization problem. The 2d solution for the contact curves evolving by EPDiff smoothly reconstructs the outlines of the PET scan images on any parallel plane between them. The EPDiff contact interactions also allow reconnection of planar outlines, corresponding to changes of topology in planar sections of the 3d object being imaged [27]. The representation (3) of the singular momentum solutions of EPDiff encodes the image contours for this application.

Importantly, the momentum representation of the image contours (3) is complete and nonredundant (one-to-one). Another advantage of the momentum representation of image contours as singular solutions of EPDiff is that this representation is *linear* in nature, being dual to the velocity vectors. Thus, linear combinations of either velocity fields, or momenta are meaningful mathematically and physically, provided they are applied to the same template [27]. This means the average of a collection of momenta, of their principal components, or time derivatives of momenta at a fixed template are all well-defined quantities. The linearity the momentum representation also allows for example the statistics of an ensemble of images to be analyzed, or the results of adding noise to the image outlines to be computed using EPDiff. All of these advantages of the singular momentum representation for 2d images also apply in the corresponding representation of 3d images. Evolution of singular momentum solutions of EPDiff as surfaces in 3d corresponding in medical imaging to growth, or changes in 3d shape with time. The last part of this paper will deal with the computation of 3d solutions of EPDiff.

Summary of the analytical approach. The rich array of possible applications of EPDiff motivates our investigation of its initial value problems

in 1d, 2d and 3d. The paradigm raised in our analysis of internal wave front interactions is the generalization of soliton collisions from 1d to 2d. The class of shallow water equations we derive and study in 2d has a sequence of simplifications that yield two dimensional generalizations of all the weakly nonlinear shallow water equations that have historically been used to study solitons and solitary waves in one dimension. We first argue that by using the highest, most accurate level of the fully nonlinear description in 2d, one should be able to reproduce the observed phenomenon of wave front reconnection observed for internal waves in the South China Sea. We then simplify the description by stages until we finally arrive at EPDiff (1) in 2d, while preserving what we believe is the key feature responsible for this wave front reconnection phenomenon – its momentum transfer during collisions. Because of its other potential applications, particularly its linear encoding of information for imaging science as momentum, we also consider the initial value problem for 3d singular solutions of EPDiff. Its imaging science applications are envisioned as optimization problems. However, the first step in understanding the role of momentum exchange for EPDiff in imaging science is the solution of its initial value problem for the emergence of its singular momentum solutions in 2d and 3d.

Brief sketch of the paper. The first few sections of this paper motivate using the much simpler equation EPDiff (1), whose properties we study analytically and numerically in later sections, as a simplified but realistic model of wave front interactions of nonlinear internal waves in the ocean. The last few sections present numerical results for EPDiff in both 2d and 3d, which we now preview.

3 Preview of numerical results

3.1 CFD methods for fluid singularities

Shocks, vortices and contacts are a compressible fluid's singular nonlinear responses to strong applied forces. Capturing these singular responses accurately has always been the grand challenge of computational fluid dynamics (CFD). Shocks move *through* the flow and carry inertia. Vortices move *with* the flow, but they have no inertia. Contacts are discontinuities in the derivatives of velocity and density that, like vortices, move with the fluid

flow, and which *do* have inertia. Consequently, it makes dynamical sense to speak of momentum exchange in contact-contact collisions. Today, various CFD methods exist that accurately capture shocks and vortices. However, considerably less is known about designing numerical methods for capturing contacts and characterizing their nonlinear interactions, especially in higher dimensions, when vorticity is present.

One might consider Lagrangian numerical methods as an obvious approach, because contact discontinuities move with the flow. However, for head-on contact collisions, parallel studies showed that the Lagrangian approach suffers in comparison to compatible differencing algorithms (CDAs) that we apply here in the Eulerian framework. In particular, the head-on collision of oppositely moving contacts produces an elastic bounce seen in the weak solution of EPDiff as a mutual annihilation and recreation of generalized functions, but only the annihilation was captured well by Lagrangian methods in the parallel studies [37]. In the future, we may also consider developing new methods for EPDiff based on discrete exterior calculus (DEC) [19, 35].

3.2 Numerical approach

The second half of this paper numerically investigates and classifies the EPDiff dynamics of contact interactions in various cases of its initial value problem. This is accomplished by applying compatible differencing algorithms to EPDiff in both 2d and 3d. One reason for choosing CDAs as the preferred simulation method is that the EPDiff equation (1) may be rewritten as

$$\frac{\partial}{\partial t} \mathbf{m} - \mathbf{u} \times \operatorname{curl} \mathbf{m} + \operatorname{grad}(\mathbf{u} \cdot \mathbf{m}) + \mathbf{m}(\operatorname{div} \mathbf{u}) = 0. \quad (6)$$

This equation contains the divergence, gradient and curl operators, whose identities must be treated properly for accurate computations. Preserving these vector calculus identities is the basis of CDAs and is the first fundamental property of discrete exterior calculus. Namely, these identities form the discrete analog of the identity $d^2 = 0$ for the exterior derivative. As mentioned earlier, EPDiff represents geodesic motion, which naturally involves exterior calculus and variational principles. A framework for designing DEC methods with promising potential for simulations of EPDiff has been developed and advanced recently in [19, 35].

3.3 Interaction dynamics of contacts

This paper takes advantage of recent developments in compatible differencing algorithms by applying CDAs to new classes of problems involving contact-contact interaction phenomena. For the report of a recent conference on CDAs, see [32]. We characterize the emergence of contacts from smooth initial velocity distributions, and describe their subsequent evolution, propagation and interaction dynamics. We address dynamical issues for basic interactions among contacts in one, two and three dimensions, as follows.

1d. An integrable shallow water equation whose peaked soliton solutions emerge from a smooth spatially confined initial conditions for velocity.

2d. Interacting contact curve segments in the plane: trains of contact curves emerging from an initially continuous fluid velocity distribution, propagating, and interacting nonlinearly through fundamental collision rules. The 2d collision rules for singular solutions of EPDiff are elucidated by plotting 1d linear sections through the 2d solutions which show their spatial profiles in various directions. The solution behavior along these sections shows the same elastic collision properties and momentum exchange as seen for the 1d peaked soliton solutions (peakons) in 1d for the dispersionless CH equation.

3d. Interacting contact surfaces in space: sheaves of contact surfaces are shown emerging from an initially continuous fluid velocity distribution. We investigate their propagation and interaction by plotting level surfaces of speed, as well as plotting 2d planar slices through these surfaces.

More specifically, we examine dynamical issues for the following basic interactions among the contacts, which are weak solutions of EPDiff, in one, two, and three dimensions.

1d. In 1d, contacts move as points on a line, and EPDiff reduces to the well known dispersionless Camassa-Holm (dCH) equation for shallow water waves, whose contacts are solitons with sharp peaks, or peakons, as shown in the time evolution in Figure 3. The N -peakon problem is known to be completely integrable [6].

2d. In 2d, contacts move as segments of curves in the plane. These EPDiff contacts correspond to oceanic internal waves in one application, or to planar image outlines in another. We shall address the following specific 2d scenarios.

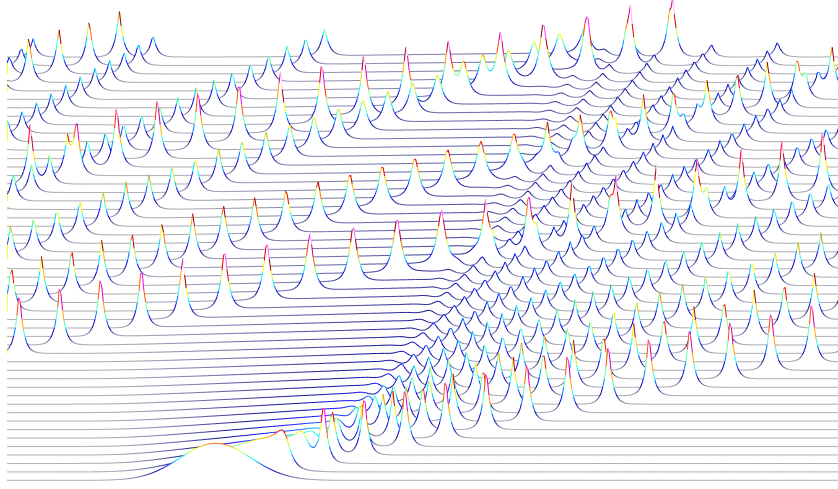


Figure 3: A wave train consisting entirely of peakons emerges in 1d from an initially Gaussian distribution of positive (rightward) velocity.

Evolution and interactions of EPDiff contact segments which are initially straight line segments. Contacts move at the local fluid velocity; so a contact segment must terminate with zero velocity. Hence, an initially straight-line contact segment does not remain straight. Instead, it evolves under EPDiff into a contact curve segment whose length increases, as shown in Figure 4. The speed, $|\mathbf{u}|$, is displayed as colors in this figure, while the bottom panels shows profiles in the east (black), north (dotted red), northeast (green), and southeast (dotted blue) directions through the center of the box. An arrow shows the initial direction of \mathbf{u} . See Section 9 for a fuller description of the contents of the figures.

The transverse collision of two contact curve segments may result in reconnection (merger, or melding) of the curves, which is admitted by the rapid evolution of EPDiff along the directions tangential to the curves. In Figure 5, note the striking similarity between the observed behavior, particularly in the second frame, and the behavior seen in the earlier image of ocean internal waves in Figure 2. We shall investigate the “collision rules” under which such reconnections of wave fronts occur.

We will also consider offset collisions of initially parallel contact segments, as shown in Figure 6. In that figure, notice the recreation (after annihilation) of the portions of the contact curves in the regions where a head-on collision

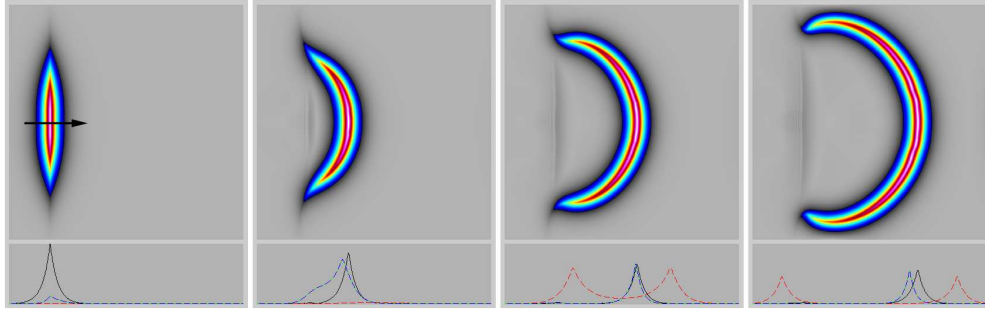


Figure 4: An initially straight, rightward moving peakon segment balloons outward and stretches as it expands in 2d, but keeps its integrity as a single wave front.

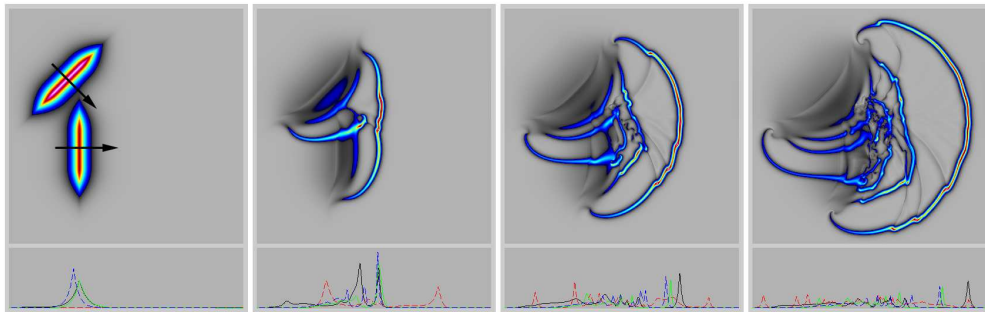


Figure 5: A skew overtaking collision of two peakon segments shows reconnection in which the wavefronts merge repeatedly upon intersecting transversely.

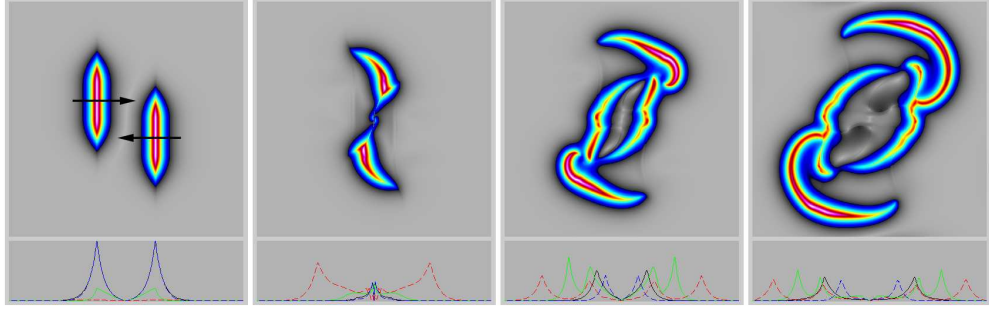


Figure 6: Head-on collisions of peakon segments first annihilate and then recreate their wavefronts.

takes place.

Emergence of contact curve segments from representative classes of smooth initial fluid velocity distributions and their subsequent interactions. For example, consider an initial velocity distribution whose magnitude (speed) is a circular Gaussian ring (annulus) and whose direction is chosen in the following ways.

Uniform translation (broken angular symmetry). This simulation, shown in Figure 7, demonstrates that the initial value problem for EPDiff tends to produce only contact solutions. It also shows the differences in their propagation under convergent (left half of annulus) and divergent (right half of annulus) geometry, and illustrates the exchange of momentum in an overtaking collision. The collision as the rightmost contact curve is overtaken from the left transfers some of the overtaking curve’s momentum forward and causes the rightmost curve to bulge slightly, as seen in the last two frames. (Thus, while momentum is transferred in this collision, the overtaking contact curve does not “pass through” the rightmost contact curve.)

Uniform rotation (preserving angular symmetry). Figure 8 illustrates how the radial and azimuthal components of EPDiff are coupled for radially symmetric solutions. The figure also shows collapse to the origin and reflection back outward, which presents an extreme test of the accuracy of our Cartesian numerical algorithm. The radial collapse and bounce can be computed semi-analytically for comparison, [26].

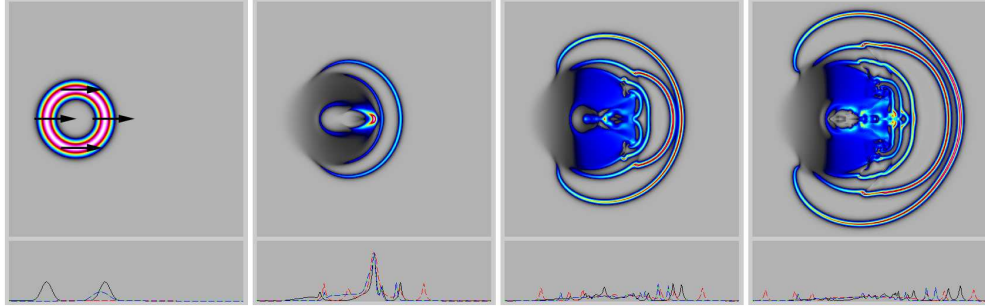


Figure 7: A rightward moving circular Gaussian ring of initial velocity breaks into divergent and convergent contact wave fronts.

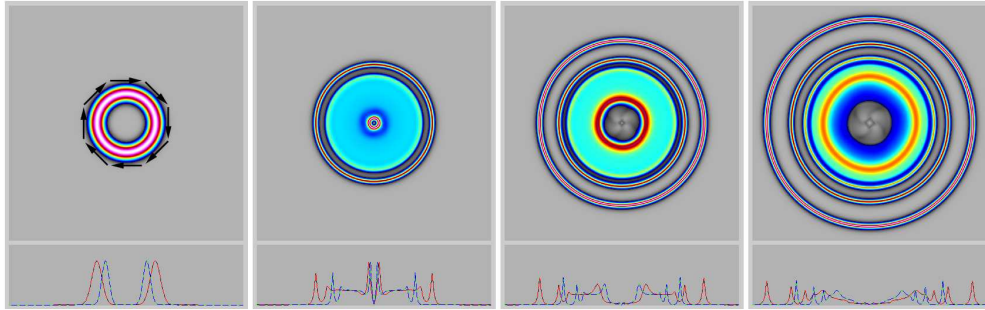


Figure 8: An initially rotating circular Gaussian ring of velocity couples its angular motion to the radial motion of contact wavefronts which propagate both inward and outward. The collapsing circular wavefronts reflect from the center of symmetry.

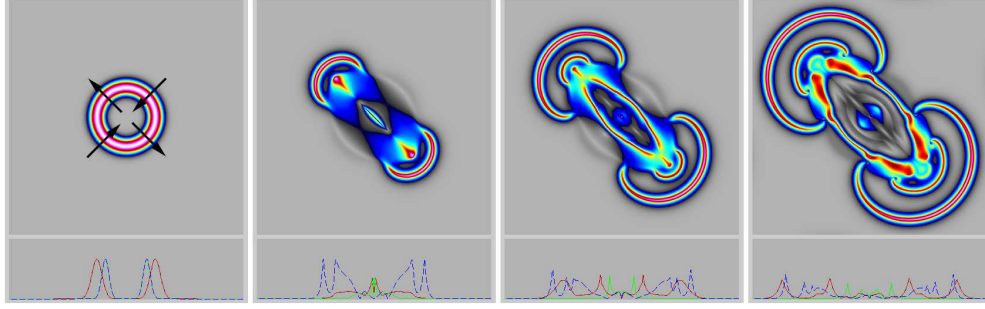


Figure 9: An initially circular Gaussian ring of velocity is diverging along one diagonal and converging along the other. This initial condition breaks into interacting contact wavefronts which propagate outward along one diagonal and converge inward along the other to annihilate and re-emerge, leaving behind a complex mixing flow in the center.

M-fold discrete angular symmetry. Formation of contacts in the outward divergent part of the flow, and the emergence, annihilation, and recreation of contacts collapsing to the diagonal, are all illustrated in Figure 9. This process is typically followed by very complex patterns of mixing flow involving peakon profiles along each 1d section.

3d. In 3d, the initial value problem for EPDiff produces contact surfaces moving through space. The interactions (collisions) of these contact surfaces produce very complex but coherent patterns. In the figures we discuss here, the left, back, and bottom panels of each box show 2d planar slices through the center x (southeast), y (northeast), and z (north) values of $|\mathbf{u}|$. The corresponding planar slices through the level surfaces of $|\mathbf{u}|$ are shown on the side panels of each box. 2d slices that form a plane of symmetry in 3d invariably reflect the behavior of the corresponding 2d problem. We will address the following scenarios in 3d.

Evolution and interactions of contact surfaces that are initially disc-shaped velocity distributions. Initially flat contact surfaces evolve by ballooning into curved contact surfaces, as shown in Figure 10.

Because EPDiff is isotropic, it allows equally rapid evolutions in the directions normal and tangential to the contact surfaces. In particular, its

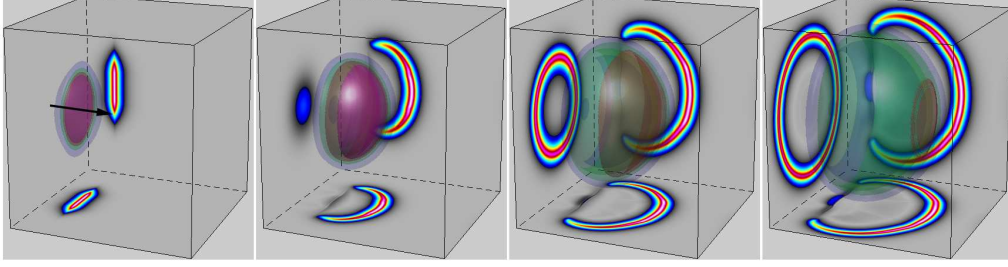


Figure 10: In 3d, an initially rightward moving disc with exponential transverse velocity profile (of correct width α) balloons outward as a contact wavefront which retains its integrity.

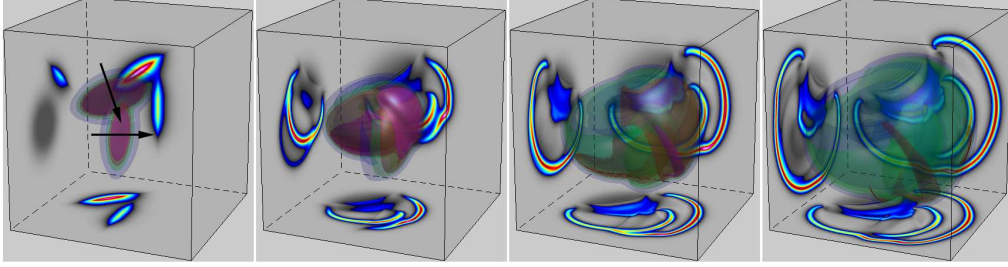


Figure 11: The skew collision of two initially disc-shaped contact wavefronts shows reconnection in 3d.

tangential evolution admits significant stretching. It also allows reconnection of contact surfaces which intersect transversely as they collide. The reconnection is caused by transfer of momentum. This phenomenon is illustrated in Figure 11. We shall investigate the “collision rules” under which such reconnections of surfaces occur.

An offset collision of initially parallel contact surfaces is shown in Figure 12. As in 2d, we observe the recreation (after annihilation) of a contact surface after a head-on collision takes place. Notice also how the outer edges (away from the head-on collision) of the contact surfaces merge to form a ring.

Emergence of contact curve surfaces from representative classes of smooth initial fluid velocity distributions and their subsequent

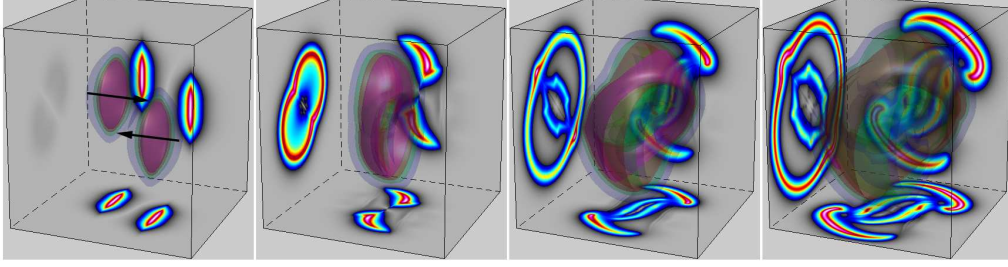


Figure 12: The head-on collision of two initially disc-shaped contact wavefronts shows annihilation and reconnection in 3d.

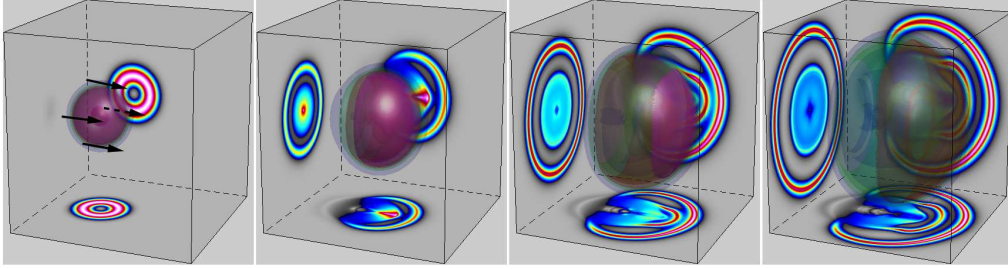


Figure 13: A rightward moving spherical Gaussian shell of initial velocity breaks into divergent and convergent contact wave fronts.

interactions. For example, consider an initial velocity distribution whose magnitude is a radially symmetric Gaussian shell (spherical annulus) and whose direction is chosen in the following ways.

Uniform translation (broken angular symmetry). The simulation shown in Figure 13, as in the corresponding figure for 2d, demonstrates that EPDiff tends to produce only contact solutions, and illustrates the differences in their propagation under convergent (left half of spherical annulus) and divergent (right half of spherical annulus) geometry.

Uniform rotation (preserving angular symmetry about the vertical direction). The frames in Figure 14 show collapse of the spherical contact surfaces to the origin, and their reflection back outward. This shows the coupling between angular and radial motion.

Two-fold discrete angular symmetry. Figure 15 illustrates the formation of contacts for the outward divergent part of the flow and the emergence,

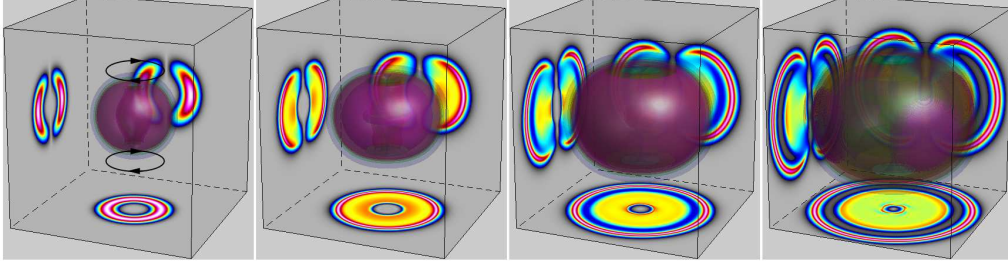


Figure 14: An initially spherical Gaussian shell of velocity rotating about the vertical axis expands outward and collapses inward with cylindrical symmetry, as it breaks into divergent and convergent contact wave fronts.

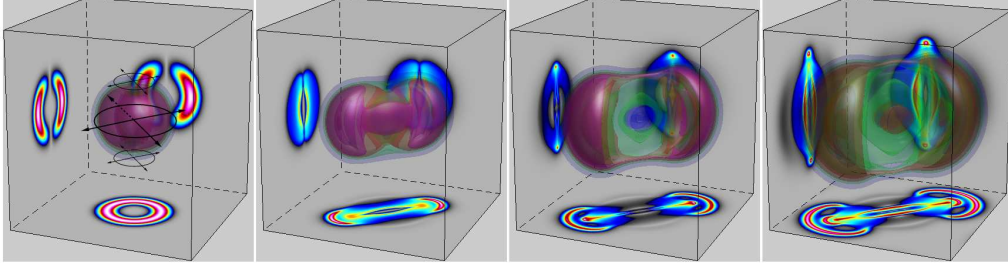


Figure 15: An initially spherical Gaussian shell of velocity diverging in one diagonal vertical plane and converging in the other breaks into interacting contact surfaces.

annihilation and recreation of contacts collapsing along lines of discrete symmetry. The 2d slice through the horizontal midplane (which is projected on the bottom panel) shows 2d behavior similar to that in Figure 9.

4 History of modeling internal wave fronts

Modeling observed internal waves propagating over real topography requires a fully two-dimensional, multilayer description. Strong, complex, two dimensional wave-wave and wave-topography interactions have long been observed, for example, in internal waves propagating through the Strait of Gibraltar [53]. Even more complex interactions were recently observed from the Space

Shuttle for internal wave trains propagating in the vicinity of Dongsha Island in the South China Sea by Liu et al. [40]; see Figures 1 and 2. These interactions produce remarkable nonlinear phenomena. In particular, they produce wave front reconnection, as well as the diffraction and refraction expected of large amplitude internal waves interacting with bathymetry and boundaries such as straits, coasts, shoals, islands and atolls.

Equations for strongly nonlinear dispersive waves on the free surface of a *single* layer of incompressible fluid with topography are usually attributed to Green and Naghdi [18], although the same equations were derived earlier by Su and Gardner [50]. These equations for single layer columnar motion (1LCM) generalize the Boussinesq family of shallow-water equations to allow for strong nonlinearity. For finite wave amplitudes, the 1LCM equations capture strongly nonlinear effects, such as the upstream emission of solitary waves and the downstream surface depression and oscillations due to flow over a obstacle at Froude numbers greater than unity [43, 39]. References [43, 39] show that numerical simulations of the 1LCM equations tend to be faithful representations of the corresponding Euler solutions, provides that wave breaking does not occur. The works of Choi and Camassa [10, 11] extended the 1LCM description to a *two-layer* fluid with fixed horizontal upper and lower boundaries, including the cases of two thin layers and of a thin layer over an infinitely deep layer. The CC equations admit bi-directional solutions and they may be derived from a variational principle by following the averaged Lagrangian methods pioneered in Whitham [51]. (See also Miles and Salmon [45], who derived the 1LCM equations using Hamilton's principle in the material representation.) As a consequence of their variational principle, the CC equations possess conservation laws for mass, momentum, and energy. The same equations were derived earlier and analyzed for well-posedness in Liska, Margolin and Wendroff [38, 39] by substituting directly in the governing equations the columnar motion assumption that the vertical velocity is a linear function of vertical coordinate. Choi and Camassa [11] showed explicitly, by assuming first weak nonlinearity and then unidirectional wave propagation, that these equations recover all the known weakly nonlinear evolution equations for interfacial waves. The well-posedness issue identified by Liska et al. [38, 39] for these equations is similar to the steepening lemma result proved for the CH equation in [6]. Namely, an initial velocity distribution possessing an inflection point of negative slope will develop a vertical slope in finite time. This loss of well-posedness in finite time is part of the mechanism for the formation of the singular solutions we

seek to investigate here. These singular solutions dominate the initial value problems we study and one should expect to deviate from standard concepts of well-posedness in studying their emergence from smooth initial conditions.

In the next few sections of this paper, we shall use the Euler-Poincaré (EP) variational principle for continuum motion in the spatial, or Eulerian, representation [23] to extend the CC equations by deriving multilayer columnar motion (MLCM) equations. MLCM describes strongly nonlinear internal waves propagating on the interfaces of layer-stratified incompressible fluid driven by gravity, moving over topography and possessing a free surface. The MLCM equations are derived here by imposing columnar motion in the EP variational principle for the Euler equations of a multilayer incompressible fluid with a free surface and variable topography. In one dimension, when the free surface and bathymetry are neglected, the MLCM equations recover the CC equations [11].

Strictly speaking, the CC equations are for vertically averaged horizontal velocities, not simply for columnar motion. Thus, they need not have emerged from an action principle for multilayer columnar motion. The vertically averaged horizontal velocities do undergo columnar motion, but this alone is insufficient to expect *a priori* that the CC equations would arise by substituting columnarity into the action principle. However, Choi and Camassa noticed *a posteriori* that their equations do satisfy a variational principle [11]. We have used their observation, combined with the suggestive results of Liska, Margolin and Wendroff [38, 39] and of Miles and Salmon [45] to extend the CC equations to the more general MLCM situation required for modeling the large scale internal wave interactions observed in the Gibraltar Strait and the South China Sea.

The new MLCM equations (20) derived here generalize the CC equations for the interfacial motion between two layers with fixed horizontal upper and lower boundaries, to allow for waves at the top free surface as observed by the Space Shuttle, to include an arbitrary number of fluid layers, and to account for variable bottom topography. These equations provide fundamental insight into how topography and the multiple layers of a stably stratified incompressible fluid are coupled by nonlinear, nonhydrostatic, dynamical effects. This dynamical coupling arises in addition to the more familiar multilayer hydrostatic effects. We derive these nonhydrostatic equations and their natural boundary conditions from the Euler-Poincaré variational principle for continuum motion of Holm, Marsden and Ratiu [23] by including in the fluid Lagrangian the kinetic energy due to vertical oscillations in the

columnar motion approximation. Their traveling waves, stability properties, well-posedness, weakly nonlinear aspects, relations to other approximations and numerical simulations will be addressed elsewhere.

After deriving the highest level nonhydrostatic MLCM equations for multilayer internal waves, we make a series of Boussinesq-like approximations for weakly nonlinear waves that allows comparison with previous work and which eventually results in a minimal description, EPDiff (1). We then discuss some of the geometrical properties and singular solutions of EPDiff. Finally, we describe our numerical approach and present a large suite of 2d and 3d simulation results for EPDiff.

5 Nonhydrostatic multilayer columnar motion (MLCM) equations

Consider a multilayer fluid consisting of N immiscible layers moving under the constant vertical acceleration of gravity. Regard the top layer (whose rest position is $z = 0$) as first and the bottom layer as last (N th), so that i increases with the depth of the layer. The i -th layer has constant density ρ_i , horizontal velocity $\mathbf{u}_i(x, y, z, t)$, vertical velocity $w_i(x, y, z, t)$, upper surface at $z = h_i(x, y, t)$ and lower surface at $z = h_{i+1}(x, y, t)$, so the layer thicknesses are $D_i = h_i - h_{i+1}$, with $i = 1, \dots, N$. The N th layer (on the bottom) has density ρ_N , horizontal velocity \mathbf{u}_N , upper surface at $z = h_N(x, y, t)$ and lower surface at $z = h_{N+1} = -b(x, y)$, the fixed bottom topography. We shall assume the multilayer fluid is stably stratified, so that $\rho_i < \rho_{i+1}$, for $i = 1, \dots, N$ (density increases downward).

5.1 Implications of the columnar motion ansatz

The Lagrangian in Hamilton's principle for a multilayer fluid is the difference of its kinetic and potential energies,

$$\ell = \int dx dy \sum_{i=1}^N \rho_i \int_{h_{i+1}}^{h_i} \left[\frac{1}{2} |\mathbf{u}_i|^2 + \frac{1}{2} w_i^2 - gz \right] dz. \quad (7)$$

One may also include the effects of Coriolis force due to rotation by adding the term $\sum_{i=1}^N D_i \mathbf{R}(x, y) \cdot \mathbf{u}_i + D_i S(x, y) w_i$ to the Lagrangian density, where $2\Omega = \text{curl}(\mathbf{R}(x, y) + S(x, y) \hat{\mathbf{z}})$ is twice the rotation vector.

We note that incompressibility $\nabla \cdot \mathbf{u}_i = -\partial_z w_i$ relates the horizontal and vertical velocities in each layer. When one also assumes the **columnar motion ansatz**, namely,

$$\frac{\partial \mathbf{u}_i}{\partial z} = 0, \quad (8)$$

then incompressibility also implies linear dependence of the vertical velocity on the vertical coordinate in each layer, as

$$w_i = -z \nabla \cdot \mathbf{u}_i + \partial_t h_{i+1} + \nabla \cdot (h_{i+1} \mathbf{u}_i), \quad (9)$$

for $h_{i+1} \leq z \leq h_i$. The thickness $D_i = h_i - h_{i+1}$ of the i -th layer obeys a continuity equation,

$$\partial_t D_i + \nabla \cdot (D_i \mathbf{u}_i) = 0. \quad (10)$$

Hence, the volume of each constant density layer is conserved and the layer thicknesses remain positive. We also note that $h_{i+1} = -b(x, y) + \sum_{j=i+1}^N D_j$, as the sums of differences D_j cancel in pairs and $h_{N+1} = -b(x, y)$. The total depth is $\sum_{j=1}^N D_j = h_1(x, y, t) + b(x, y)$.

As a result of these relations, the vertical velocity in the i -th layer for $h_{i+1} \leq z \leq h_i$ may be expressed in terms of the horizontal velocities, the layer thicknesses, and the prescribed bathymetry, $b(x, y)$, as [1]

$$w_i = -z \nabla \cdot \mathbf{u}_i - \nabla \cdot b(x, y) \mathbf{u}_i - \sum_{j=i+1}^N \nabla \cdot D_j (\mathbf{u}_j - \mathbf{u}_i). \quad (11)$$

We shall substitute this expression obtained from columnarity into the Lagrangian (7), then perform the vertical integrals and use the **Euler-Poincaré** theory to obtain the motion equation in each layer, as the EP equation [23],

$$\frac{\partial}{\partial t} \frac{\delta \ell}{\delta \mathbf{u}_i} + \mathbf{u}_i \cdot \nabla \frac{\delta \ell}{\delta \mathbf{u}_i} + \nabla \mathbf{u}_i^T \cdot \frac{\delta \ell}{\delta \mathbf{u}_i} + \frac{\delta \ell}{\delta \mathbf{u}_i} \nabla \cdot \mathbf{u}_i - D_i \nabla \frac{\delta \ell}{\delta D_i} = 0. \quad (12)$$

This procedure will produce the **multilayer columnar motion** (MLCM) equations (20), which are completed by the corresponding continuity equation (10) in each layer.

5.2 Variational derivatives of the Lagrangian

Columnarity (8) and its implied formula (11) for w_i allow the vertical integrals in the Lagrangian (7) to be performed as,

$$\begin{aligned} \ell = & \frac{1}{2} \int \sum_{i=1}^N \rho_i \left[D_i |\mathbf{u}_i|^2 - g(h_i^2 - h_{i+1}^2) \right. \\ & \left. + \frac{D_i}{6} (B_i^2 + (D_i A_i + B_i)^2 + (D_i A_i + 2B_i)^2) \right] dx dy. \end{aligned} \quad (13)$$

Perhaps not unexpectedly, the integrated kinetic energy is a layer-thickness-weighted sum of squares of the horizontal velocities and their divergences. The additional notation is defined as $A_i \equiv \nabla \cdot \mathbf{u}_i$, so that

$$D_i A_i = - \left(\partial / \partial t + \mathbf{u}_i \cdot \nabla \right) D_i \equiv - \dot{D}_i = \dot{h}_{i+1} - \dot{h}_i,$$

and

$$\begin{aligned} B_i & \equiv \mathbf{u}_i \cdot \nabla b + \sum_{j=i+1}^N \nabla \cdot (D_j \mathbf{u}_j) \\ & = - \left(\frac{\partial}{\partial t} + \mathbf{u}_i \cdot \nabla \right) h_{i+1} = w_i|_{z=h_{i+1}} \equiv -\dot{h}_{i+1}. \end{aligned} \quad (14)$$

Thus, $D_i A_i$ is the rate of expansion of the i -th layer, and B_i is the vertical velocity at its lower interface. Moreover, the vertical velocity at its upper interface is $D_i A_i + B_i = -\dot{h}_i$. The differences of squares in the potential energy of (13) may also be written in terms of the layer thicknesses upon substituting for h_{i+1} , as

$$\begin{aligned} \frac{1}{2} (h_i^2 - h_{i+1}^2) & = \frac{1}{2} D_i^2 + D_i h_{i+1} \\ & = \frac{1}{2} D_i^2 + D_i \left(-b(x, y) + \sum_{j=i+1}^N D_j \right). \end{aligned} \quad (15)$$

Thus, columnarity (8) allows the Lagrangian (7) to be expressed solely in terms of the horizontal velocities $\{\mathbf{u}\}$, their (weighted) divergences, and the layer thicknesses $\{D\}$. The potential energy of each layer is coupled hydrostatically to all the layers beneath it by the last term in (15). We

leave the top layer free. For a rigid lid [2] one would add the constraint $h_1 = -b(x, y) + \sum_{i=1}^N D_i = 0$, imposed by a Lagrange multiplier p_s (the surface pressure) determined by preservation of $h_1 = 0$.

We rearrange the sums by using the following identity, which holds for arbitrary quantities Q_i and R_i , with $i = 1, 2, \dots, N$,

$$\sum_{i=1}^N \left(Q_i \sum_{j=i+1}^N R_j \right) = \sum_{i=1}^N \left(R_i \sum_{j=1}^{i-1} Q_j \right). \quad (16)$$

Consequently, we find that the variational derivatives of the Lagrangian (7) under columnarity (8) are given by [3]

$$\begin{aligned} \delta \ell = & \int dx dy \sum_{i=1}^N \rho_i \left\{ \left(\frac{1}{2} |\mathbf{u}_i|^2 - gh_i - \frac{g}{\rho_i} \sum_{j=1}^{i-1} \rho_j D_j \right) \delta D_i \right. \\ & + \left[\frac{1}{2} (D_i A_i + B_i)^2 + \sum_{j=1}^{i-1} \nabla \cdot C_j \mathbf{u}_j - \mathbf{u}_i \cdot \nabla \sum_{j=1}^{i-1} C_j \right] \delta D_i \\ & \left. + \left[D_i \mathbf{u}_i - \nabla (D_i^2 F_i) - C_i \nabla h_{i+1} - D_i \nabla \sum_{j=1}^{i-1} C_j \right] \cdot \delta \mathbf{u}_i \right\} \end{aligned} \quad (17)$$

where we have introduced notation for two more linear combinations of the interface velocities,

$$F_i \equiv \frac{1}{3} D_i A_i + \frac{1}{2} B_i = -\frac{1}{6} (2\dot{h}_i + \dot{h}_{i+1}), \quad (18)$$

and $C_i \equiv D_i G_i$, with average interface velocity,

$$G_i \equiv \frac{D_i A_i}{2} + B_i = -\frac{1}{2} (\dot{h}_i + \dot{h}_{i+1}). \quad (19)$$

5.3 Euler-Poincaré motion equation for MLCM

Substituting the variational derivatives from the formula for $\delta \ell$ in (17) into the Euler-Poincaré equation (12) yields the desired *multilayer columnar motion* (MLCM) system of equations, which may be manipulated into the simple

form,

$$\begin{aligned} \frac{d\mathbf{u}_i}{dt} + g\nabla H_i &= \frac{1}{D_i} \nabla \left(D_i^2 \frac{dF_i}{dt} \right) - \frac{dG_i}{dt} \nabla b(x, y) \\ &+ \nabla \sum_{j=1}^{i-1} D_j \left(\frac{\partial G_j}{\partial t} + \mathbf{u}_j \cdot \nabla G_j \right) + \frac{dG_i}{dt} \nabla \sum_{j=i+1}^N D_j. \end{aligned} \quad (20)$$

The top line of equation (20) recovers the 1LCM equation of Su-Gardner [50] or Green-Naghdi [18] in each layer. The new terms involve sums on $j \neq i$, which couple the layers. The nonhydrostatic contributions on the right side are *dynamical*, with $d/dt = (\partial/\partial t + \mathbf{u}_i \cdot \nabla)$. The hydrostatic pressure in the i -th layer is given by $p_i \equiv \rho_i g H_i$, with H_i as in $\delta\ell$ (17),

$$H_i \equiv h_i + \frac{1}{\rho_i} \sum_{j=1}^{i-1} \rho_j D_j \quad \text{and} \quad h_i = -b + \sum_{j=i}^N D_j. \quad (21)$$

The quantities F_i and G_i in (20) are defined in terms of the layer thicknesses and velocities by equations (18,19). The resulting MLCM equations (20) are closed by the layer continuity relations (10) for D_i .

The MLCM motion equations (20) reduce to the standard 1LCM equations [50, 18] in the single layer case, in which there are no sums on $j \neq i$. In one dimension, the MLCM equations generalize equations (3.19-3.22) of Choi and Camassa [11] for the interfacial motion between two layers with fixed horizontal upper and lower boundaries, to allow for waves at the top free surface, to include an arbitrary number of fluid layers and to account for variable bottom topography. One recovers the CC equations of [11, 38, 39] by specializing to two layers with fixed upper and lower boundaries in one dimension. This amounts to setting $N = 2$ and neglecting terms involving B_i , G_i and G_j in equations (17-20).

Nonhydrostatic contributions to momentum and pressure. In the variational formula for $\delta\ell$ (17), we see that the horizontal momentum in the columnar motion equation for the i -th layer involves horizontal gradients,

$$\begin{aligned} \mathbf{m}_i &\equiv \frac{\delta\ell}{\delta\mathbf{u}_i} \equiv \sum_{j=1}^N \mathcal{L}_{ij}(\{D\}, b) \mathbf{u}_j \\ &= \rho_i D_i \left(\mathbf{u}_i - \frac{1}{D_i} \nabla (D_i^2 F_i) - G_i \nabla h_{i+1} - \nabla \sum_{j=1}^{i-1} D_j G_j \right). \end{aligned} \quad (22)$$

The last equality defines the symmetric, positive definite operator in $\mathbf{m}_i = \sum_{j=1}^{i-1} \mathcal{L}_{ij}(\{D\}, b) \mathbf{u}_j$, which depends on the set of layer thicknesses $\{D\}$ and the bottom topography b . In terms of this operator, the multilayer fluid Lagrangian (7) under columnarity (8) becomes

$$\ell = \frac{1}{2} \int \sum_{i=1}^N \left(\mathbf{m}_i \cdot \mathbf{u}_i - g(h_i^2 - h_{i+1}^2) \right) dx dy. \quad (23)$$

Because the multilayer Lagrangian (23) depends on the horizontal spatial coordinate through the bathymetry $b(x, y)$, the spatial integral of the total momentum (22) is not conserved, except in translation-invariant directions of $b(x, y)$. The total pressure in the i -th layer, $\delta\ell/\delta D_i$, also contains non-hydrostatic contributions arising from the vertical columnar oscillations and velocity differences among the layers, in addition to its hydrostatic component. All of these additional nonhydrostatic contributions to the momentum and the pressure gradient arise from the kinetic energy of vertical motion and are proportional to the velocities of the interfaces [4].

Kelvin circulation theorem and potential vorticity. Although the layer motions are strongly coupled, each layer has its own Kelvin circulation theorem,

$$\frac{d}{dt} \oint_{c(\mathbf{u}_i)} \frac{\mathbf{m}_i}{D_i} \cdot d\mathbf{x} = 0, \quad (24)$$

where the closed loop $c(\mathbf{u}_i)$ moves with the horizontal velocity \mathbf{u}_i in the i -th layer. In addition, each layer also locally conserves its own potential vorticity (PV), i.e.,

$$\frac{\partial q_i}{\partial t} + \mathbf{u}_i \cdot \nabla q_i = 0 \quad \text{where} \quad q_i = \frac{1}{D_i} \hat{\mathbf{z}} \cdot \text{curl} \frac{\mathbf{m}_i}{D_i}. \quad (25)$$

Consequently, one has an infinite set of conservation laws,

$$C_\Phi = \int D_i \Phi(q_i) dx dy, \quad \text{for any function } \Phi. \quad (26)$$

The C_Φ are Casimirs of the Lie-Poisson Hamiltonian operator for the MLCM system and they play a role in classifying the MLCM equilibrium solutions, as in [20, 24].

Both the Kelvin circulation theorem and its associated local conservation of potential vorticity follow from the invariance properties of the EP variational principle. Namely, the EP variational principle is invariant under fluid parcel relabeling that preserves Eulerian quantities. For full details of the Kelvin-Noether theorem, see [23]. The implications of PV conservation for multilayer internal waves remain to be investigated. PV conservation is a new element of the MLCM equations, which differs fundamentally from the standard Charney-Drazin non-acceleration theorem approach for purely potential waves [8], in allowing solutions representing waves, bores and circulations to coexist and interact nonlinearly.

Lie-Poisson Hamiltonian structure of MLCM. The Euler-Poincaré variational formulation implies the Lie-Poisson Hamiltonian structure of MLCM, upon Legendre transforming the multilayer Lagrangian ℓ in (23), as shown in [23]. Hence, the conserved Hamiltonian for the MLCM equations is $H_{MLCM} = \int \sum_{i=1}^N \mathbf{m}_i \cdot \mathbf{u}_i dx dy - \ell$. Thus, the MLCM equations of motion are expressible in Lie-Poisson Hamiltonian form using the standard **Lie-Poisson bracket** in terms of the momenta $\{\mathbf{m}\}$ and the layer depths $\{D\}$, as in [23, 20, 24]. As expected, the Casimirs for this Lie-Poisson bracket are the potential vorticity functionals $C_\Phi = \int D_i \Phi(q_i) dx dy$, which satisfy $\{H, C_\Phi\} = 0$ for any Hamiltonian H . The corresponding treatment of the Lie-Poisson Hamiltonian structure for the single layer GN equations is given in [20, 7].

Comparison with alternative 2d averaged shallow water equations.

In addition to possessing conservation properties for energy, circulation and potential vorticity, the EP motion equation (20) takes a simpler form than many other depth-integrated motion equations discussed in the literature, such as in [41, 17, 42]. Whether MLCM will be as successful in simulating internal wave interactions remains to be seen. As in all columnar motion equations, a key feature of MLCM is the elliptic operator in (22) relating velocity and momentum. Our numerical simulations in section 9 show that a weakly nonlinear approximation of the elliptic inversion in the MLCM model does capture the characteristic aspects of the internal wave-front collisions and reconnections which were observed in the South China Sea by Liu et al. [40].

6 Weakly nonlinear limit equations

6.1 EP derivation of Boussinesq-like equations

One may rewrite the total Lagrangian (13) without approximation as

$$\begin{aligned} \ell = \frac{1}{2} \int \sum_{i=1}^N \rho_i & \left[D_i |\mathbf{u}_i|^2 - g(h_i^2 - h_{i+1}^2) \right. \\ & \left. + \frac{D_i}{3} \left((D_i A_i)^2 + 3B_{i-1}B_i \right) \right] dx dy. \end{aligned} \quad (27)$$

The two-dimensional CC equations arise as EP equations from this Lagrangian upon neglecting its final term, $\frac{1}{2} \int \sum_{i=1}^N \rho_i D_i B_{i-1} B_i dx dy$. We introduce an alternative approximation of the last term, by approximating it in the weakly nonlinear limit, as

$$\begin{aligned} \ell = \frac{1}{2} \int \sum_{i=1}^N \rho_i & \left[D_i |\mathbf{u}_i|^2 - g(h_i^2 - h_{i+1}^2) \right. \\ & \left. + \frac{d_i}{3} \left((\operatorname{div} D_i \mathbf{u}_i)^2 + 3B_{i-1}B_i \right) \right] dx dy, \end{aligned} \quad (28)$$

where $\{d_i : i = 1, 2, \dots, N\}$ are a set of N constants, differing only slightly from the corresponding D_i . In this alternative approximation, the Lagrangian (28) has the following variational derivatives

$$\mathbf{m}_i \equiv \frac{\delta \ell}{\delta \mathbf{u}_i} = \rho_i D_i \left(\mathbf{u}_i - \frac{d_i}{3} \nabla (\operatorname{div} D_i \mathbf{u}_i) + \frac{1}{D_i} \frac{\delta \mathcal{B}_i}{\delta \mathbf{u}_i} \right) \quad (29)$$

for the momentum density, where $\mathcal{B}_i = (d_i/2)B_{i-1}B_i$, and

$$\frac{1}{\rho_i} \frac{\delta \ell}{\delta D_i} = \frac{1}{2} |\mathbf{u}_i|^2 - gH_i - \frac{d_i}{3} \nabla (\operatorname{div} D_i \mathbf{u}_i) + \frac{\delta \mathcal{B}_i}{\delta D_i}, \quad (30)$$

for the Bernoulli potential.

From these variational derivatives, the multilayer EP equations (12) produce

$$\begin{aligned} \frac{\partial}{\partial t} \mathbf{u}_i + \mathbf{u}_i \cdot \nabla \mathbf{u}_i + g \nabla H_i + \frac{d_i}{3} \nabla \frac{\partial^2 D_i}{\partial t^2} \\ = \mathbf{u}_i \times \operatorname{curl} \frac{1}{D_i} \frac{\delta \mathcal{B}_i}{\delta \mathbf{u}_i} - \nabla \left(\frac{1}{D_i} \mathbf{u}_i \cdot \frac{\delta \mathcal{B}_i}{\delta \mathbf{u}_i} - \frac{\delta \mathcal{B}_i}{\delta D_i} \right). \end{aligned} \quad (31)$$

We call these the “Boussinesq-like” multilayer equations, because the approximation $D_i A_i = D_i \operatorname{div} \mathbf{u}_i \simeq \operatorname{div} D_i \mathbf{u}_i = -\partial D_i / \partial t$ in the Lagrangian (28) replaces the strongly nonlinear dispersive term in the MLCM equations with Boussinesq-like linear dispersion, as

$$\frac{1}{3D_i} \nabla \left(d_i^2 \frac{d(D_i A_i)}{dt} \right) \rightarrow -\frac{d_i}{3} \frac{\partial}{\partial t} \nabla (\operatorname{div} D_i \mathbf{u}_i) = \frac{d_i}{3} \nabla \frac{\partial^2 D_i}{\partial t^2}. \quad (32)$$

This term is linear, by virtue of the continuity equation for each layer thickness. The completion of this approximation depends on the treatment of the \mathcal{B}_i terms in equation (31), which are neglected in the CC equations. In the approximation that one neglects the \mathcal{B}_i terms, the multilayer Boussinesq-like equations become

$$\frac{\partial}{\partial t} \mathbf{u}_i + \mathbf{u}_i \cdot \nabla \mathbf{u}_i + g \nabla H_i + \frac{d_i}{3} \nabla \frac{\partial^2 D_i}{\partial t^2} = 0. \quad (33)$$

These equations are still coupled by the multilayer hydrostatic pressure gradient, where hydrostatic pressure head H_i is given in equation (21).

The contributions of the $\mathcal{B}_i = (d_i/2) B_{i-1} B_i$, terms to the EP equations (29-31) may be obtained by computing the required variational derivatives, as follows.

$$\begin{aligned} \delta \int \sum_{i=1}^N \rho_i \frac{d_i}{2} B_{i-1} B_i dx dy &= \int \sum_{i=1}^N \rho_i \frac{d_i}{2} (B_{i-1} + B_{i+1}) \delta B_i \\ &= \int \sum_{i=1}^N \rho_i \frac{d_i}{2} (B_{i-1} + B_{i+1}) \nabla b \cdot \delta \mathbf{u}_i \\ &\quad - \sum_{i=1}^N (\mathbf{u}_i \delta D_i + D_i \delta \mathbf{u}_i) \cdot \nabla \sum_{j=1}^{i-1} \rho_j \frac{d_j}{2} (B_{j-1} + B_{j+1}). \end{aligned} \quad (34)$$

In the first line, we have used the definition of B_i in equation (14). In the last line, we have dropped boundary terms when integrating by parts and used the summation identity (16). These formulas determine the contributions of the \mathcal{B}_i terms to the EP equations (29-31). In particular, they couple the horizontal motion of the i -th layer to the vertical interface velocity of its *next* nearest layer below, since $B_{i-1} + B_{i+1} = -\dot{h}_i - \dot{h}_{i+2}$. Thus, ignoring the contributions of the \mathcal{B}_i terms corresponds to ignoring interactions among next nearest layers in the weakly nonlinear limit.

6.2 Other weakly nonlinear EP equations

We invoke the weakly nonlinear limit to make a further approximation in the multilayer Lagrangian (27), by representing its kinetic energy due to vertical motion as

$$\ell = \frac{1}{2} \int \sum_{i=1}^N \rho_i \left[D_i |\mathbf{u}_i|^2 - g(h_i^2 - h_{i+1}^2) + \frac{d_i^2 D_i}{3} (\operatorname{div} \mathbf{u}_i)^2 \right] dx dy. \quad (35)$$

Consequently, its variational derivatives become

$$\mathbf{m}_i \equiv \frac{\delta \ell}{\delta \mathbf{u}_i} = \rho_i D_i \left(\mathbf{u}_i - \frac{d_i^2}{3 D_i} \nabla (D_i \operatorname{div} \mathbf{u}_i) \right), \quad (36)$$

for the momentum density, and

$$\frac{1}{\rho_i} \frac{\delta \ell}{\delta D_i} = \frac{1}{2} |\mathbf{u}_i|^2 - g H_i + \frac{d_i^2}{6} (\operatorname{div} \mathbf{u}_i)^2, \quad (37)$$

for the Bernoulli potential. The corresponding EP equations are,

$$\begin{aligned} & \frac{\partial}{\partial t} \mathbf{u}_i + \mathbf{u}_i \cdot \nabla \mathbf{u}_i + g \nabla H_i \\ & - \frac{\partial}{\partial t} \frac{d_i^2}{3 D_i} \nabla (D_i \operatorname{div} \mathbf{u}_i) + \mathbf{u}_i \times \operatorname{curl} \frac{d_i^2}{3 D_i} \nabla (D_i \operatorname{div} \mathbf{u}_i) \\ & = - \frac{d_i^2}{3} \nabla \left(\frac{1}{2} (\operatorname{div} \mathbf{u}_i)^2 + \frac{1}{D_i} \mathbf{u}_i \cdot \nabla (D_i \operatorname{div} \mathbf{u}_i) \right). \end{aligned} \quad (38)$$

In the *weakly nonlinear limit*, one neglects terms in ∇D_i to find

$$\begin{aligned} & \frac{\partial}{\partial t} \left(\mathbf{u}_i - \frac{d_i^2}{3} \nabla (\operatorname{div} \mathbf{u}_i) \right) + \mathbf{u}_i \cdot \nabla \mathbf{u}_i + g \nabla H_i \\ & = - \frac{d_i^2}{3} \nabla \left(\frac{1}{2} (\operatorname{div} \mathbf{u}_i)^2 + \mathbf{u}_i \cdot \nabla (\operatorname{div} \mathbf{u}_i) \right) + O(\nabla D_i). \end{aligned} \quad (39)$$

Upon neglecting terms of order $O(\nabla D_i)$, choosing the center of volume frame of reference with $\sum_{i=1}^N D_i \mathbf{u}_i = 0$ for $N = 2$, and specializing to one dimension, one recovers the weakly nonlinear limit of the CC equations in [11]. These weakly nonlinear limit equations were shown in [11] to recover all of the various Boussinesq approximations for one dimensional shallow water theory.

Remark on inversion of the second order elliptic operator. As with all the equations in the GN family, the evolution equation (39) requires inversion of a second order operator in solving for fluid velocity \mathbf{u}_i from momentum density \mathbf{m}_i at each time step. A simplification occurs in the weakly nonlinear approximation, because the operator $(1 - \frac{d_i^2}{3} \nabla \text{div})$ appearing in this approximation is independent of the layer thicknesses, D_i , which do enter at the fully nonlinear level as in equations (22), (29) and (36). The nonlocality and smoothing associated with inversion of such elliptic operators is a characteristic feature of the *entire family* of GN equations.

The remainder of this paper is devoted to using the EP theory in characterizing the two-dimensional effects of this elliptic operator inversion on the solutions of equations in the GN family of shallow water equations. To focus our attention on this aspect of the investigation, we shall not require the effects of potential energy.

7 Kinetic energy Lagrangians and the EPDiff geodesic equation

7.1 Kinetic energy Lagrangians

Neglecting potential energy entirely in the weakly nonlinear limit multilayer Lagrangian (35), by setting $D_i \rightarrow d_i$, gives

$$\ell = \frac{1}{2} \int \sum_{i=1}^N \rho_i d_i \left[|\mathbf{u}_i|^2 + \frac{d_i^2}{3} (\text{div } \mathbf{u}_i)^2 \right] dx dy. \quad (40)$$

The corresponding momentum density involves the second order elliptic operator,

$$\mathbf{m}_i \equiv \frac{\delta \ell}{\delta \mathbf{u}_i} = \rho_i d_i \left(\mathbf{u}_i - \frac{d_i^2}{3} \nabla (\text{div } \mathbf{u}_i) \right). \quad (41)$$

Without potential energy, the layers decouple and the EP equation (12) takes the same form in every layer, so we may drop the layer index i and write the EP equation for the kinetic energy Lagrangian (40) as

$$\frac{\partial}{\partial t} \mathbf{m} + \nabla \mathbf{u}^T \cdot \mathbf{m} + \mathbf{m} (\text{div } \mathbf{u}) = 0, \quad \text{with} \quad \mathbf{m} = \mathbf{u} - \frac{d^2}{3} \nabla (\text{div } \mathbf{u}). \quad (42)$$

By design, this equation has no contribution from potential energy. In addition, its evolution conserves the kinetic energy,

$$\ell = \frac{1}{2} \int \left[|\mathbf{u}|^2 + \frac{d^2}{3} (\operatorname{div} \mathbf{u})^2 \right] dx dy. \quad (43)$$

Evolution by kinetic energy in Hamilton's principle results in geodesic motion, with respect to the velocity norm provided by the kinetic energy Lagrangian.

Reduction to the Camassa-Holm (CH) equation in 1d. In one dimension, equation (42) simplifies to

$$\frac{\partial m}{\partial t} + \frac{\partial}{\partial x}(mu) + m \frac{\partial u}{\partial x} = 0, \quad \text{with} \quad m = u - \alpha^2 \frac{\partial^2 u}{\partial x^2}. \quad (44)$$

This is the dispersionless limit of the Camassa-Holm (CH) equation [6], which is known to be the equation at quadratic order in the shallow water asymptotic expansion, one full order beyond KdV, whereas KdV appears at linear order in this expansion [13, 14, 15]. (The dispersionless limit of the CH equation appears because we are ignoring potential energy in this part of our investigation.)

Strengthening the kinetic energy norm to H_α^1 . The kinetic energy (43) is only part of the H_α^1 norm of the velocity, defined as

$$\begin{aligned} \|\mathbf{u}\|_{H_\alpha^1}^2 &= \int \left[|\mathbf{u}|^2 + \alpha^2 (\operatorname{div} \mathbf{u})^2 + \alpha^2 (\operatorname{curl} \mathbf{u})^2 \right] dx dy \\ &= \int \left[|\mathbf{u}|^2 + \alpha^2 |\nabla \mathbf{u}|^2 \right] dx dy. \end{aligned} \quad (45)$$

Here we assume \mathbf{u} is tangential on the boundaries upon integrating by parts in Cartesian geometry. We have also simplified the notation slightly by replacing $d^2/3$ with α^2 , where α is a length scale. In anticipation that mathematical analysis will be facilitated by controlling the entire H_α^1 norm of the velocity, we shall choose our kinetic energy Lagrangian to be

$$\ell = \frac{1}{2} \|\mathbf{u}\|_{H_\alpha^1}^2 = \frac{1}{2} \int \left[|\mathbf{u}|^2 + \alpha^2 |\nabla \mathbf{u}|^2 \right] dx dy. \quad (46)$$

The corresponding EP equation (12) is EPDiff, which involves the familiar *Helmholtz* operator in the relation between fluid velocity and momentum density,

$$\frac{\partial}{\partial t} \mathbf{m} + \mathbf{u} \cdot \nabla \mathbf{m} + \nabla \mathbf{u}^T \cdot \mathbf{m} + \mathbf{m}(\operatorname{div} \mathbf{u}) = 0, \quad \text{with} \quad \mathbf{m} \equiv \frac{\delta \ell}{\delta \mathbf{u}} = \mathbf{u} - \alpha^2 \Delta \mathbf{u}. \quad (47)$$

We shall assume *periodic boundary conditions* for the remainder of our investigations in this paper. An alternative way of writing EPDiff (47) is

$$\frac{\partial}{\partial t} \mathbf{m} - \mathbf{u} \times \operatorname{curl} \mathbf{m} + \operatorname{grad}(\mathbf{u} \cdot \mathbf{m}) + \mathbf{m}(\operatorname{div} \mathbf{u}) = 0, \quad (48)$$

which involves the three differential operators curl, gradient and divergence in two dimensions. This is the EPDiff equation whose solution behavior for the initial value problem is studied in the remainder of the paper.

7.2 Momentum maps for singular solutions of EPDiff

Substituting the singular momentum solution formula (3) for $s \in \mathbb{R}^1$ and its corresponding velocity (4) into EPDiff, then integrating against a smooth test function, implies the following Lagrangian wave front equations,

$$\begin{aligned} \frac{\partial}{\partial t} \mathbf{Q}_a(s, t) &= \sum_{b=1}^N \int \mathbf{P}_b(s', t) G(\mathbf{Q}_a(s, t), \mathbf{Q}_b(s', t)) ds', \\ \frac{\partial}{\partial t} \mathbf{P}_a(s, t) &= - \sum_{b=1}^N \int (\mathbf{P}_a(s, t) \cdot \mathbf{P}_b(s', t)) \frac{\partial}{\partial \mathbf{Q}_a(s, t)} G(\mathbf{Q}_a(s, t), \mathbf{Q}_b(s', t)) ds'. \end{aligned} \quad (49)$$

in which summation is explicit on $b \in 1, 2, \dots, N$, and there is no sum on a . The dot product $\mathbf{P}_a \cdot \mathbf{P}_b$ denotes the inner, or scalar, product of the two vectors \mathbf{P}_a and \mathbf{P}_b in \mathbb{R}^2 . Thus, the momentum solution formula (3) yields a closed set of integro-partial-differential equations (IPDEs) given by (49) for the vector parameters $\mathbf{Q}_a(s, t)$ and $\mathbf{P}_a(s, t)$ with $i = 1, 2, \dots, N$.

Canonical Hamiltonian dynamics of wave fronts in \mathbb{R}^2 . The singular momentum solution formula (3) is shown to be a *momentum map* in [22]. This fact guarantees the following result,

Theorem. *The Lagrangian wave front equations (49) are canonical Hamiltonian equations,*

$$\frac{\partial}{\partial t} \mathbf{Q}_a(s, t) = \frac{\delta H_N}{\delta \mathbf{P}_a}, \quad \frac{\partial}{\partial t} \mathbf{P}_a(s, t) = - \frac{\delta H_N}{\delta \mathbf{Q}_a}. \quad (50)$$

The corresponding Hamiltonian function H_N is,

$$H_N = \frac{1}{2} \iint \sum_{a, b=1}^N (\mathbf{P}_a(s, t) \cdot \mathbf{P}_b(s', t)) G(\mathbf{Q}_a(s, t), \mathbf{Q}_b(s', t)) ds ds'. \quad (51)$$

Because the solution formula (3) is a momentum map the singular solution dynamics is *collective*. That is, the Hamiltonian H_N arises by substituting the singular momentum solution formula (3) into the H^1 kinetic energy norm (46) and using the delta functions to perform the integrals. Thus, the evolutionary IPDE system (49) represents canonically Hamiltonian motion on the space of curves in \mathbb{R}^2 . Moreover, this Hamiltonian motion is geodesic with respect to the co-metric given on these curves in (51) by the Green's function G . The Hamiltonian $H_N = \frac{1}{2} \|\mathbf{P}\|^2$ in (51) for this motion defines the norm $\|\mathbf{P}\|$ in terms of this co-metric. This momentum map result helps organize the theory and provides new avenues of exploration, as suggested in [22]. The remainder of this paper, however, will deal with numerical simulations which capture the momentum exchange properties of these singular EPDiff solutions.

8 Numerical approach

Our numerical studies of EPDiff were performed on uniform, logically rectangular Eulerian grids in 2d and 3d, using the compatible differencing algorithm (CDA) described in [31] and sketched in Figure 16. In contrast to our experience with Lagrangian methods, our numerics using this CDA have captured the elastic bounce expected in head-on collisions with only small distortions observed in the recreated contact curves. Future investigations may allow us to improve CDAs by developing related *variational* integrators based on additional ideas from discrete exterior calculus (DEC) [19, 35].

In this CDA, scalar and vector quantities are defined at locations that are naturally appropriate for the domains and ranges of the discrete divergence, gradient, and curl operators. Eight *spaces*, or grid centerings, include a node

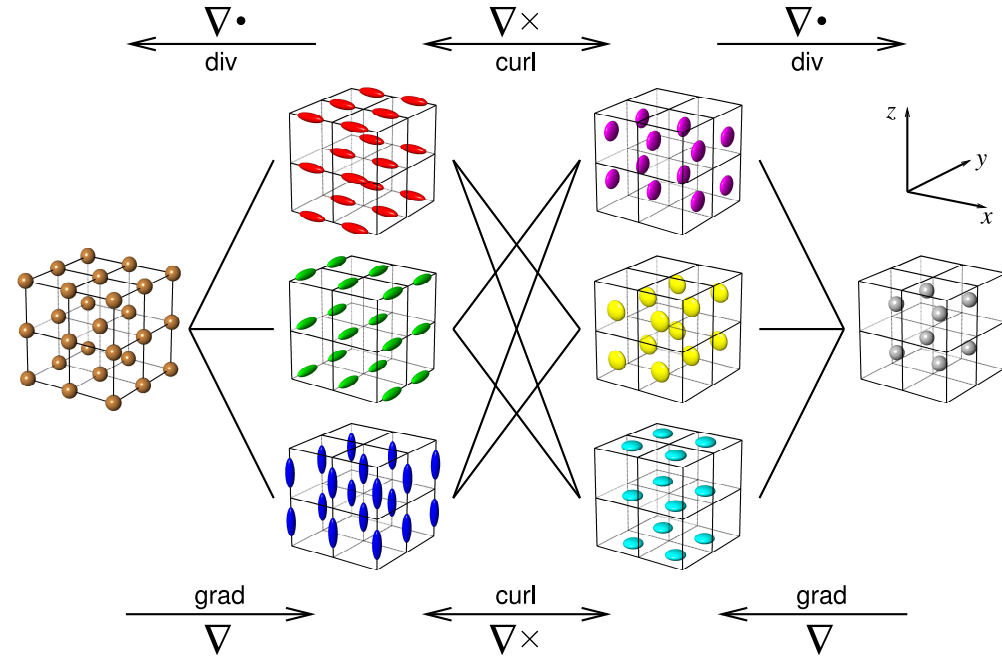


Figure 16: This schematic illustrates a particular compatible differencing algorithm for quantities defined on uniform, logically rectangular grids. Reading left to right, we have nodes, edges, faces, and cells. Nodes and cells support scalar-valued functions, while edges and faces support vector-valued functions. Divergence, gradient, and curl operators map between nodes, edges, faces, and cells.

space, at left, which supports scalar functions. An edge space, consisting of x -direction edges, y -direction edges, and z -direction edges, supports vector functions; x components of vectors exists on x -direction edges, etc. A face space, consisting of faces perpendicular to the x , y , and z directions, also supports vectors. Finally, a cell space supports scalars.

The set of spaces shown in the figure supports two versions each of divergence, gradient, and curl, as described in [31]. Divergence maps vectors to scalars, gradient maps scalars to vectors, and curl maps vectors to vectors. Lines between particular spaces in Figure 16 illustrate how the quantities defined on different spaces contribute to one another through the various operators.

Node-space scalars map to edge-space vectors through the x , y , and z components of the discrete gradient operator, while cell-space scalars map to face-space vectors through the x , y , and z components of another discrete gradient. The x , y , and z components of edge-space vectors each contribute a term ($\partial u/\partial x$, $\partial u/\partial y$, or $\partial u/\partial z$) to a discrete divergence defined on the nodes, while the x , y , and z components of face-space vectors each contribute a term to the cell-based divergence. Finally, the discrete curl operators map between edges and faces in the manner one expects: y and z inputs contribute to x outputs, x and z inputs to y outputs, and x and y inputs to z outputs.

Different components of the same vectors have different numbers of discrete points in this CDA. If the number of nodes is $N \times M \times P$, then the number of x -direction edges is $N - 1 \times M \times P$, the number of y -direction edges is $N \times M - 1 \times P$, and the number of z -direction edges is $N \times M \times P - 1$. The different numbers of discrete points and their slightly different locations must be managed appropriately in any code that uses this scheme.

At present, our numerics are limited to uniform, logically rectangular Eulerian grids with periodic boundary conditions. Our results are promising, but future work will be needed to continue investigating numerical methods and identifying the best candidates for capturing contact behavior on non-uniform or unstructured grids and on non-rectangular domains with boundary conditions other than periodic. For example, when studying the relation of EPDiff to internal waves, one might examine the behavior of contact segments as they interact with islands or atolls placed into the domain.

For our 2d and 3d numerical simulations, we advanced the momentum \mathbf{m} in (48) with an explicit, variable time step Runge-Kutta type predictor-corrector. We selected the time step for numerical stability by trial and error, while our code selected the time step for numerical accuracy (not to exceed

the time step for numerical stability) according to the following well-known formula,

$$h_i = \gamma h_{i-1} \left(\frac{\epsilon |h_{i-1}|}{\|\bar{u}_i - \hat{u}_i\|} \right)^{1/p}, \quad (52)$$

which is used in the following way. At step i of the calculation, we know the predicted solution \bar{u}_i , the corrected solution \hat{u}_i , and the previous time step h_{i-1} . The predictor's order of accuracy is p , while the corrector's order of accuracy is $p + 1$. For our 2d simulations we used $p = 4$, while we used $p = 3$ for our 3d simulations because this reduced the number of large, 3d temporary arrays needed for the calculations, and thereby allowed us to have a higher resolution while still using a reasonably accurate time integration scheme.

A new time step h_i is chosen from (52) based on the old time step h_{i-1} and the norm of the difference between the current predicted and corrected solutions. For both 2d and 3d, we used a relative error tolerance per time step of $\epsilon = 10^{-6}$, a safety factor $\gamma = 0.9$, and the L_2 norm, $\|\cdot\|_2$.

Divergence, gradient, and curl were computed at second order accuracy according to the CDA outlined above, with the vectors \mathbf{m} and \mathbf{u} defined on the edges (shown as the red, green, and blue spaces in Figure 16). We observed that the quality of our numerics did not improve markedly with fourth or sixth order operators, and as expected, the higher-order operators were somewhat slower to compute. Note that our second order operators, in addition to mimicking important properties of their continuum analogs, also have greater accuracy than one might expect at second order. This is because the staggered nature of the grid allows for a smaller “ Δx ” in the difference computations. For example, $\partial u / \partial x$ mapping nodes to x -direction edges uses the stencil $\partial u / \partial x(i + \frac{1}{2}, j, k) = (u(i + 1, j, k) - u(i, j, k)) / \Delta x$, whereas the analogous computation on a strictly nodal grid is $\partial u / \partial x(i, j, k) = (u(i + 1, j, k) - u(i - 1, j, k)) / (2\Delta x)$.

In two dimensions, one must regard the individual spaces in the schematic of Figure 16 as compressed vertically, so that they are flat. This corresponds to having no z component. In this case, x -direction edges (red) are identical to y -direction faces (yellow), y -direction edges (green) are identical to x -direction faces (purple), z -direction edges (dark blue) are identical to nodes (brown), and z -direction faces (light blue) are identical to cells (gray). (This is *not* generally true on nonuniform grids.) Even so, the proper treatment of quantities defined on the different spaces requires that we regard the different

spaces as distinct in 2d.

In our formulation, the curl operator appearing in (48) is still meaningful in 2d. In particular, $\text{curl}(\mathbf{m})$ takes the 2d function \mathbf{m} , defined on the x -direction edges (red) and y -direction edges (green), and maps it to a face-space quantity with x and y components of 0 (which are not stored in a computer code, of course), and a nonzero z component (light blue in Figure 16), which is regarded as a vector that is normal to the plane.

For our 2d simulations, we used a resolution of 1024^2 zones, or 1025^2 nodes. For our 3d simulations, we used 256^3 zones (257^3 nodes). To invert the Helmholtz operator in transforming between \mathbf{m} and \mathbf{u} , we convolved $m(x, t)$ with the Green function in Fourier space. No artificial viscosity or other numerical tricks proved to be necessary for our simulations.

9 Numerical results for EPDiff in 2d

Upcoming sections describe 2d simulations of evolution under EPDiff for each of nine initial velocity distributions. For each simulation we have figures for $\alpha = \sigma$, $\alpha = \sigma/2$, $\alpha = \sigma/4$, and $\alpha = \sigma/8$. Each figure contains six frames, showing the initial magnitude (speed) of velocity, $|\mathbf{u}|$, in the upper left frame, followed by plots of $|\mathbf{u}|$ at future times, reading across and then down. For each simulation, the domain is $[-1, 1] \times [-1, 1]$, x is toward the right, and y is toward the top.

Colors in each frame indicate the magnitude of the velocity, beginning with gray for $|\mathbf{u}| = 0$ and ending with white for the maximum value of $|\mathbf{u}|$, as shown in the color bar in Figure 17. Maximum values of $|\mathbf{u}|$ are determined for each frame individually, not over all frames in a figure, so that the colors in frames with smaller maximum values of $|\mathbf{u}|$ are not washed out. Notice how the use of the color black for small $|\mathbf{u}|$, just above gray for $|\mathbf{u}| = 0$ in the color scheme, allows us to etch the outlines of the spatially confined velocity distributions.

The transverse profile of the velocity distribution along the horizontal midline of each frame is shown as the black (solid) graph in the lower panel of each frame, while the red (dotted) graph shows the vertical midline. The profiles along the northeast and southeast diagonals are plotted in green (solid) and blue (dotted), as sketched in 18. Unlike the colors in the full 2d plots, which are scaled according to the maximum of $|\mathbf{u}|$ in each frame, the vertical axis of the profiles in the lower panels are set between 0 and the

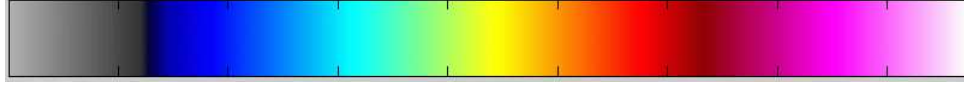


Figure 17: Color scheme for the magnitude of velocity, $|\mathbf{u}|$, in the upcoming figures.

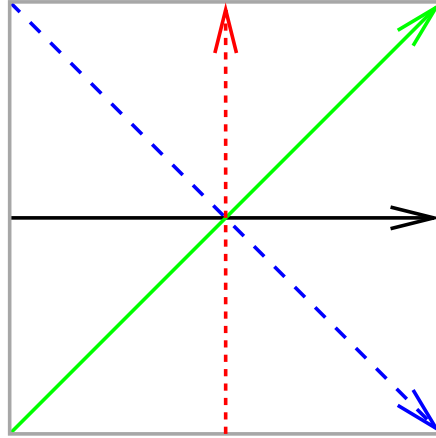


Figure 18: Locations of 1d profiles of $|\mathbf{u}|$ shown in the bottom panels in the upcoming 2d figures.

maximum over all frames (in each figure) of the black, red, green, and blue profiles. So, for example, in the profiles of Figure 19, $|\mathbf{u}|$ as seen in the lower panels is seen to decrease as the evolution proceeds, even though the colors in the 2d plots always vary between gray (minimum) and white (maximum) in order to show maximum detail.

9.1 Plate

Each figure we shall discuss compares evolution under EPDiff with various values of α , starting from the *same* standard initial velocity distribution, which for Figures 19-22 we call “plate.” The velocity in these four 2d plate flows is initially rightward. The initial speed in each of these cases is distributed along a line segment in 2d, which in 3d will be a disc, or plate. Hence, the term plate flow. This initial speed is constant along most of the

segment's length, then falls off as a Gaussian at either end. It falls off exponentially in the transverse directions. The width σ of the initial exponential profile $e^{-|x|/\sigma}$ is the *same* in each figure. We start the EPDiff evolution in each figure with this profile, and we vary the parameter α , in the relation $\mathbf{m} = \mathbf{u} - \alpha^2 \Delta \mathbf{u}$, from problem to problem in fractions of the standard initial profile's exponential width σ .

In Figures 19-19, the values of α are, respectively, σ , $\sigma/2$, $\sigma/4$, and $\sigma/8$. In Figure 19, the initially straight velocity segment evolves to “balloon” outward, while maintaining its transverse peakon profile. In Figures 20-21, the initially straight velocity segment in each case evolves into a series of curved peakon strips of width α with transverse peakon profiles. The lower panels in each case confirm that the velocity profiles in every transverse direction have the characteristic exponential peakon shape, $e^{-|x|/\alpha}$. The first strip to emerge travels fastest and each subsequent strip moves slower. Consequently, the distances between the strips increases. These peakon strips are curved because their endpoints are nearly fixed, while their middle regions are still moving. They stretch during their evolution and increase their lengths. Because of their peakon cross-sections in velocity profile, each peakon strip corresponds to a singular momentum density supported on a curve through the center of the strip. The speed varies along each strip according to its height at the peak at a given point along the curve. Consequently, the “hotspots” appearing in the velocity color scheme as red inhomogeneities along the strip are moving faster than the adjoining yellow regions. The extension of these hotspots along the peakon strips also indicates order $O(1)$ stretching.

One sees kinks near the endpoints of the curved peakon strips that first arise at a distance of order σ , the matching length in the initial velocity profile. Thus, the connection along the segment to the zero speed background influences the stretching of the peakon segments over a finite length scale. These kinks near the endpoints are more pronounced for the larger values of α than for the smaller values, indicating that the length scale α plays a role in the stretching process, as well as in the shape of the transverse profile. These peakon segments also rotate around their nearly fixed endpoints as their expansion and stretching proceeds.

The black (horizontal) transverse profiles in the lower panels of the figures show a steady rightward progression of peakon profiles. The green and blue profiles show a similar progression of peakon profiles along the diagonals. However, the red (vertical) profiles show a symmetric progression, both upward and downward. This means the peakon strips are stretching as they

balloon out from the initial rightward motion. Being roughly circular at late times, this stretching of the strip length is comparable to the distance they propagate horizontally. Therefore, their stretching is an order $O(1)$ effect.

Stability and an open problem. For $\alpha = \sigma$ in Figure 19, the peakon curve segment is stable and it retains its integrity. The other cases, for $\alpha < \sigma$, are unstable and they break into narrower curved peakon segments each of width α , as the evolution tends toward the peakon profile $e^{-|x|/\alpha}$. In fact, any smooth confined initial velocity distribution tends eventually to a set of peakon strips. These are *contact curves*, along which the discontinuity in slope moves with the fluid velocity. Hence, the momentum density tends to a set of moving *curves* on the plane, with each curve embedded in the flow. The latter claim is proved by the isospectral problem in 1d, but for now is only an observation in 2d and 3d. The proof of this observed tendency remains an open problem from the analytical viewpoint.

As $\alpha < \sigma$ decreases in Figures 20-22, the number of emerging contact curves increases. We emphasize that, at sufficiently late times, *only* these contact curves are observed emerging from a confined initial velocity distribution with width greater than α . However, the process occurs does require a certain amount of time to reach completion, as the peakons are successively formed at definite intervals. In the cases 20 and 21 of $\alpha = \sigma/2$ and $\alpha = \sigma/4$ at the times shown, some vestiges of the initial conditions still remain as ramps. As time progresses further, these ramps will eventually decay into a sequence of successively slower moving (lower amplitude) peakon contact curves. No such vestiges remain in the case when $\alpha = \sigma$. This behavior is in accord with the 1d steepening lemma of [6], which states that an initial velocity profile possessing an inflection points of negative slope will develop a vertical slope in finite time. The formation of the vertical slope is part of the nonlinear steepening mechanism which creates the train of peakons from the ramp velocity configuration.

Time reversal. Starting from the final velocity distribution for each value of α , we integrate back to the starting time in the EPDiff evolution numerics. This procedure tests the reversibility of the numerical algorithm. (The EPDiff equation itself is reversible.) Each case reverses accurately to its initial condition, as is evident visually in Figure 23, and as measured in the L^1 , L^2 , and L^∞ norms shown in Table 1. For the simple plate evolutions,

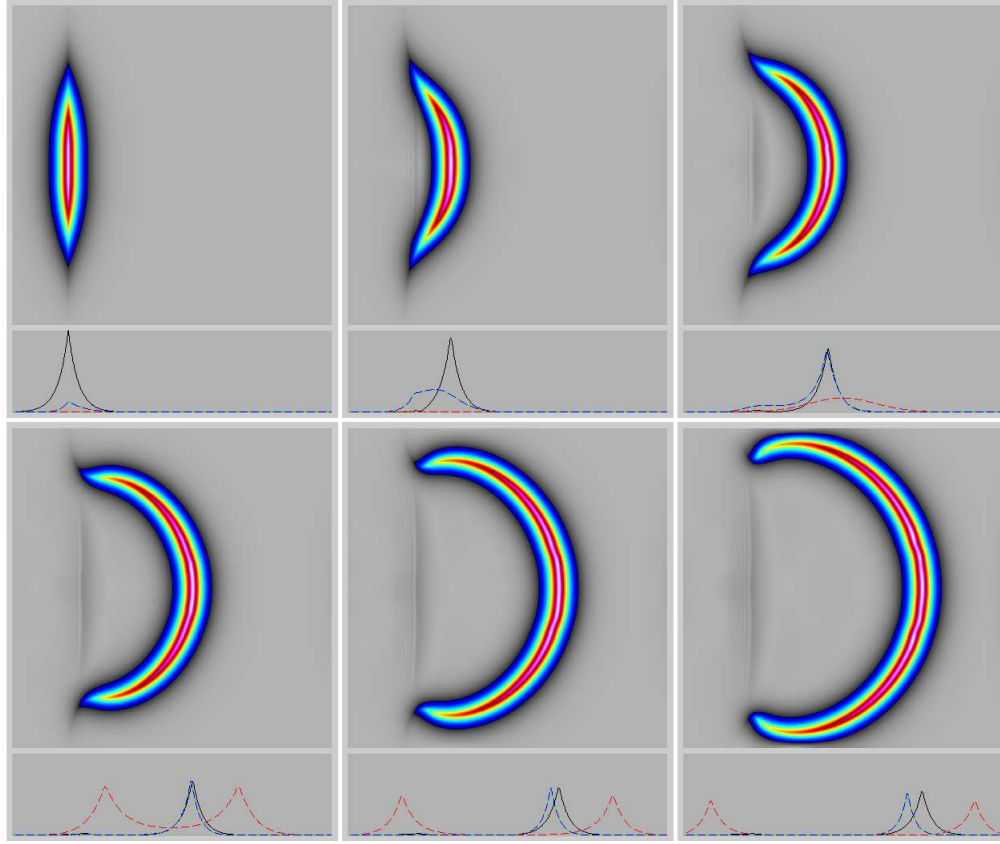


Figure 19: Evolution of the 2d “plate” initial velocity profile with $\alpha = \sigma$.

without any of the head-on collisions of contact curves that will produce the more complicated flows seen below, this reversibility affirms the numerical scheme. It is not a severe test, however, in the sense that reversibility from the endpoint back to the beginning does not guarantee accuracy over the entire forward evolution.

9.2 Parallel

In Figures 24-27, two straight segments are initialized moving rightward. The one behind has twice the speed of the one ahead, and the two segments are offset in the vertical direction. The segments each break into curved

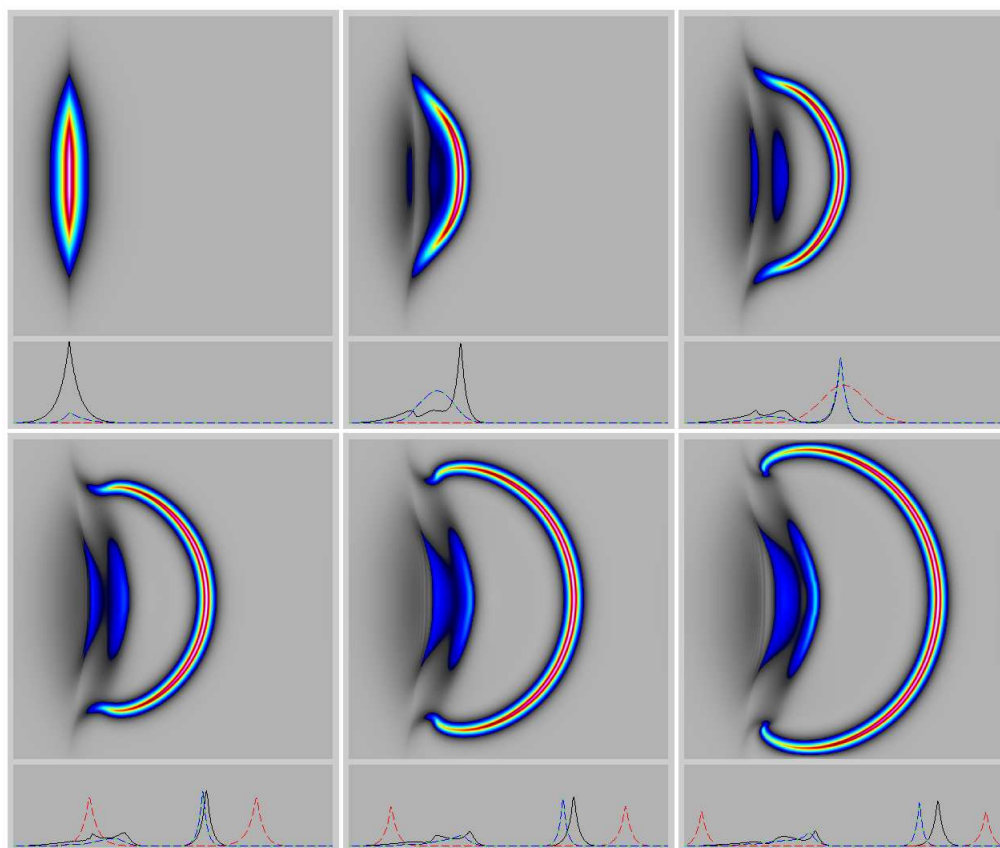


Figure 20: Evolution of the 2d “plate” initial velocity profile with $\alpha = \sigma/2$.

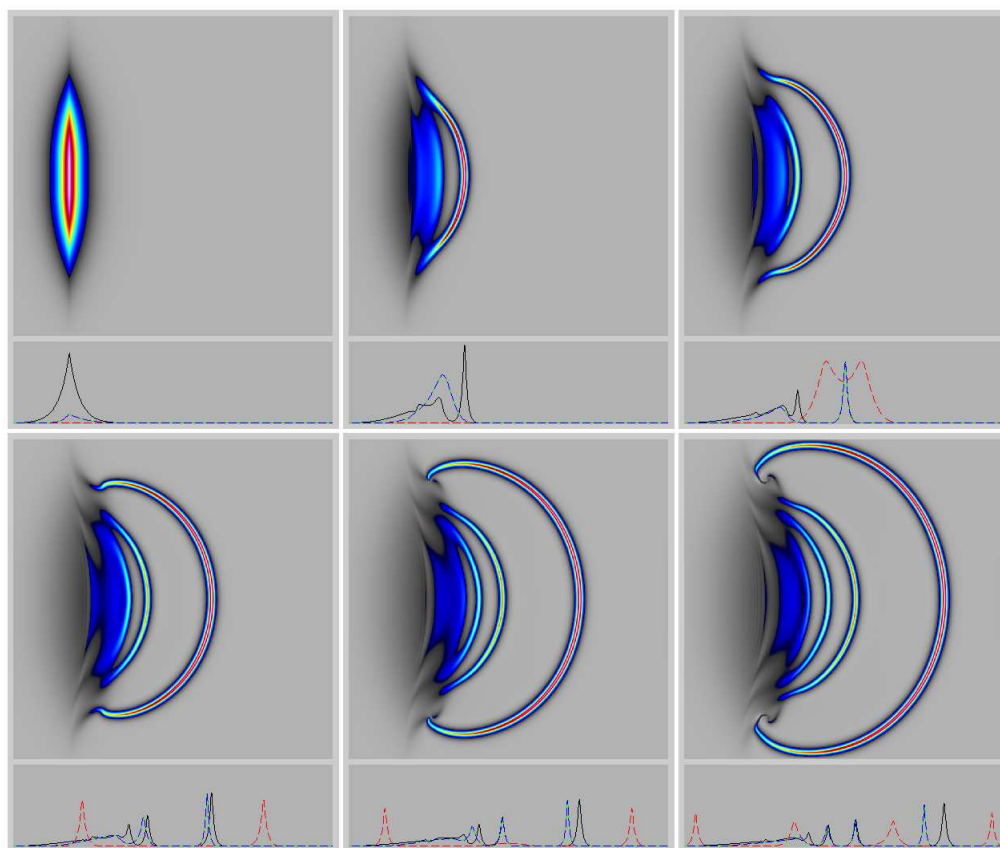


Figure 21: Evolution of the 2d “plate” initial velocity profile with $\alpha = \sigma/4$.

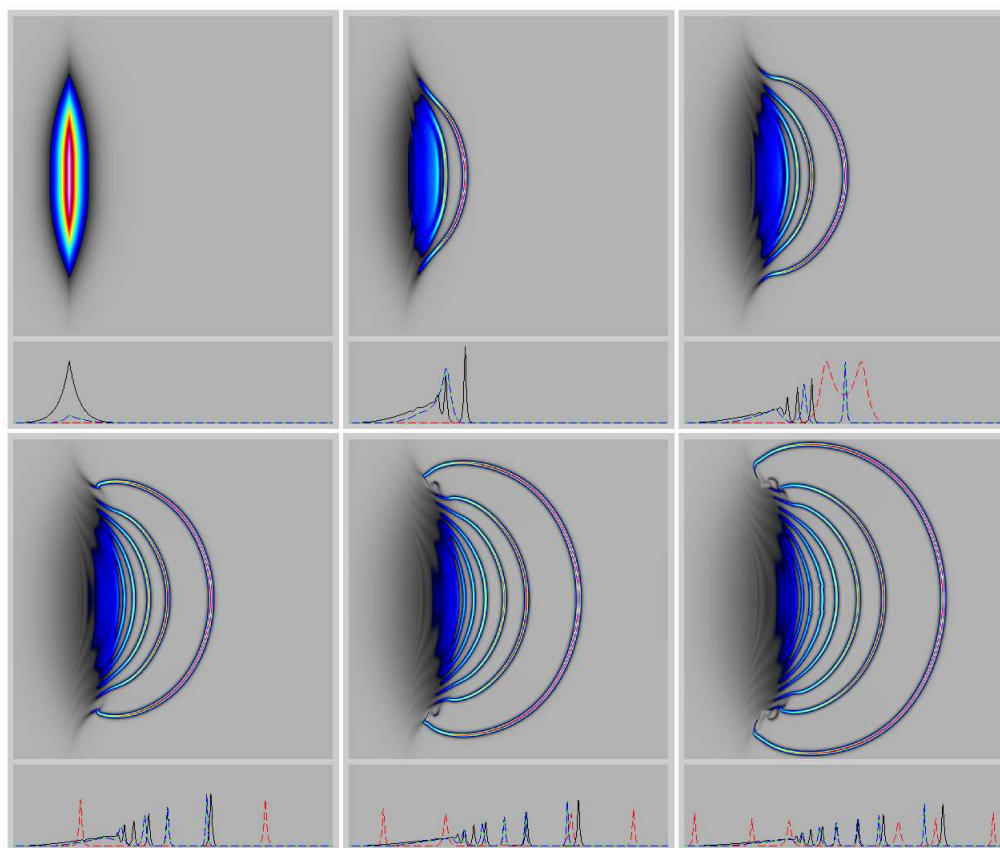


Figure 22: Evolution of the 2d “plate” initial velocity profile with $\alpha = \sigma/8$.

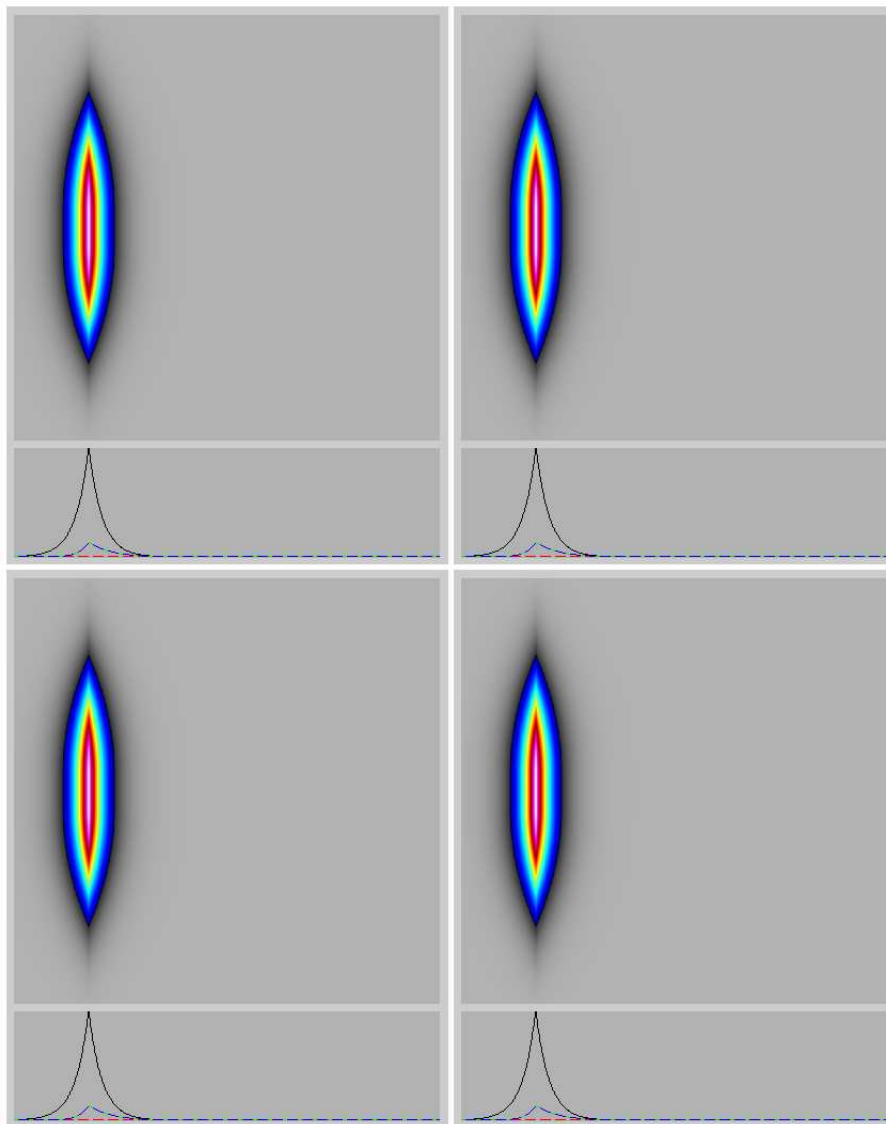


Figure 23: Reconstituted initial velocity profile after time reversal for the 2d “plate” case with $\alpha = \sigma$ (upper left), $\alpha = \sigma/2$ (upper right), $\alpha = \sigma/4$ (lower left), $\alpha = \sigma/8$ (lower right). This initial condition reconstitutes well for all values of α

strips of width α and these undergo overtaking collisions. For $\alpha = \sigma$, the segments retain their integrity as they expand until the overtaking collision occurs. Upon overtaking the slower segment, the faster segment transfers its momentum to the slower one ahead and a remarkable “reconnection” or “melding” of the segments occurs. This reconnection also shows rapid transverse stretching in which “hot spots” of velocity arise and then spread out along the wave front. Also, remarkably, the figures show a low amplitude “peakon wisp” connecting the endpoint of an earlier reconnection to a point (usually to a hotspot) on the leading peakon segment. This wisp apparently provides the “memory” of the previous reconnection, which is required for the evolution to remain reversible. Its reversibility affirms the nondissipative nature of the reconnection process. Moreover, this reconnection must be reversible, because the evolution is Hamiltonian in the continuum limit.

The lower panels of Figures 24-27 for $\alpha = \sigma$ show that the profiles remain exponential both before and after the overtaking collision. For decreasing values of $\alpha < \sigma$, the evolution develops increasing complexity, with numerous overtaking collisions and corresponding reconnections. In each case, one sees the trailing memory wisps arising from these reconnections. These trailing wisps often connect to kinks at hotspots along the curve, indicating that their interaction is nontrivial, even though they have small amplitude. (This may also indicate that the hotspot is the *source* of the trailing wisp.)

In the time-reversed runs shown in Figure 28, all of the overtaking collisions reconstituted their initial conditions accurately in the various norms shown in Table 1. This indicates the accurate reversibility of the numerics for overtaking collisions.

9.3 Skew

Skew flows in Figures 29-32 begin with two peakon segments of the same width, but oriented so that the one behind, which has twice the amplitude (speed) of the one in front, overtakes the one ahead by moving along the negative diagonal. Again, one sees integrity of the $\alpha = \sigma$ case and reconnection with hot spots and memory wisps trailing behind kinks in the main peakon segments after the overtaking peakon segment transfers its momentum to the one ahead. This locally 1d soliton elastic-collision rule seems to explain the momentum transfer. Once again the lower panels show that the solution tends to peakon profiles in each direction.

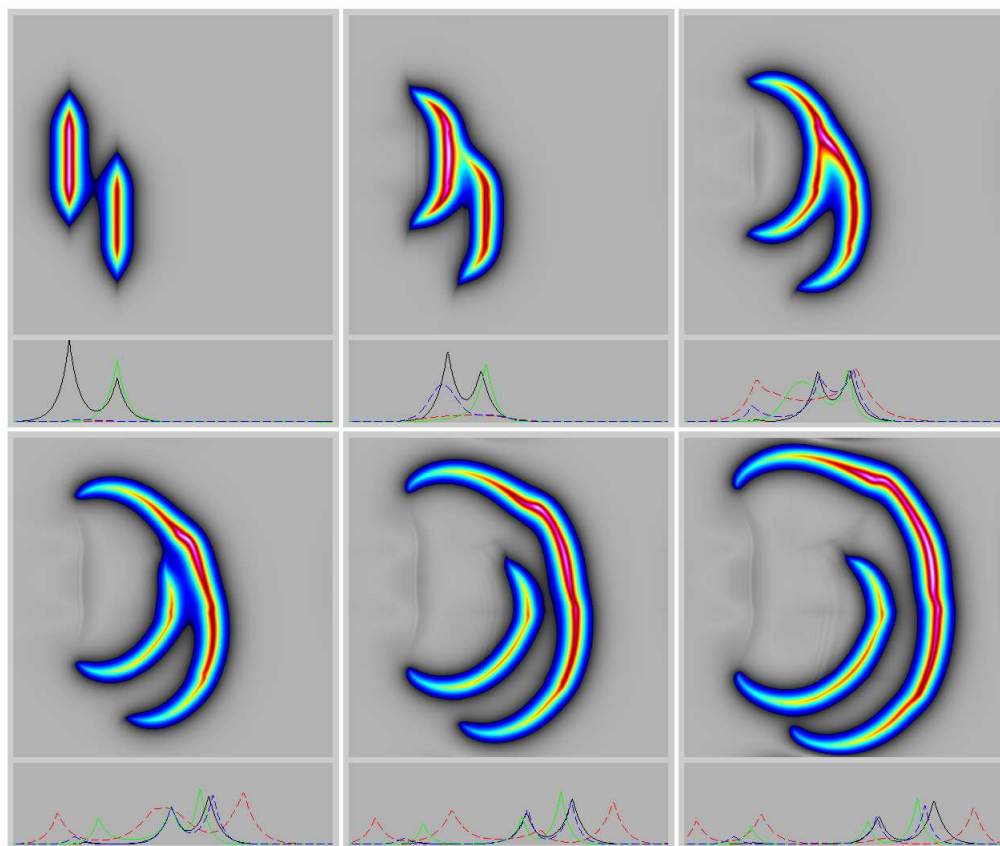


Figure 24: Evolution of the 2d “parallel” initial velocity profile with $\alpha = \sigma$.

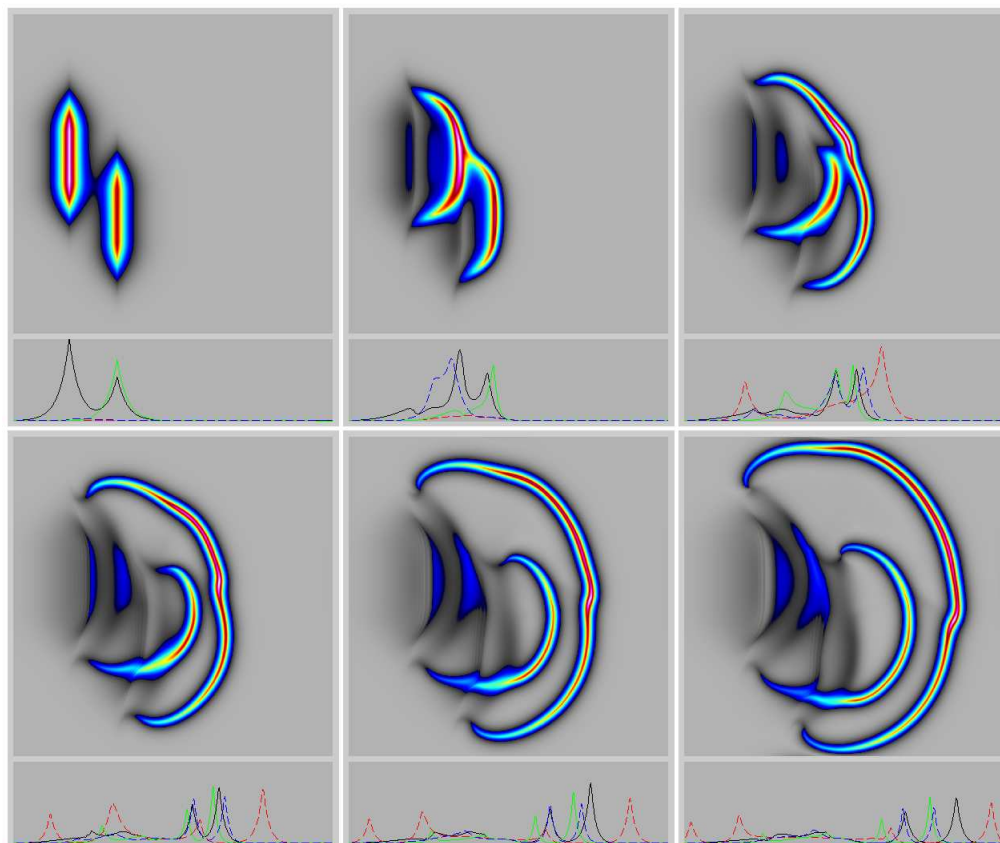


Figure 25: Evolution of the 2d “parallel” initial velocity profile with $\alpha = \sigma/2$.

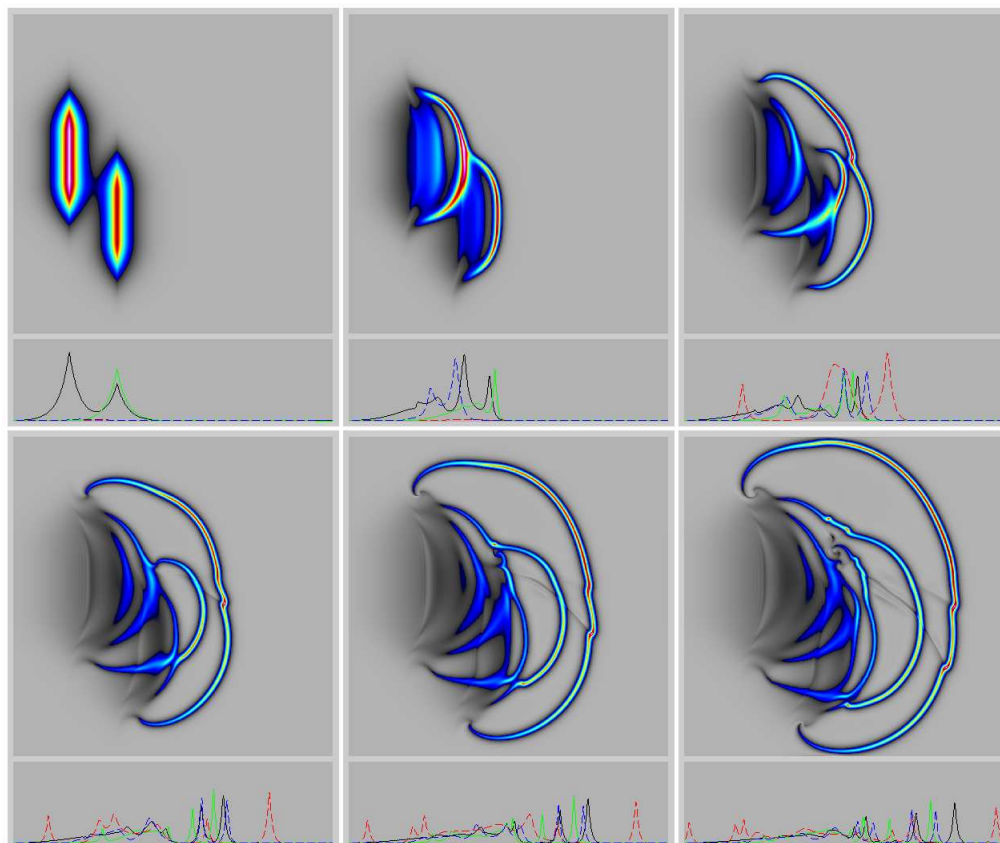


Figure 26: Evolution of the 2d “parallel” initial velocity profile with $\alpha = \sigma/4$.

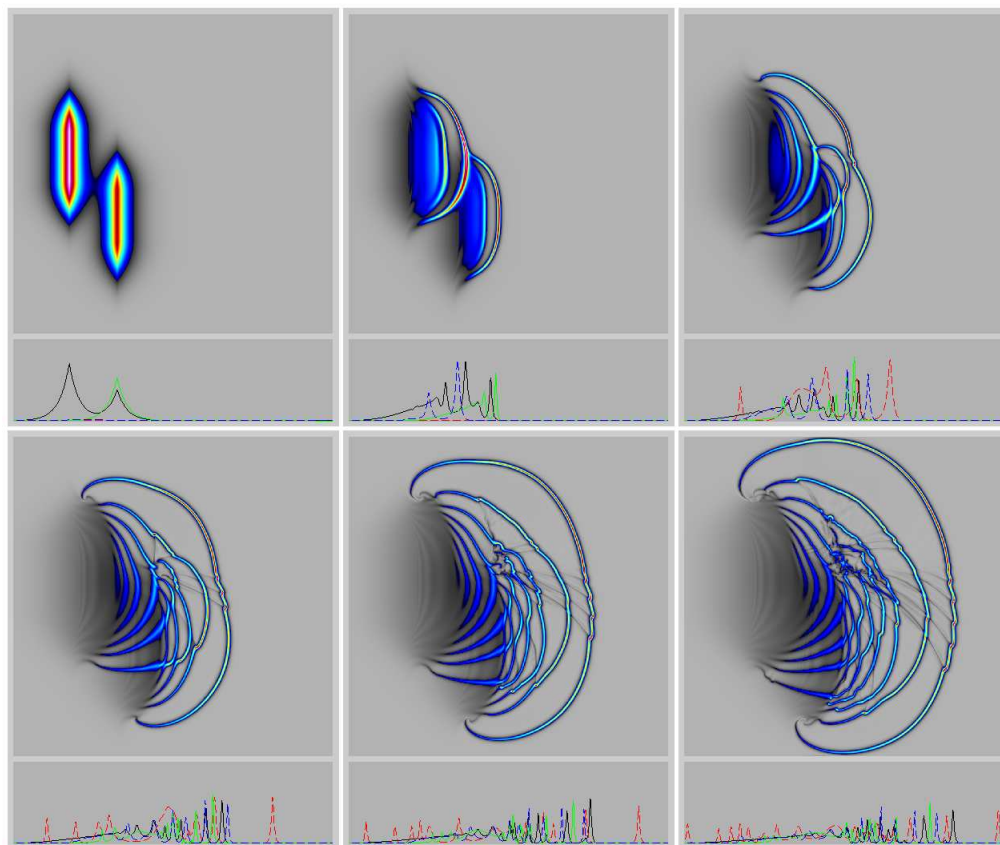


Figure 27: Evolution of the 2d “parallel” initial velocity profile with $\alpha = \sigma/8$.

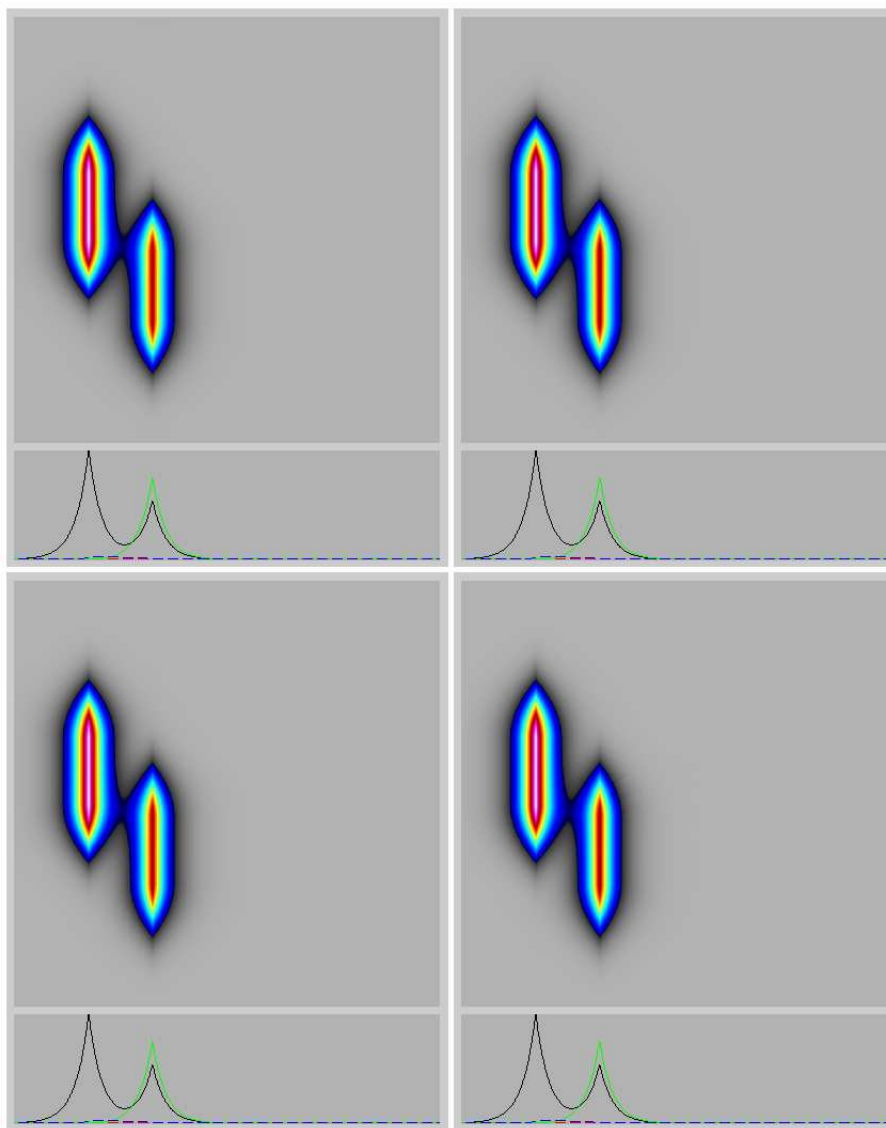


Figure 28: Reconstituted initial velocity profile after time reversal for the 2d “parallel” case with $\alpha = \sigma$ (upper left), $\alpha = \sigma/2$ (upper right), $\alpha = \sigma/4$ (lower left), $\alpha = \sigma/8$ (lower right).

Memory wisps: another open problem. Figures 29-32 raises issues (such as the production of memory wisps) for the 2d peakon segment interactions which could lead to new research well beyond the scope of the present work. As before, in the cases of $\alpha < \sigma$, for skew flows it seems that each memory wisp is attached to a hot spot along a major peakon segment. The memory wisps, by the way, are very low in amplitude, but they seem to also possess the peakon exponential transverse profile. Hence, the stretching motion along the wisp must considerably *faster* than across it. This may be because the hot spots keep contributing to the wisps trailing behind them. Thus, the wisps may be seen as trailing residuals from the hot spots. The memory wisp feature of the reconnection remains to be explained in more detail, both numerically and analytically.

For small $\alpha < \sigma$, the central regions of the skew flows in Figures 30-32 become very intricate (partially mixed). Hence, one could expect that its reversibility is compromised. The case $\alpha = \sigma/8$ is mostly reconstituted after the time reversal, but some small-amplitude, high-frequency errors do remain, as observed in Figure 33. For other values of alpha ($\alpha = \sigma, \sigma/2, \sigma/4$) the initial conditions reconstitute quite well.

9.4 Wedge

The wedge flows in Figures 34-37 are variants of skew flows in Figures 29-32, showing two plates colliding along opposite diagonals in the plane, with reflection symmetry about the horizontal axis. The wedge flows are convergent, and therefore they have some head-on features that emerge on the left-hand side of the collisions. They also show considerable acceleration along the midline, in forming jets moving along the horizontal axis in both directions. This jet formation is due to convergence of momentum which continues to build up after the initial collision. The multiple wedge collisions occurring for values of $\alpha < \sigma$ show successive strong accelerations due to convergence. They also show enhanced stretching of the main peakon segments. These collisions also produce complex patterns of small-amplitude peakon wisps, trailing from hotspots at kinks along the main peakon curves.

Again, the lower panels in Figures 29-32 show primarily peakon profiles and the emergence of peakons from ramp-and-cliff formations with inflection points of negative slope, in agreement with the steepening lemma for CH in 1d.

The head-on features of the wedge collisions cause noticeable errors in

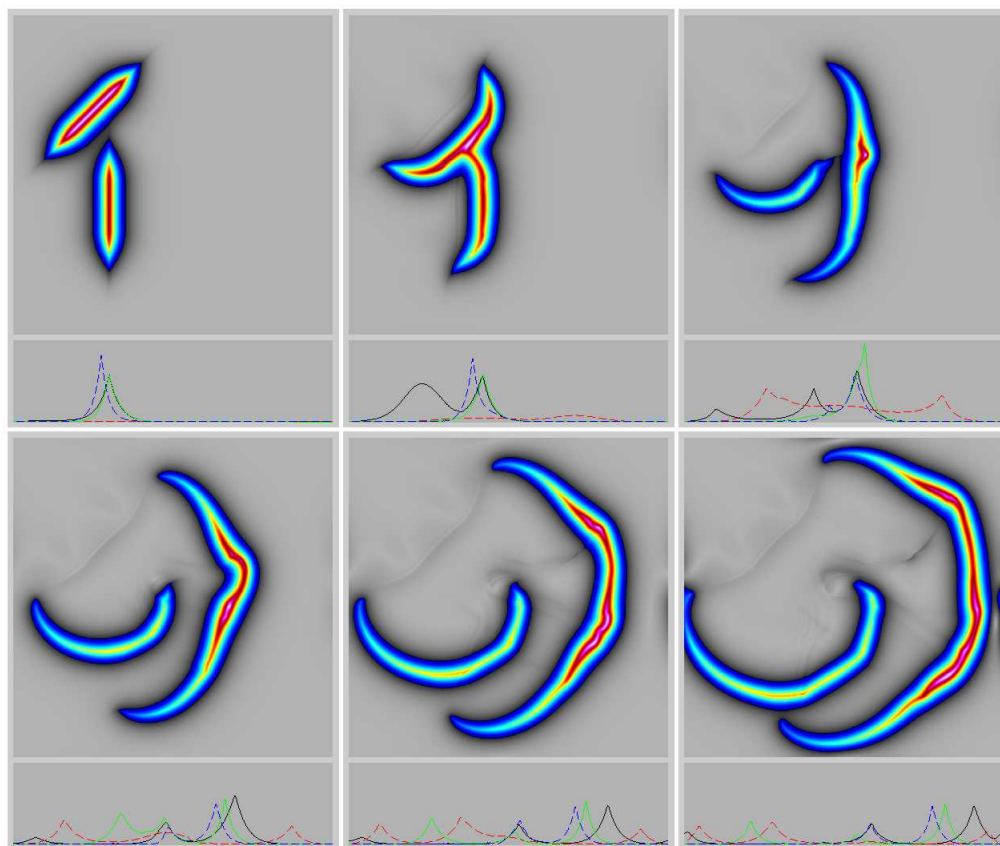


Figure 29: Evolution of the 2d “skew” initial velocity profile with $\alpha = \sigma$.

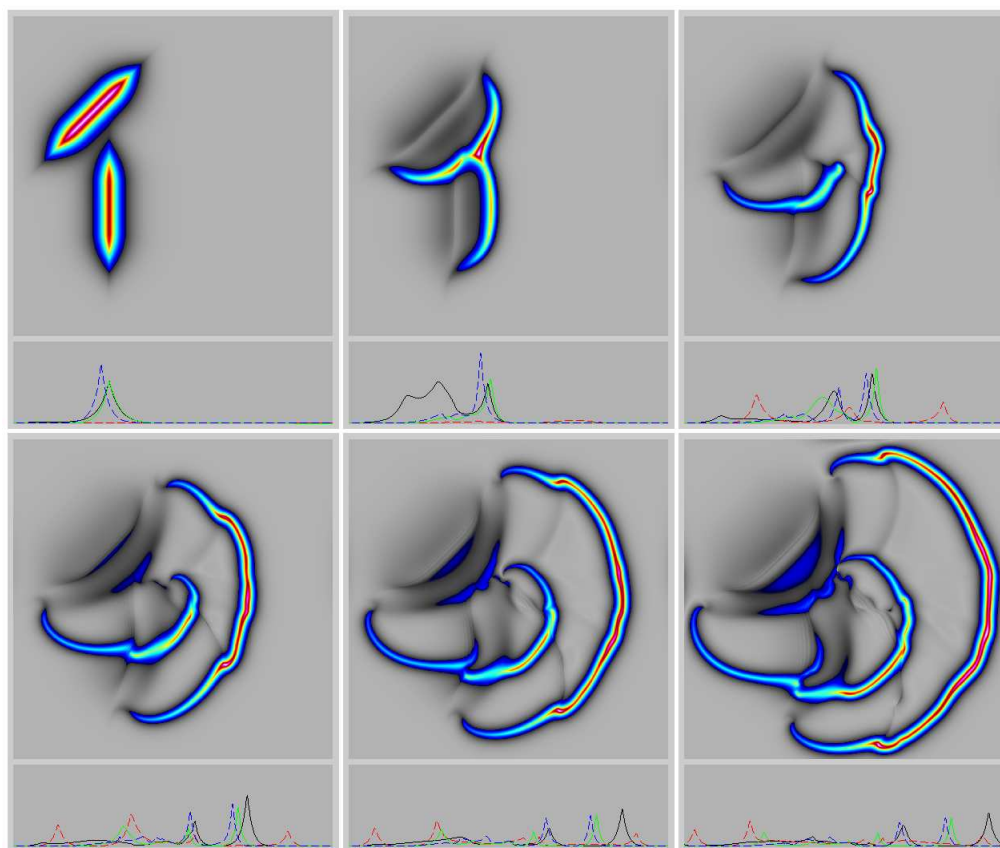


Figure 30: Evolution of the 2d “skew” initial velocity profile with $\alpha = \sigma/2$.

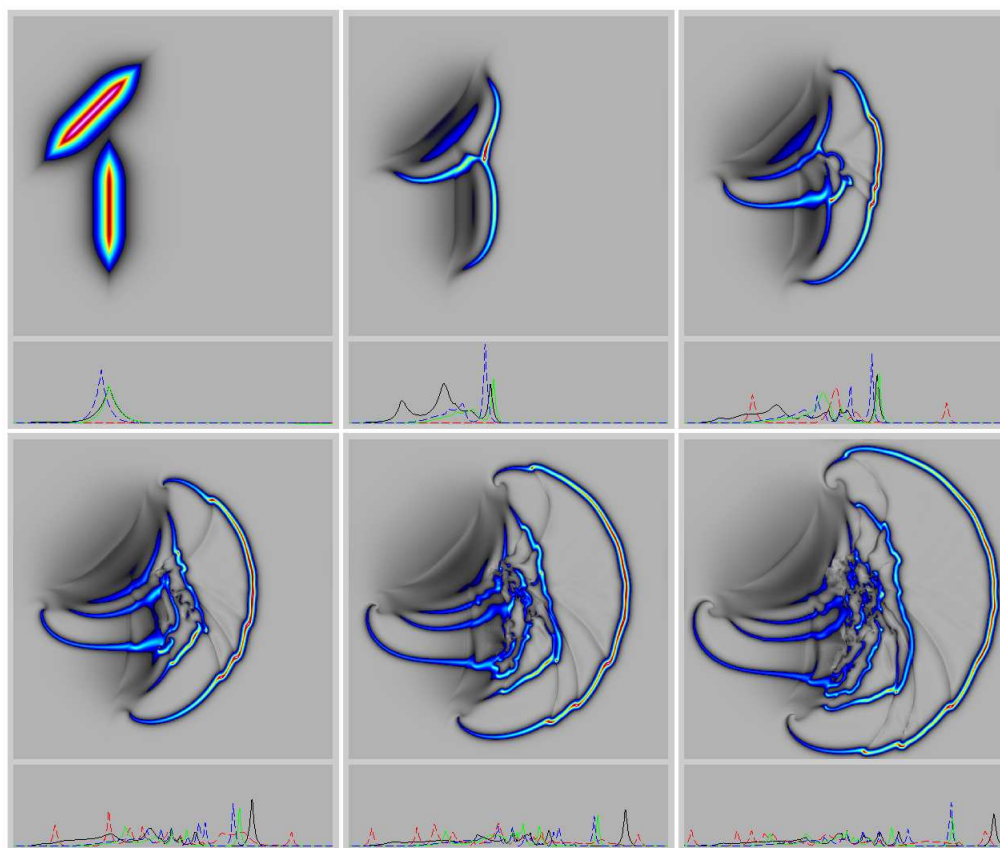


Figure 31: Evolution of the 2d “skew” initial velocity profile with $\alpha = \sigma/4$.

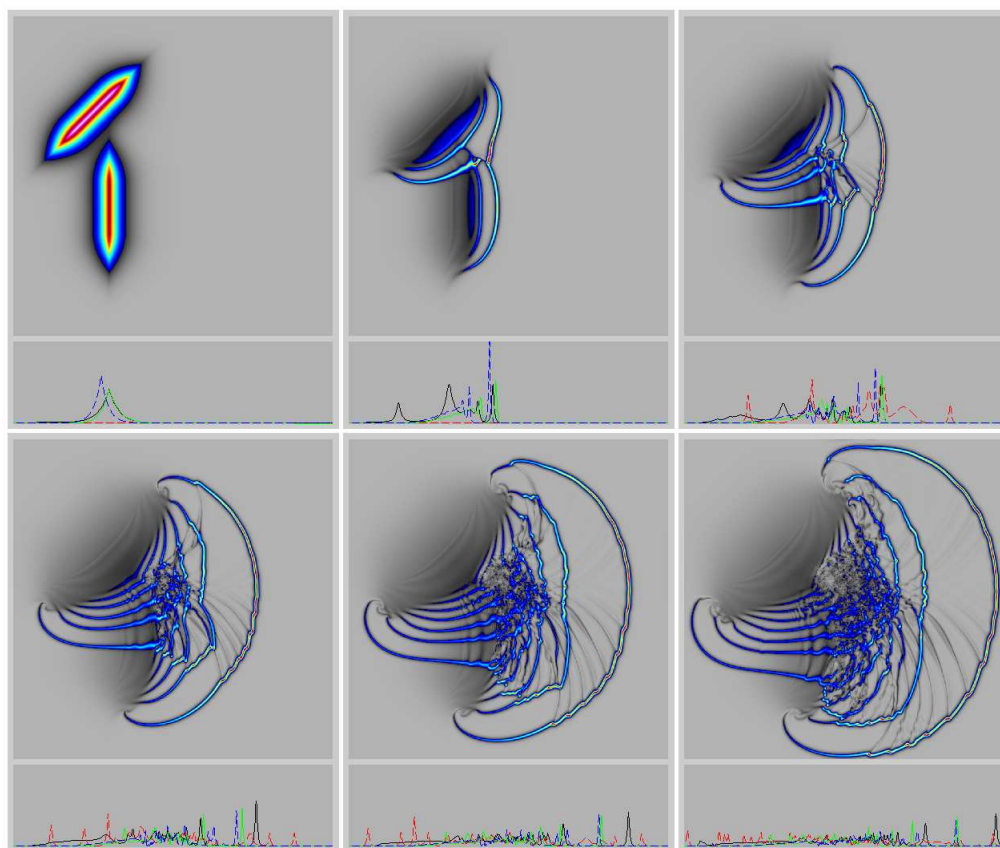


Figure 32: Evolution of the 2d “skew” initial velocity profile with $\alpha = \sigma/8$.

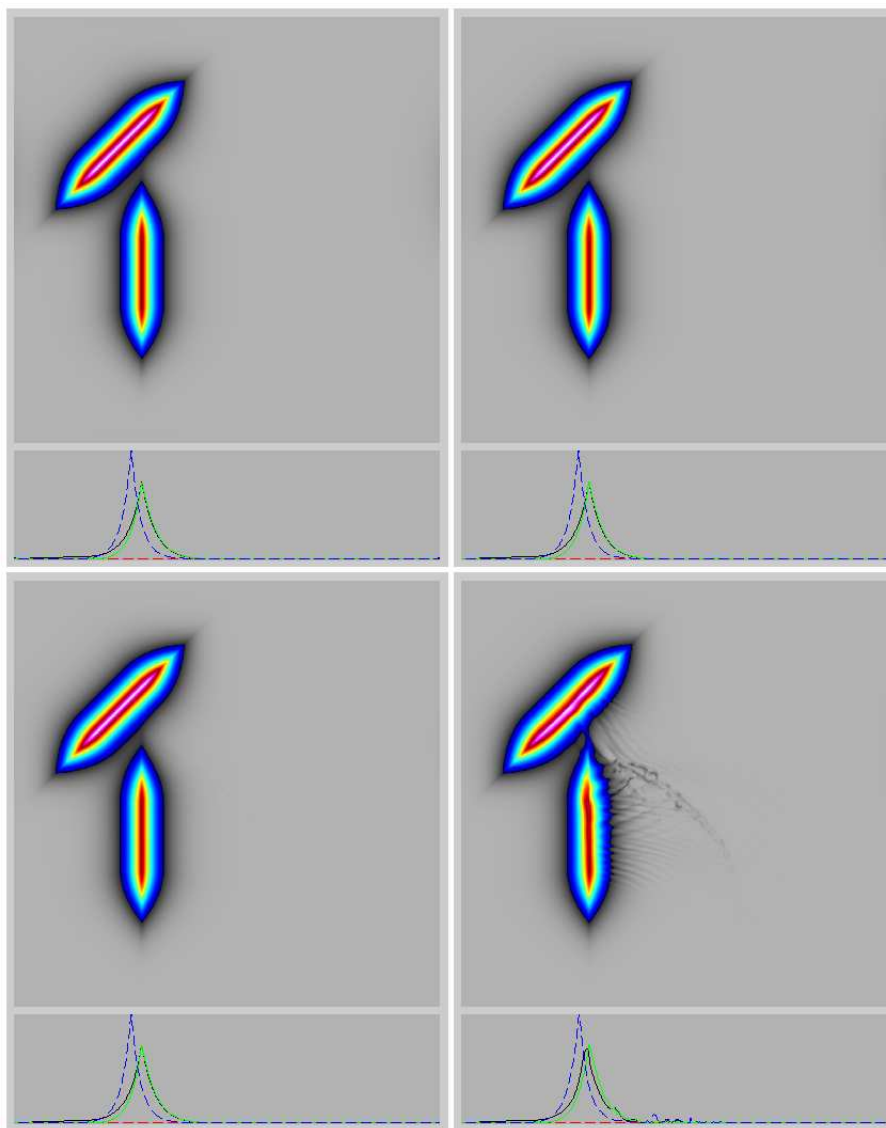


Figure 33: Reconstituted initial velocity profile after time reversal for the 2d “skew” case with $\alpha = \sigma$ (upper left), $\alpha = \sigma/2$ (upper right), $\alpha = \sigma/4$ (lower left), $\alpha = \sigma/8$ (lower right).

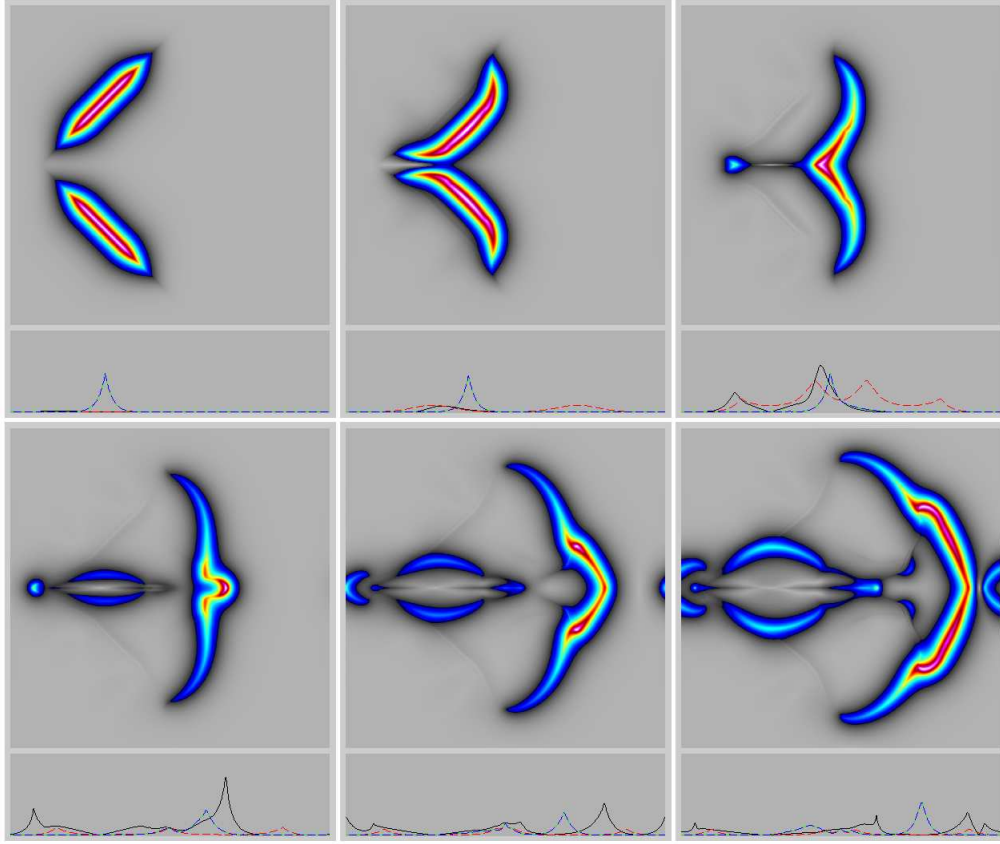


Figure 34: Evolution of the 2d “wedge” initial velocity profile with $\alpha = \sigma$.

reversibility, of order 10 to 20 percent for $\alpha = \sigma/8$, as observed in Figure 38. However, these errors decrease for larger alpha. As we will see in other plots, errors in reversibility tend to arise for smaller values of $\alpha < \sigma$ whenever head-on collisions occur.

9.5 Head-on

The head-on collisions of two offset peakon segments in Figures 39-42 show great complexity. Some of this complexity is due to the process of annihilation and recreation known to occur in the purely 1d antisymmetric head-on collisions of a peakon with its reflection, the antipeakon. At the moment

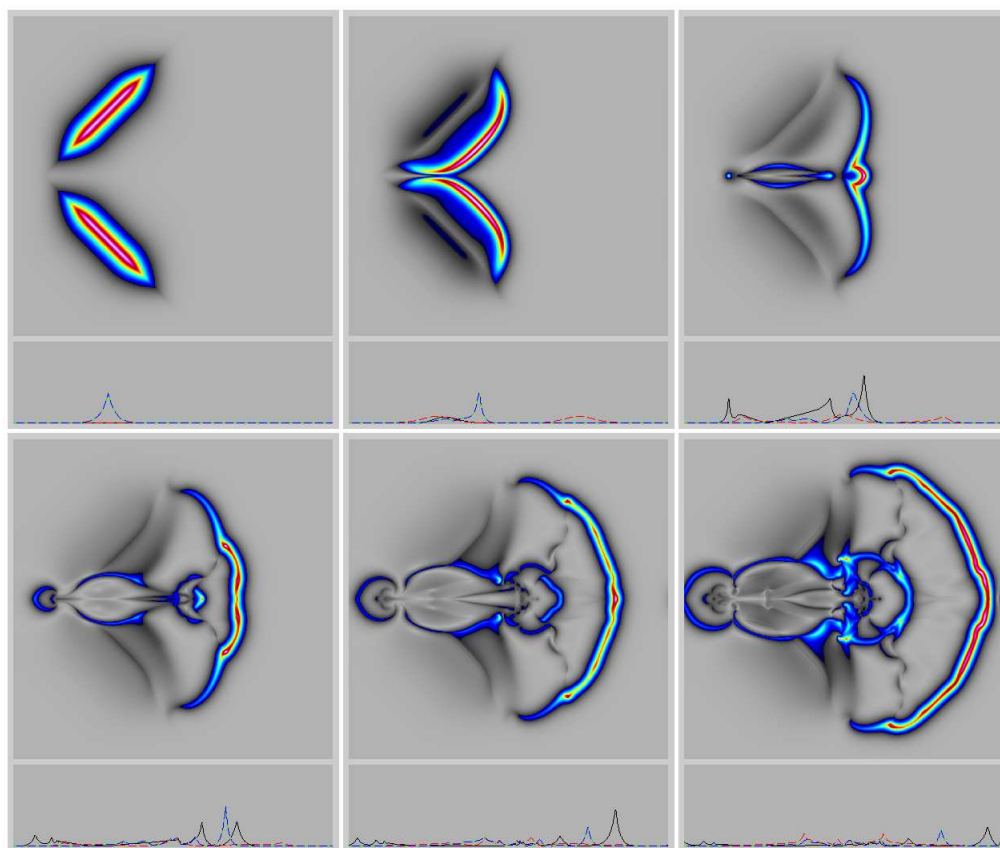


Figure 35: Evolution of the 2d “wedge” initial velocity profile with $\alpha = \sigma/2$.

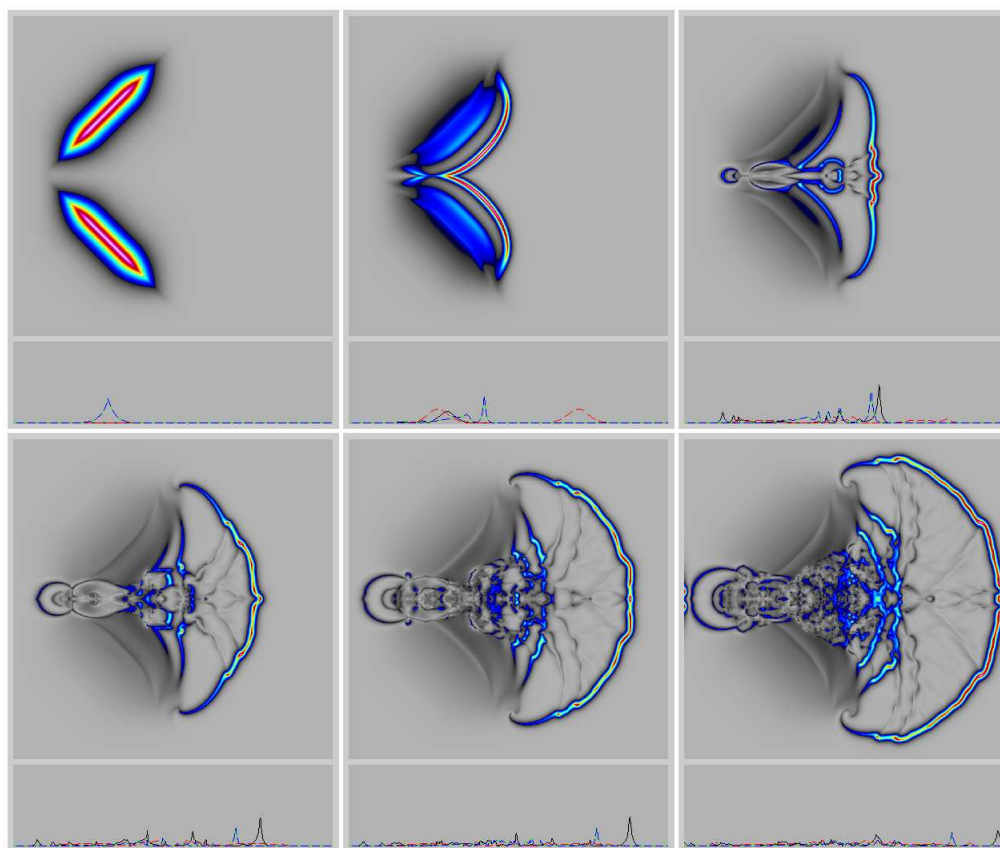


Figure 36: Evolution of the 2d “wedge” initial velocity profile with $\alpha = \sigma/4$.

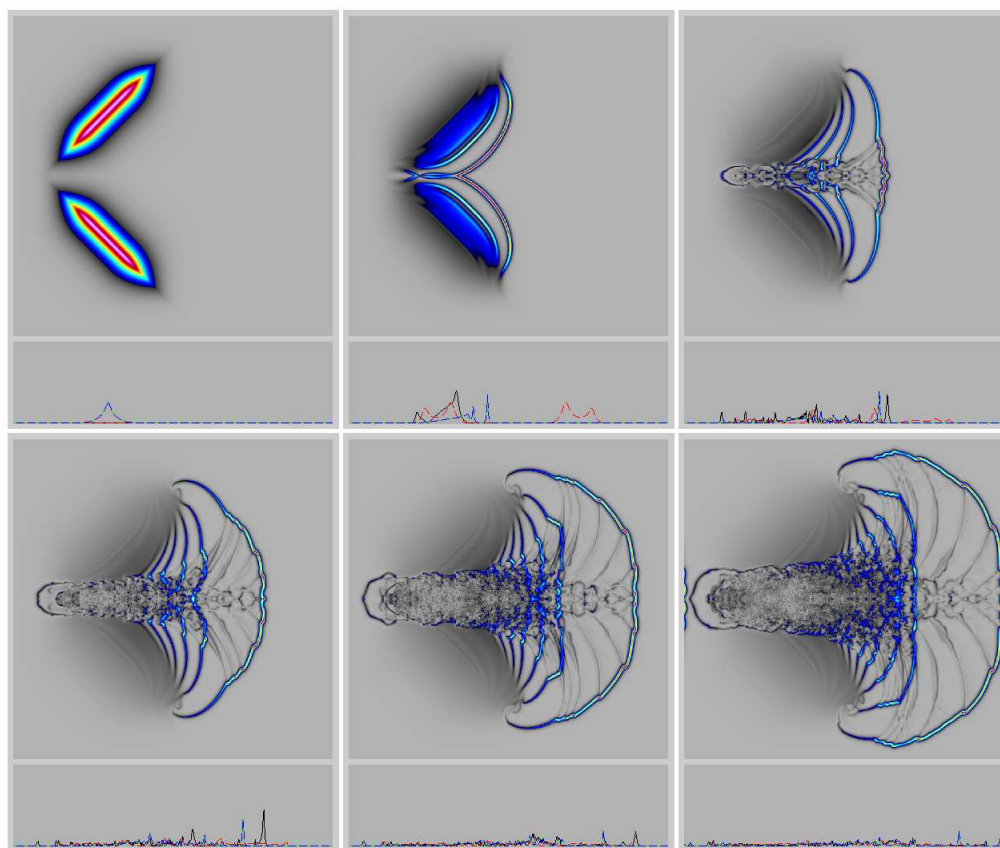


Figure 37: Evolution of the 2d “wedge” initial velocity profile with $\alpha = \sigma/8$.

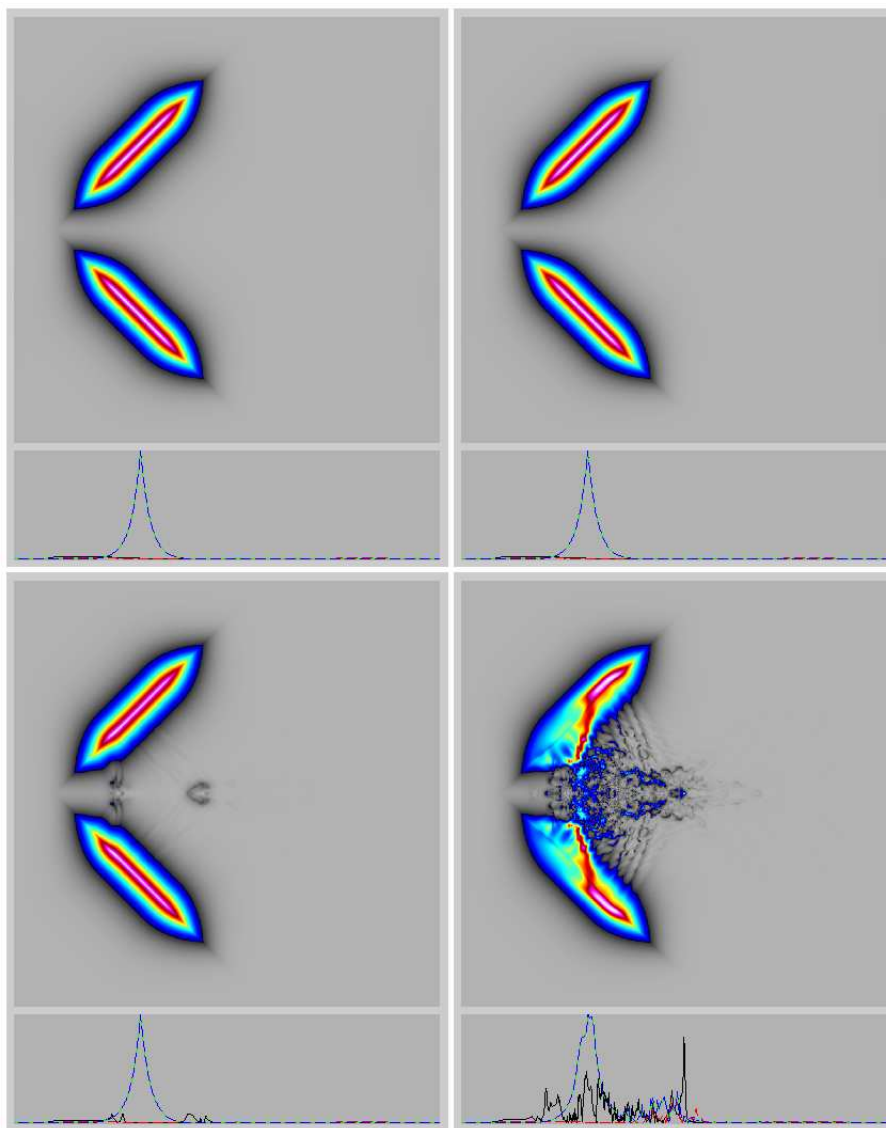


Figure 38: Reconstituted initial velocity profile after time reversal for the 2d “wedge” case with $\alpha = \sigma$ (upper left), $\alpha = \sigma/2$ (upper right), $\alpha = \sigma/4$ (lower left), $\alpha = \sigma/8$ (lower right).

a head-on collision occurs, one sees the blue profiles in the lower panels of Figures 39-42 becoming very steep, exactly as seen in 1d peakon-antipeakon collisions. Thus, the locally 1d collision rules carry over to the 2d case for head-on collisions.

The case $\alpha = \sigma$ in Figure 39 shows the annihilation and recreation expected from the 1d rules. Thereafter, a new feature emerges as the recreated segments disconnect, then eventually reconnect again with segment elements that did not participate in the head-on part of the collision. The first disconnection occurs in the presence of rapid rotation or circulation of the peakon segments, which causes extreme stretching before the disconnection. The later reconnection of these segments occurs less violently.

Once again, peakon profiles are ubiquitous in the lower panels of Figures 39-42.

Time reversal of the head-on collisions shows, for $\alpha = \sigma$, an essentially complete restoration of the initial condition; see Figure 43. However, the cases for smaller alpha ($\alpha = \sigma/4, \sigma/8$) show breakup and head-on collisions occurring simultaneously. These simultaneous processes produce complex mixed states which tend to reverse less accurately, as one might expect, because of the plethora of peaked excitations at small scales.

9.6 Star

Star flows in Figures 44-47 form a variant of wedge flows with fivefold symmetry, instead of simple reflection antisymmetry. The mutual rotation of the overtaking-collision evolution in each case preserves the fivefold symmetry well, and is seen in Figure 48 to be largely reversible. Figures 44-47 each show many reconnections (mergers), until eventually one peakon filament ring surrounds all the others. Again, peakon segments are the ubiquitous feature of the solution. If the evolution were allowed to proceed further, reconnections would tend to produce additional concentric rings of peakon filaments.

9.7 Rotate

Figures 49-52 show how angular (azimuthal) motion couples to radial motion in the plane. Each evolution starts with a circularly symmetric velocity distribution in a Gaussian (not peakon) ring, or annulus, of width alpha, which is initially rotating rigidly at constant angular velocity. The angular

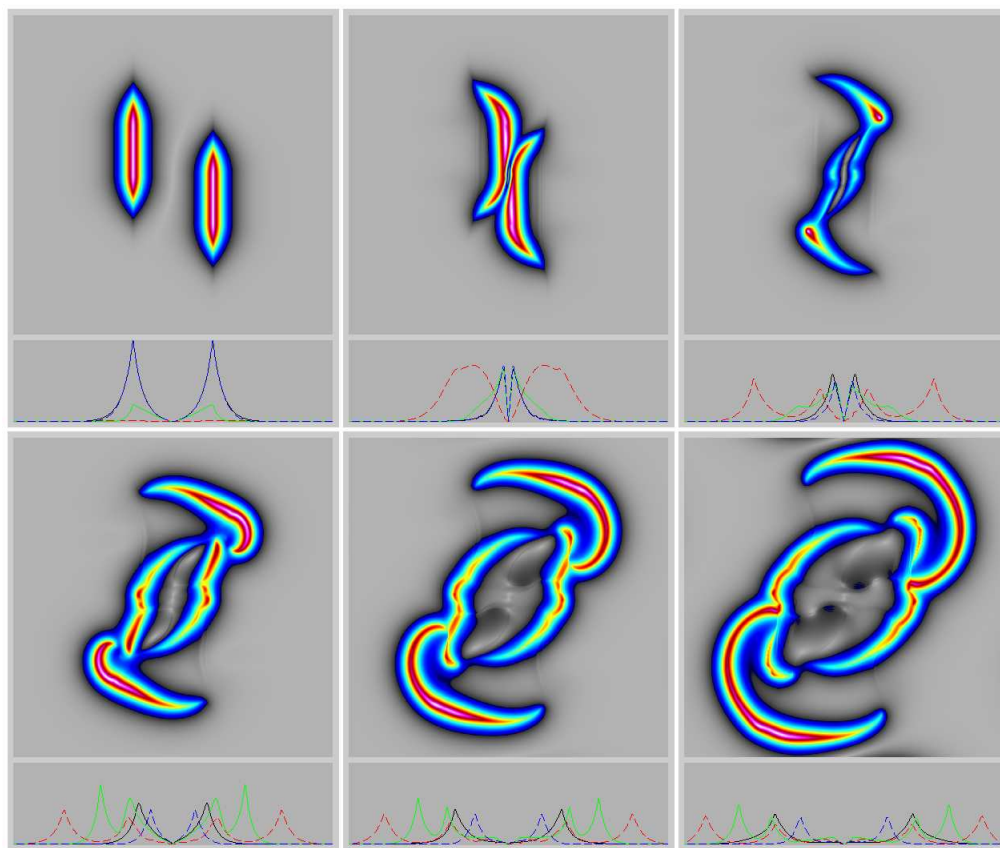


Figure 39: Evolution of the 2d “head-on” initial velocity profile with $\alpha = \sigma$.

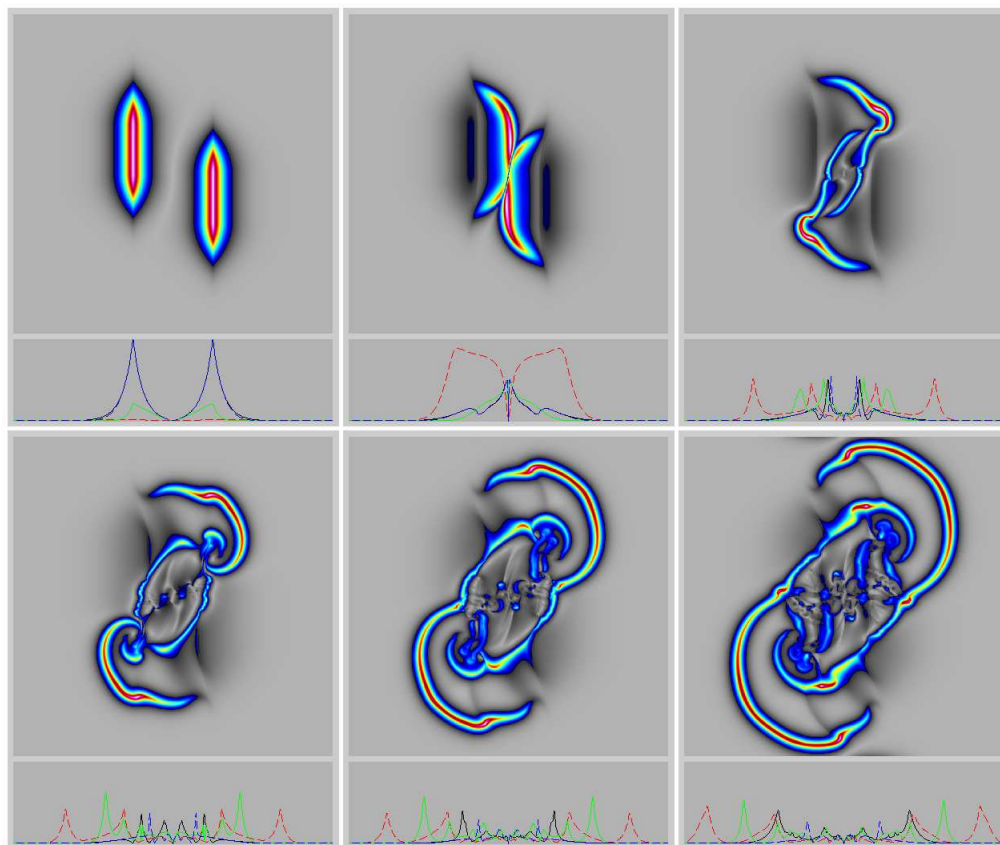


Figure 40: Evolution of the 2d “head-on” initial velocity profile with $\alpha = \sigma/2$.

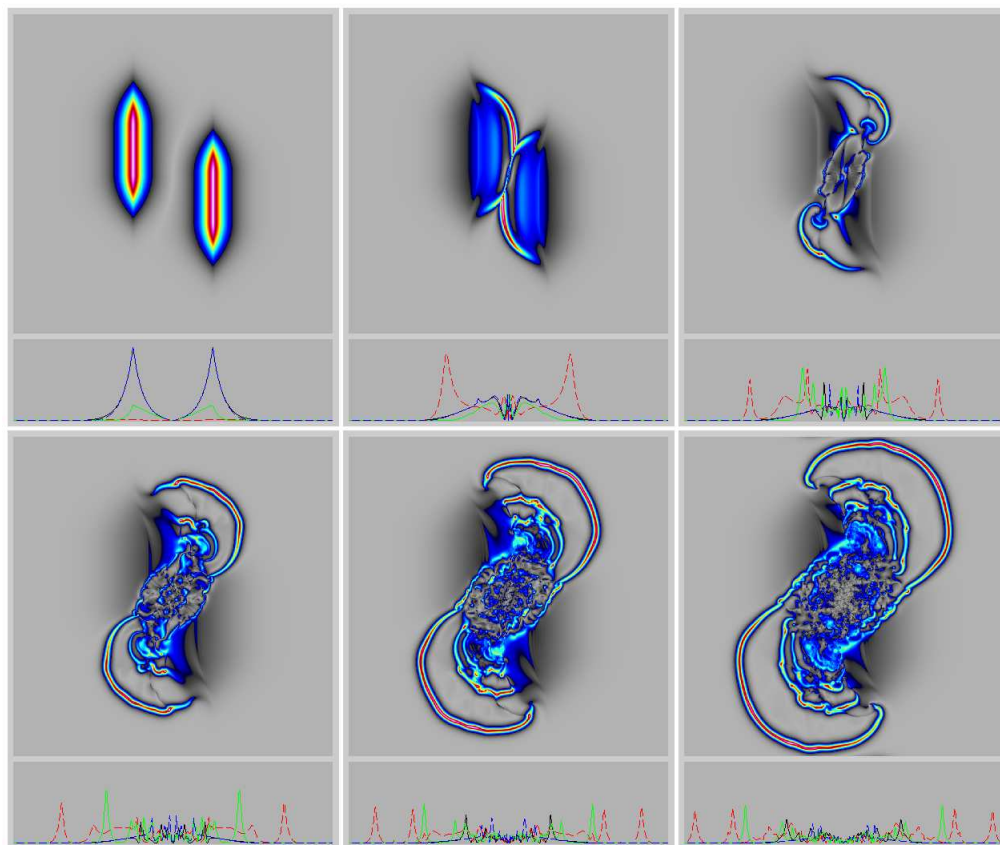


Figure 41: Evolution of the 2d “head-on” initial velocity profile with $\alpha = \sigma/4$.

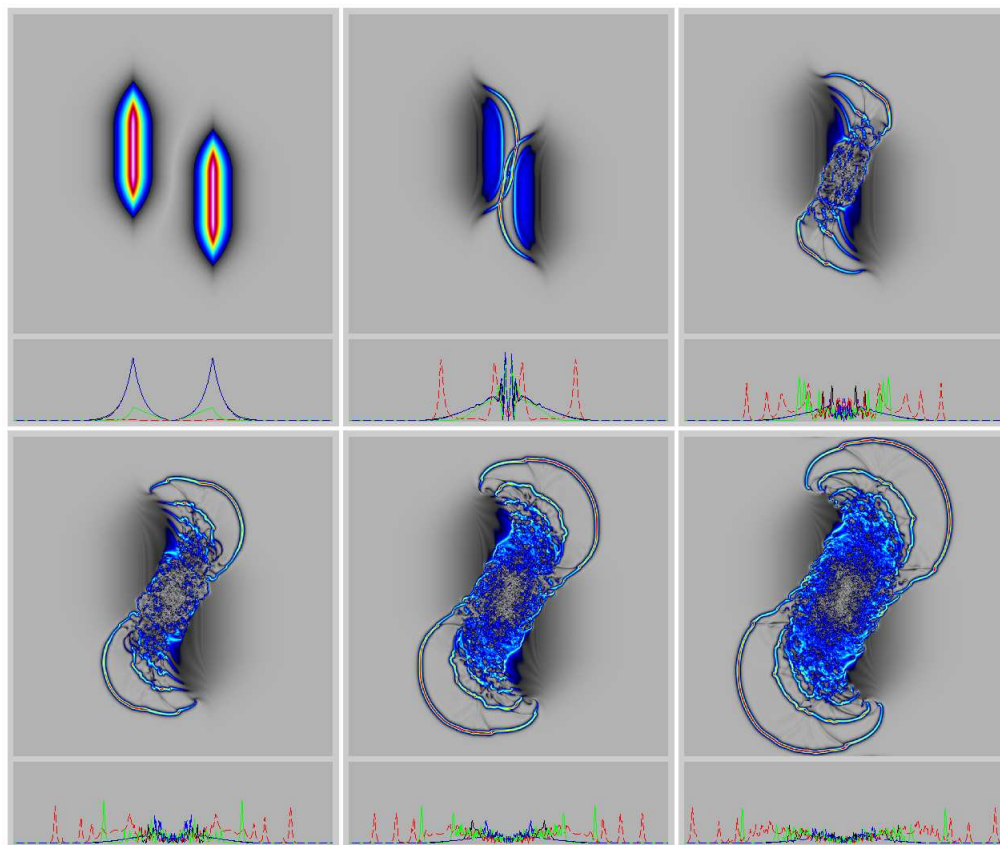


Figure 42: Evolution of the 2d “head-on” initial velocity profile with $\alpha = \sigma/8$.

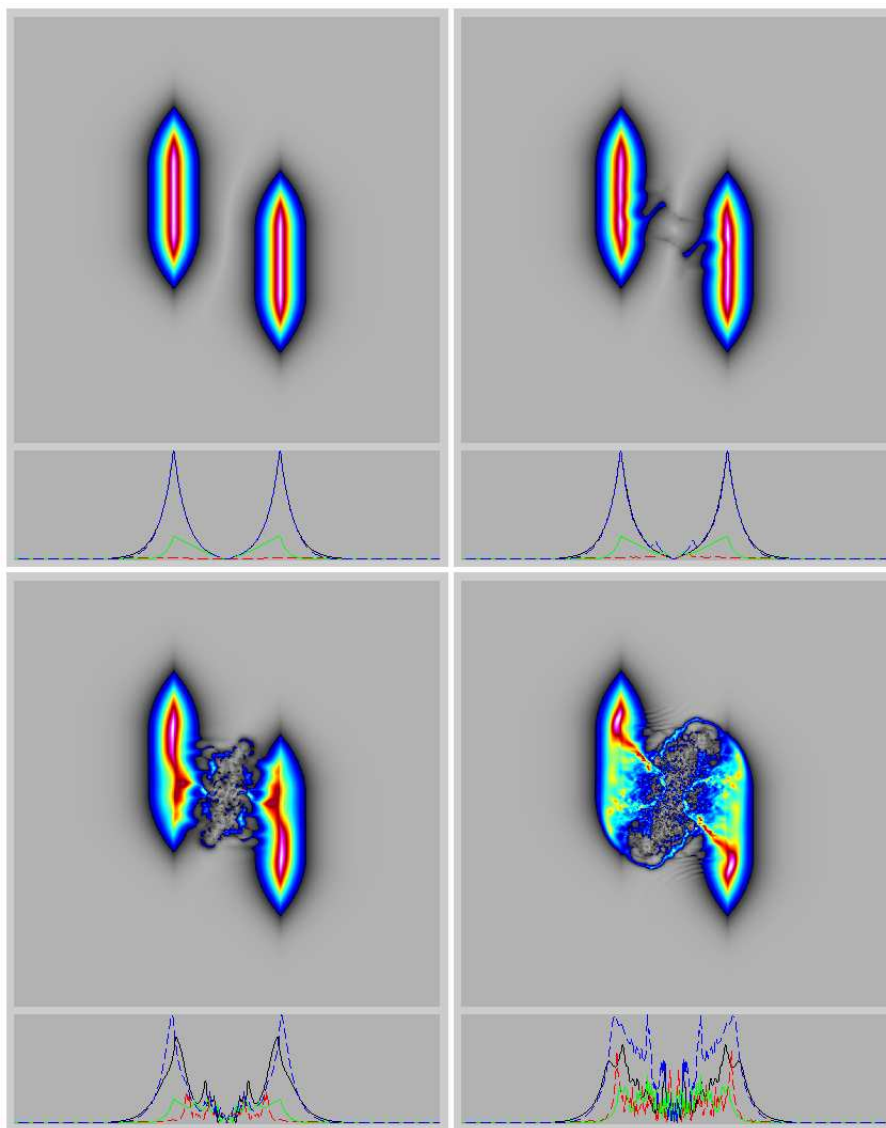


Figure 43: Reconstituted initial velocity profile after time reversal for the 2d “head-on” case with $\alpha = \sigma$ (upper left), $\alpha = \sigma/2$ (upper right), $\alpha = \sigma/4$ (lower left), $\alpha = \sigma/8$ (lower right).

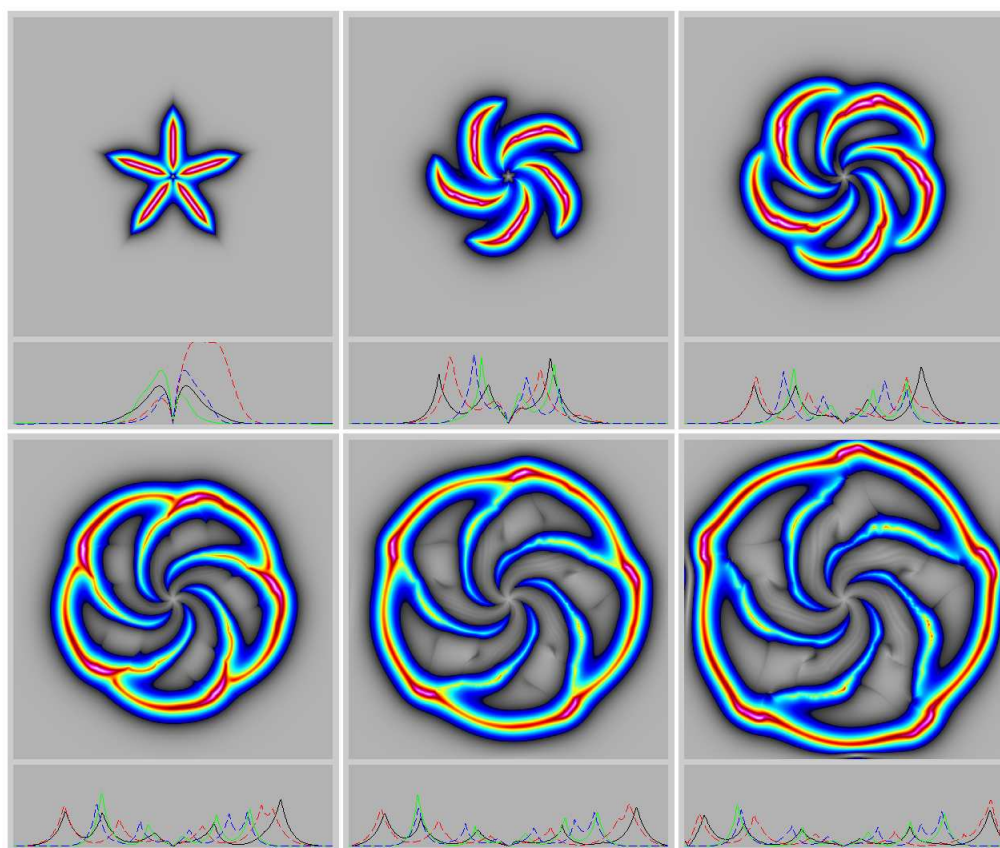


Figure 44: Evolution of the 2d “star” initial velocity profile with $\alpha = \sigma$.

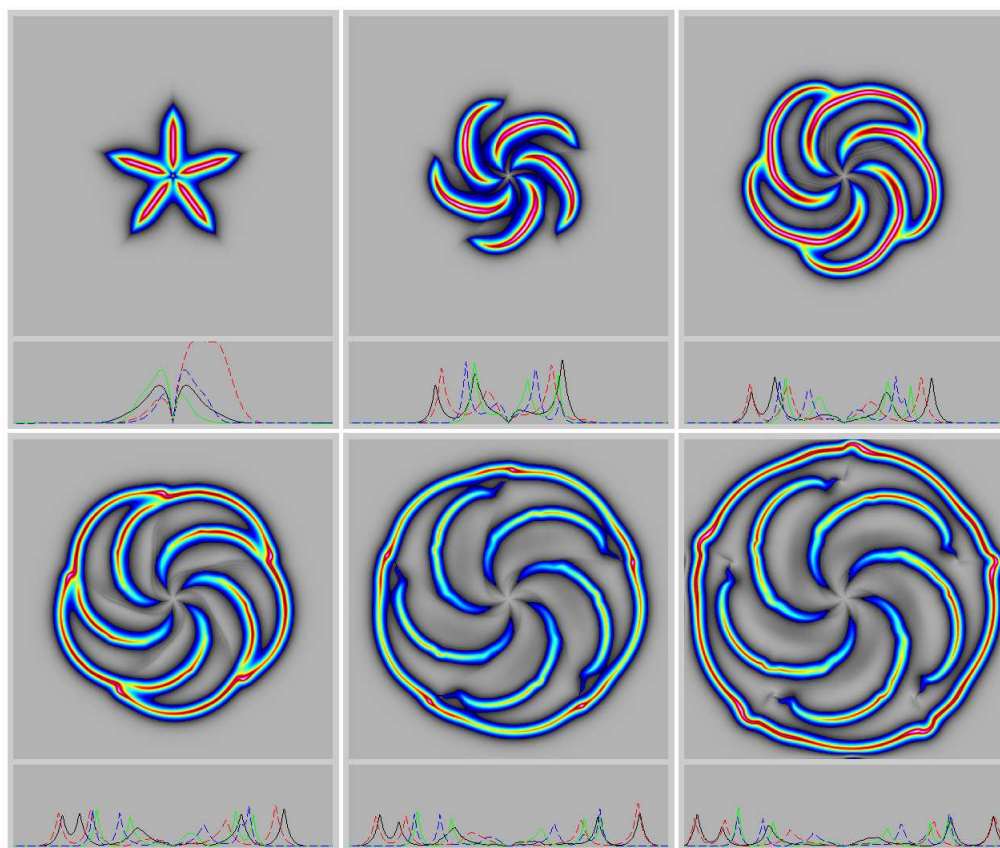


Figure 45: Evolution of the 2d “star” initial velocity profile with $\alpha = \sigma/2$.

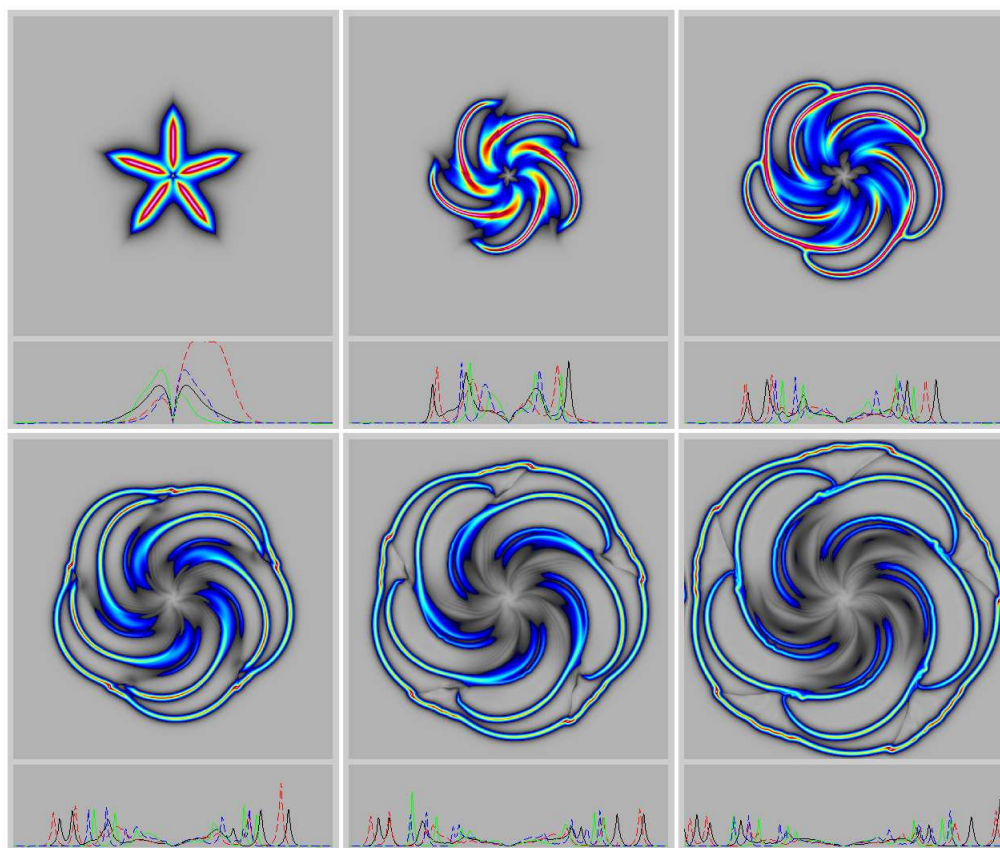


Figure 46: Evolution of the 2d “star” initial velocity profile with $\alpha = \sigma/4$.

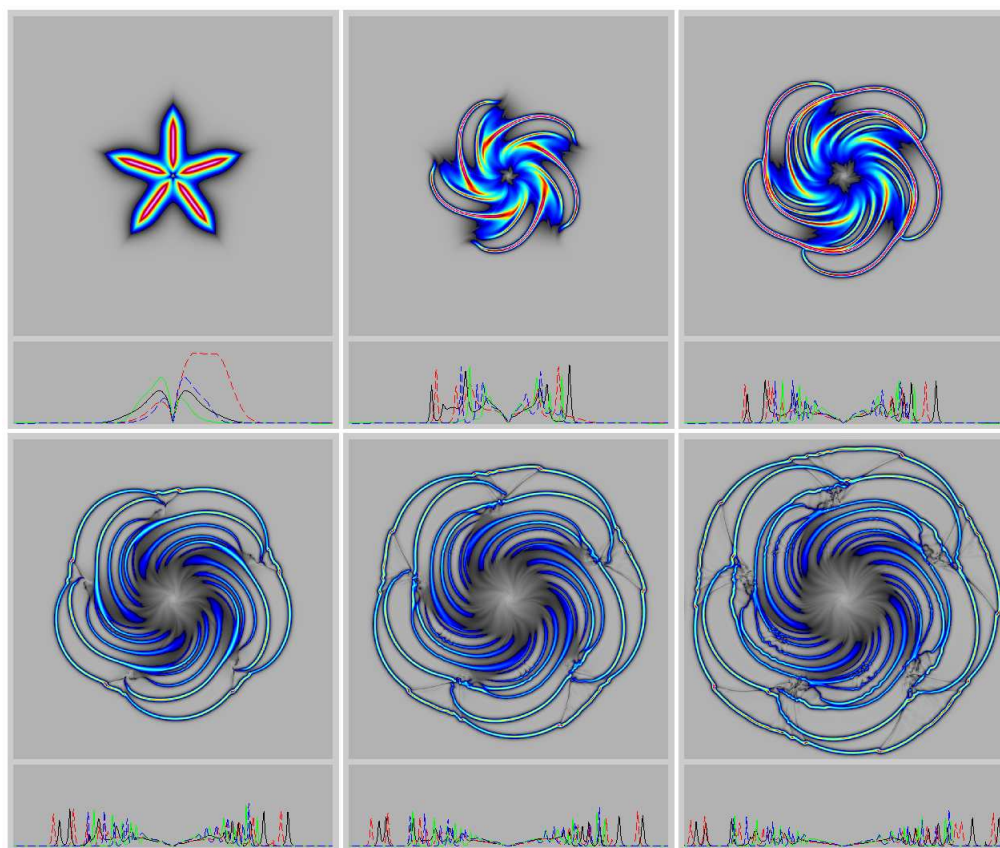


Figure 47: Evolution of the 2d “star” initial velocity profile with $\alpha = \sigma/8$.

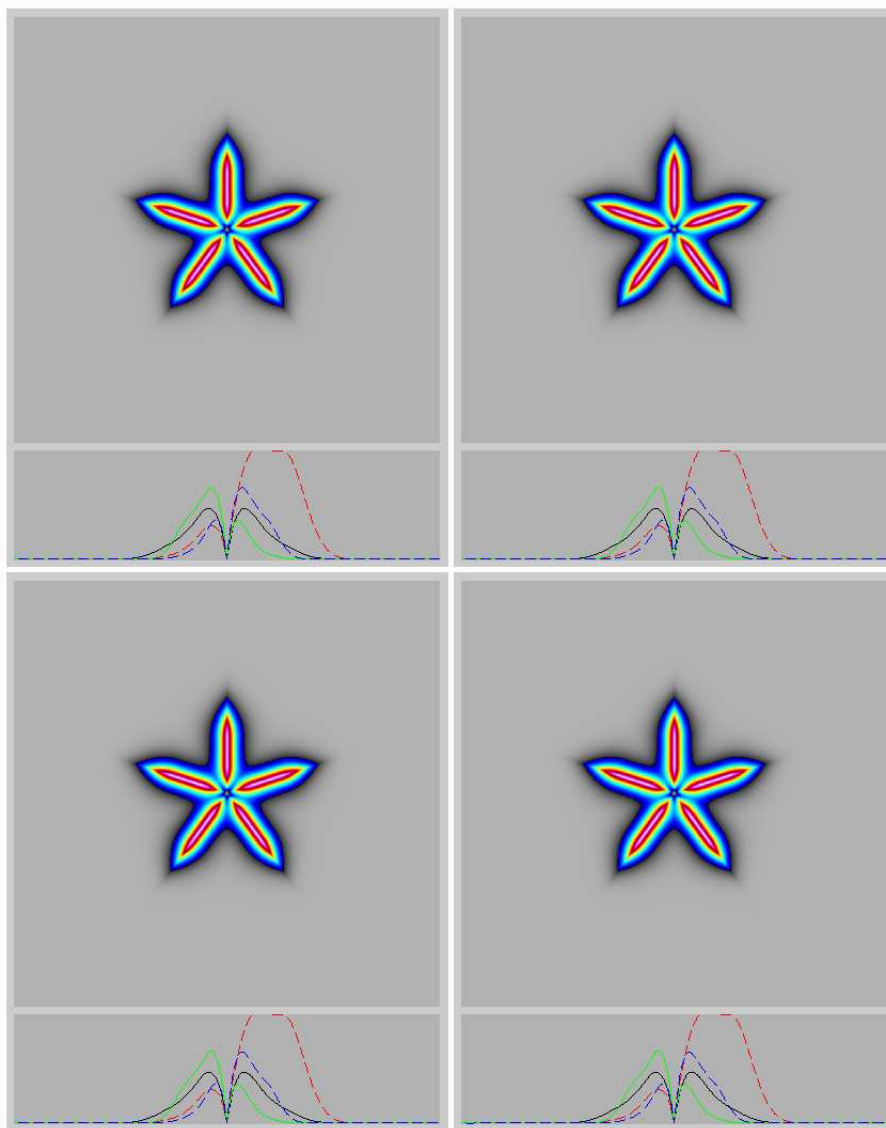


Figure 48: Reconstituted initial velocity profile after time reversal for the 2d “star” case with $\alpha = \sigma$ (upper left), $\alpha = \sigma/2$ (upper right), $\alpha = \sigma/4$ (lower left), $\alpha = \sigma/8$ (lower right).

motion couples to the radial motion by producing a sequence of outward and inward propagating circular peakons. These circular peakons also rotate clockwise (in the same sense as the initial condition) because of conservation of angular momentum. See Holm et al. [25, 26] for more details about circular peakons.

For $\alpha < \sigma$, the first inward propagating circular peakon in Figures 50-52 collapses to the center, then reflects outward and overwhelms the formation of any subsequent inward moving circular peakons. For $\alpha = \sigma$, no inward moving peakons form during the time of the simulation.

Upon reflection from the center, the circular peakon is influenced by the finite Cartesian mesh, especially for smaller alpha (narrower peakons). The reflection interaction with the mesh distorts the outward propagating solution, as seen in the animations, with greater distortion for smaller alpha. This is a severe test of the numerics near the center of symmetry. Nonetheless, time reversal from the final velocity profile reconstitutes the initial condition to within less than one percent, as seen in Figure 53. This illustrates that accurate time reversal to the initial condition does not guarantee accuracy of the solution during the forward evolution. However, it does show that even in a somewhat distorted solution, dissipation plays little role in the numerical simulation.

9.8 Right

In the simulations shown in Figures 54-57, the velocity distribution is initially a Gaussian ring in magnitude, uniformly pointed rightward along the x axis. The right outer side of the ring produces diverging peakon contact curves, which slow as they propagate outward. The left inner side of the ring, however, produces converging peakon contact curves, which accelerate as they converge, undergo a strong interaction along the axis, then break again into contact curves still moving rightward, approaching the previous divergent peakon curves and colliding with them from behind. These overtaking collisions impart momentum but they do not produce reconnections.

After the collisions, a complex flow remains near the axis, in which one also sees hot spots at kinks in the contact curves, with trailing memory wisps behind them.

The lower panels show peakon profiles with high wavenumber oscillations (possibly noise) in the complex flow region remaining behind near the axis. Except for the smallest case of $\alpha = \sigma/8$, all of the time-reversed runs re-

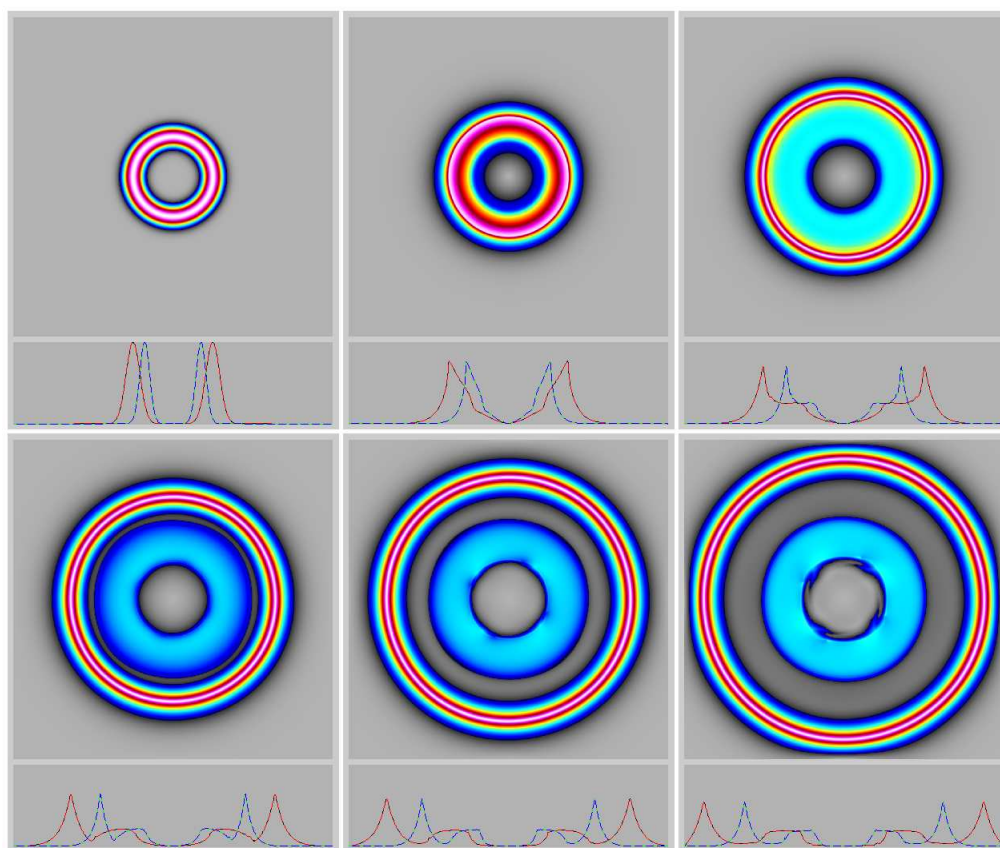


Figure 49: Evolution of the 2d “rotate” initial velocity profile with $\alpha = \sigma$.

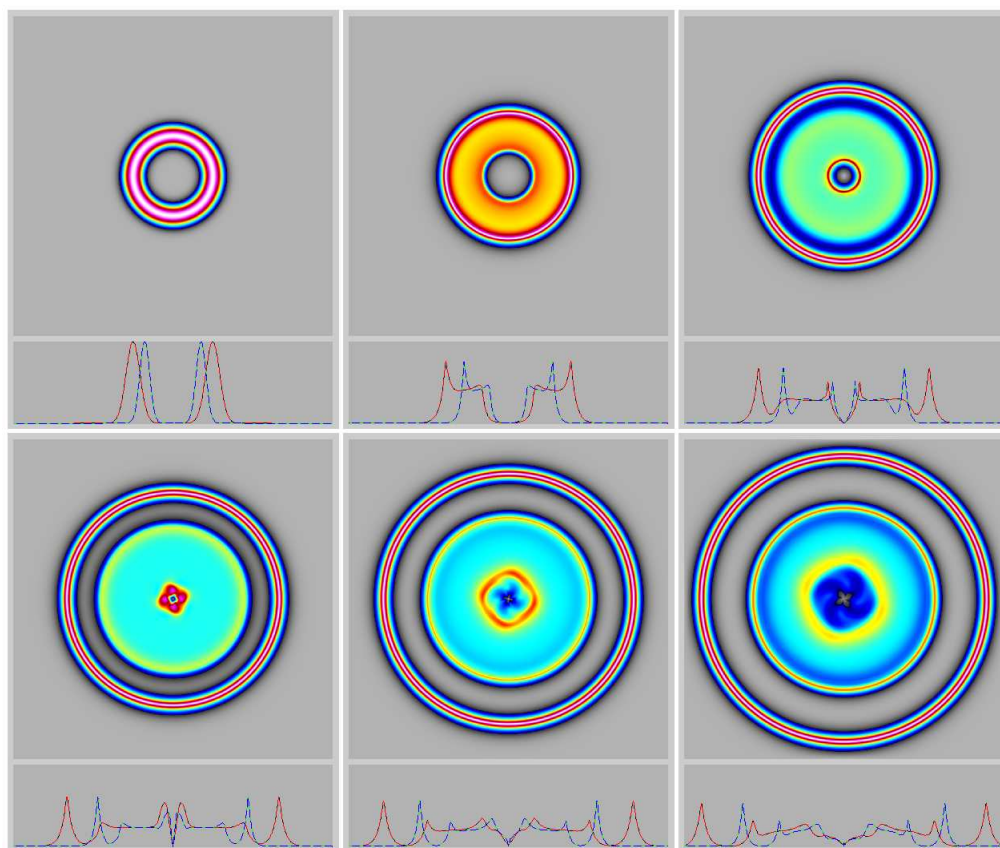


Figure 50: Evolution of the 2d “rotate” initial velocity profile with $\alpha = \sigma/2$.

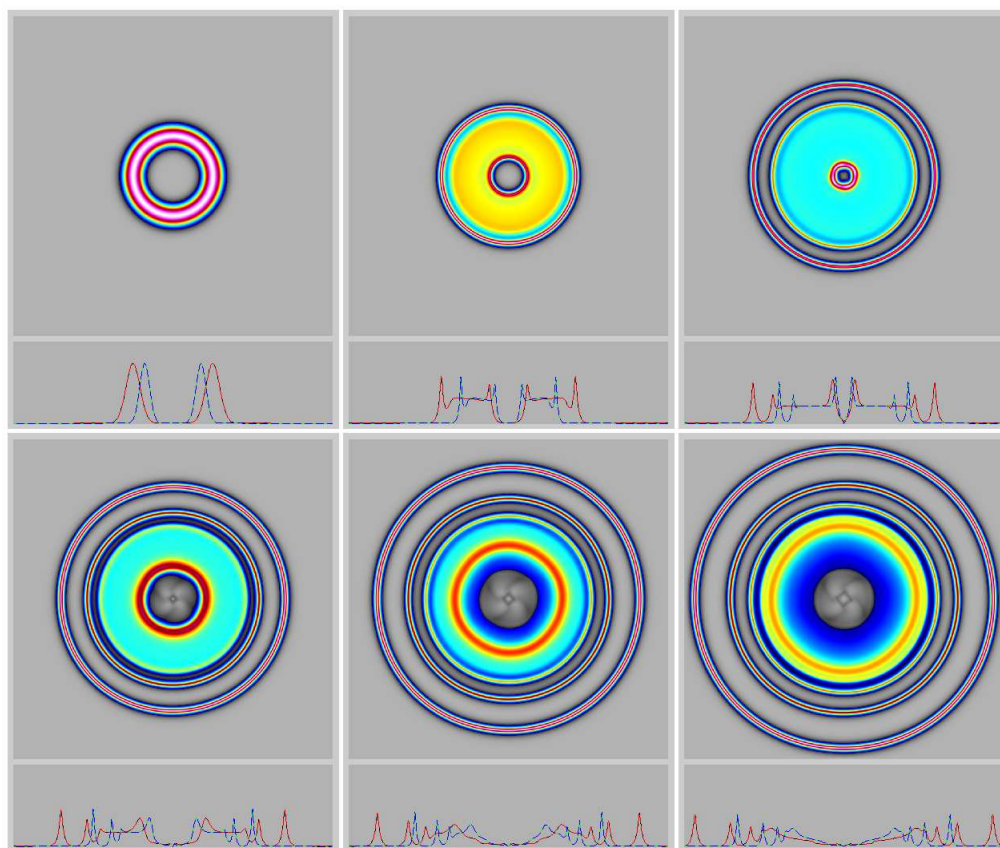


Figure 51: Evolution of the 2d “rotate” initial velocity profile with $\alpha = \sigma/4$.

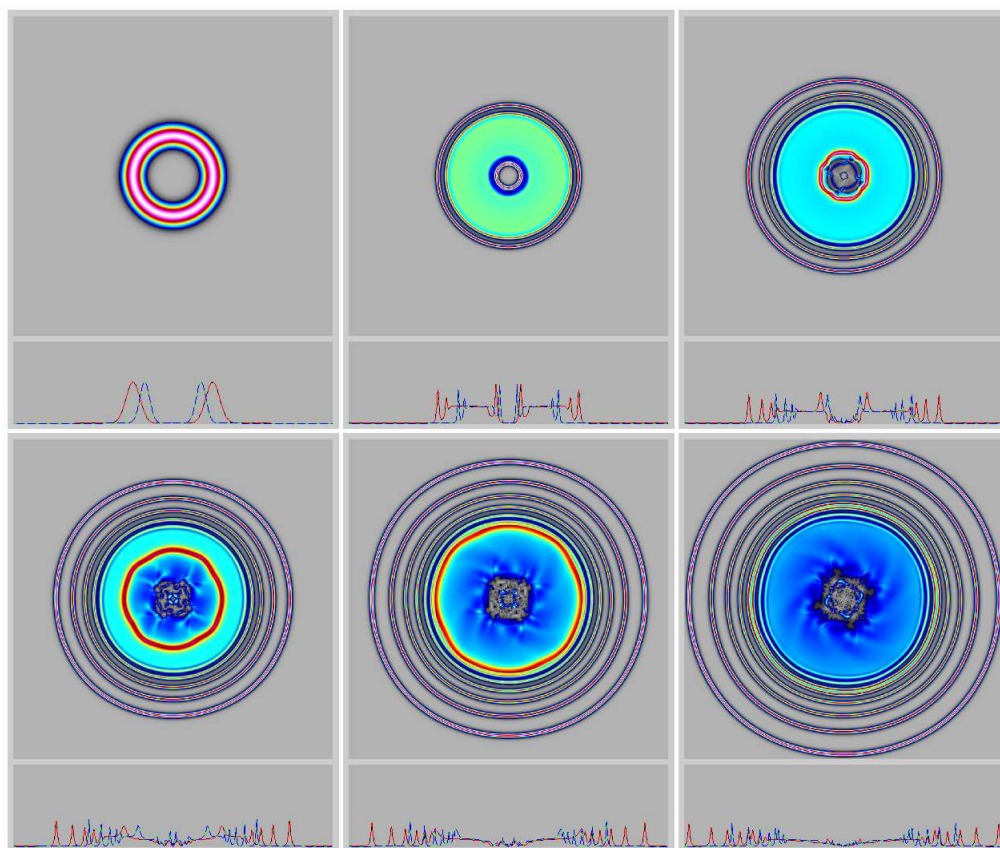


Figure 52: Evolution of the 2d “rotate” initial velocity profile with $\alpha = \sigma/8$.

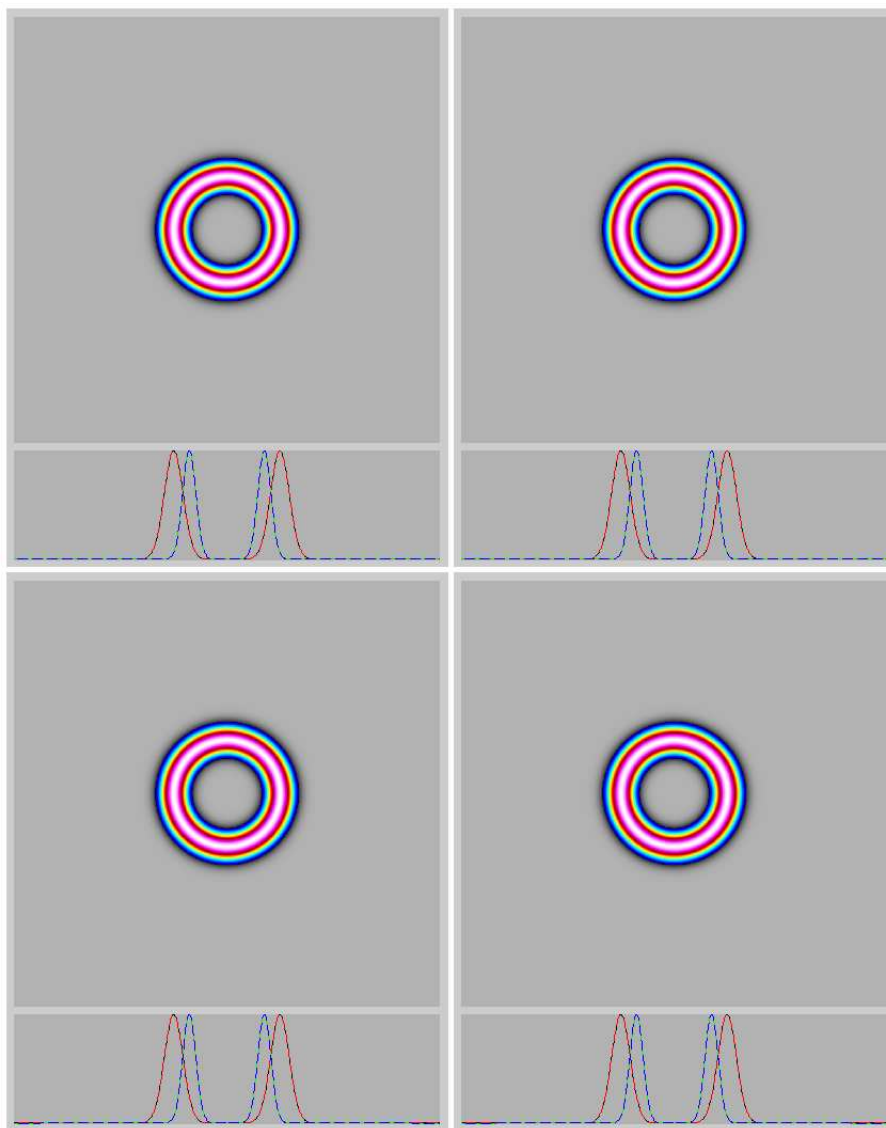


Figure 53: Reconstituted initial velocity profile after time reversal for the 2d “rotate” case with $\alpha = \sigma$ (upper left), $\alpha = \sigma/2$ (upper right), $\alpha = \sigma/4$ (lower left), $\alpha = \sigma/8$ (lower right).

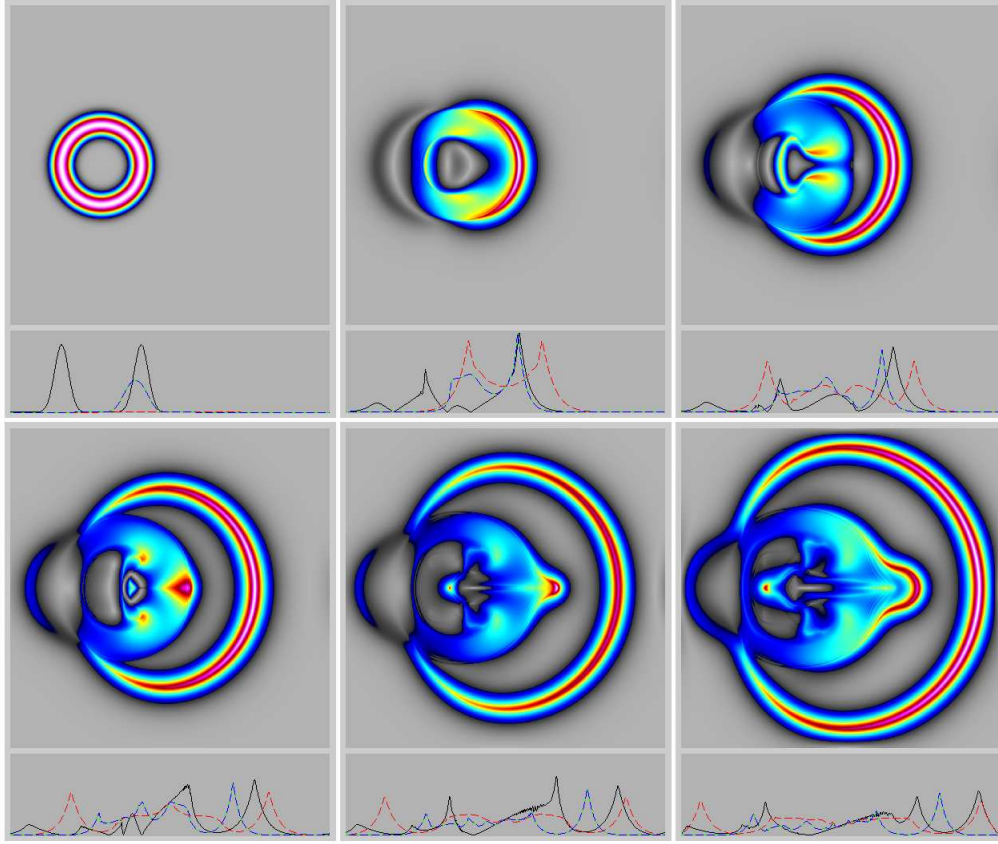


Figure 54: Evolution of the 2d “right” initial velocity profile with $\alpha = \sigma$.

assemble into the Gaussian ring without significant distortion, as diagnosed by the black profile in the lower panel of the time reversed runs in Figure 58.

9.9 Inout

In Figures 59-62 we start with an initial Gaussian ring of width α in speed, with an angular distribution of $-(\sin \theta, \cos \theta) \exp(-(r - r_0)^2/\sigma^2)$ for the direction of the velocity. Consequently, the motion is inward along the positive diagonal and outward along the negative diagonal. The outward motion breaks into a sequence of curved peakon segments of width α , as usual. The inward motion also produces peakon segments, which however

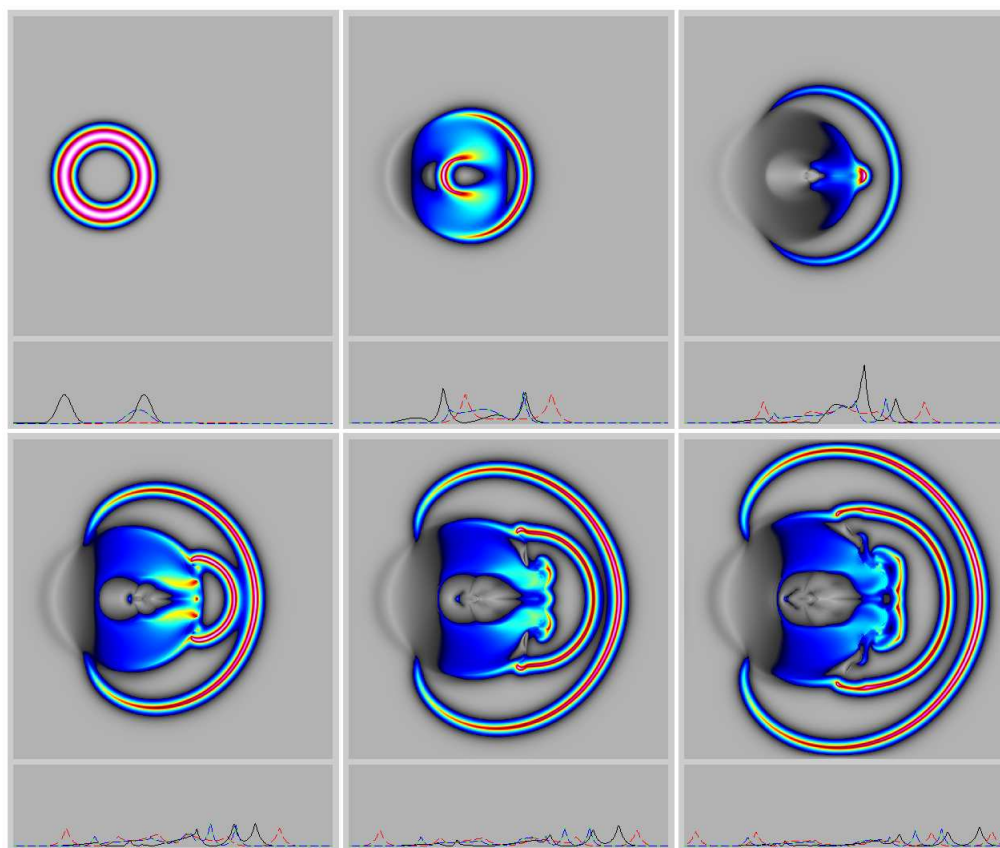


Figure 55: Evolution of the 2d “right” initial velocity profile with $\alpha = \sigma/2$.

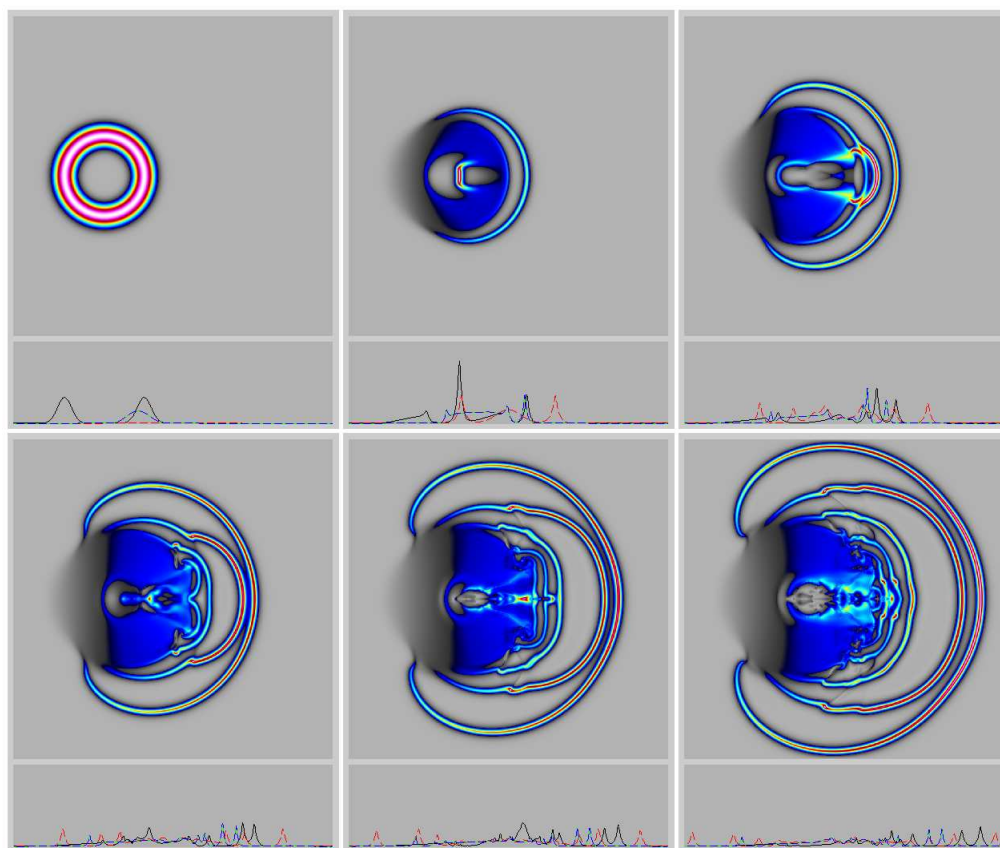


Figure 56: Evolution of the 2d “right” initial velocity profile with $\alpha = \sigma/4$.

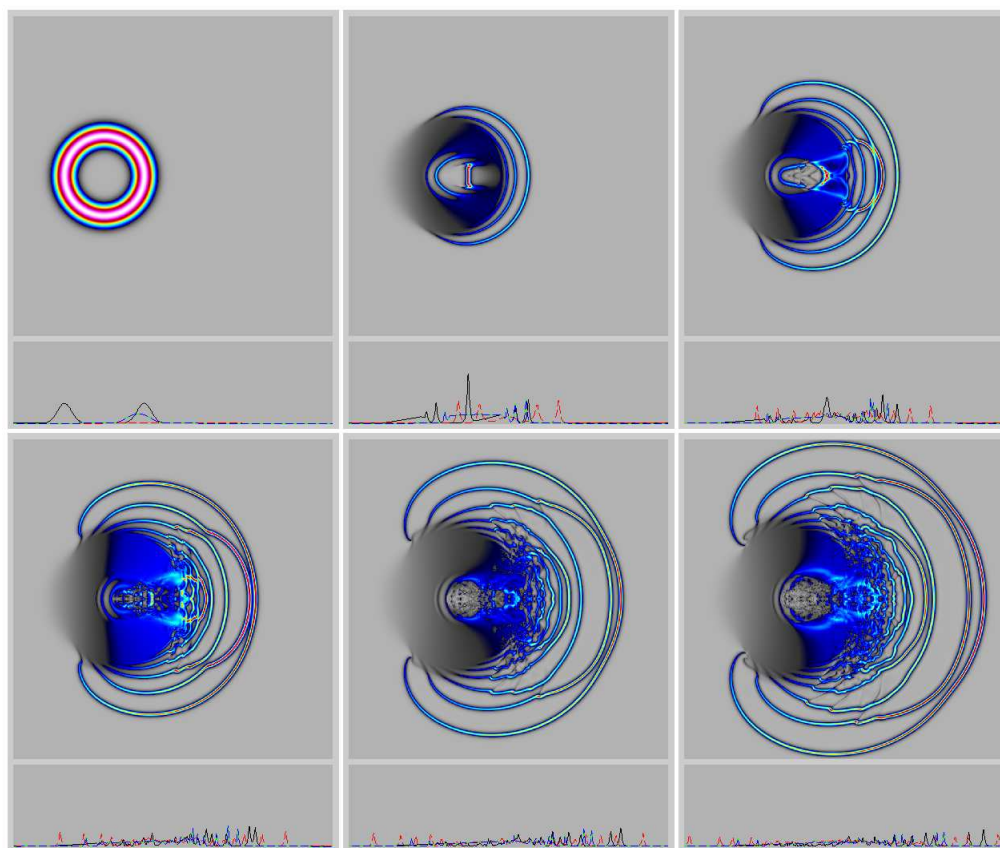


Figure 57: Evolution of the 2d “right” initial velocity profile with $\alpha = \sigma/8$.

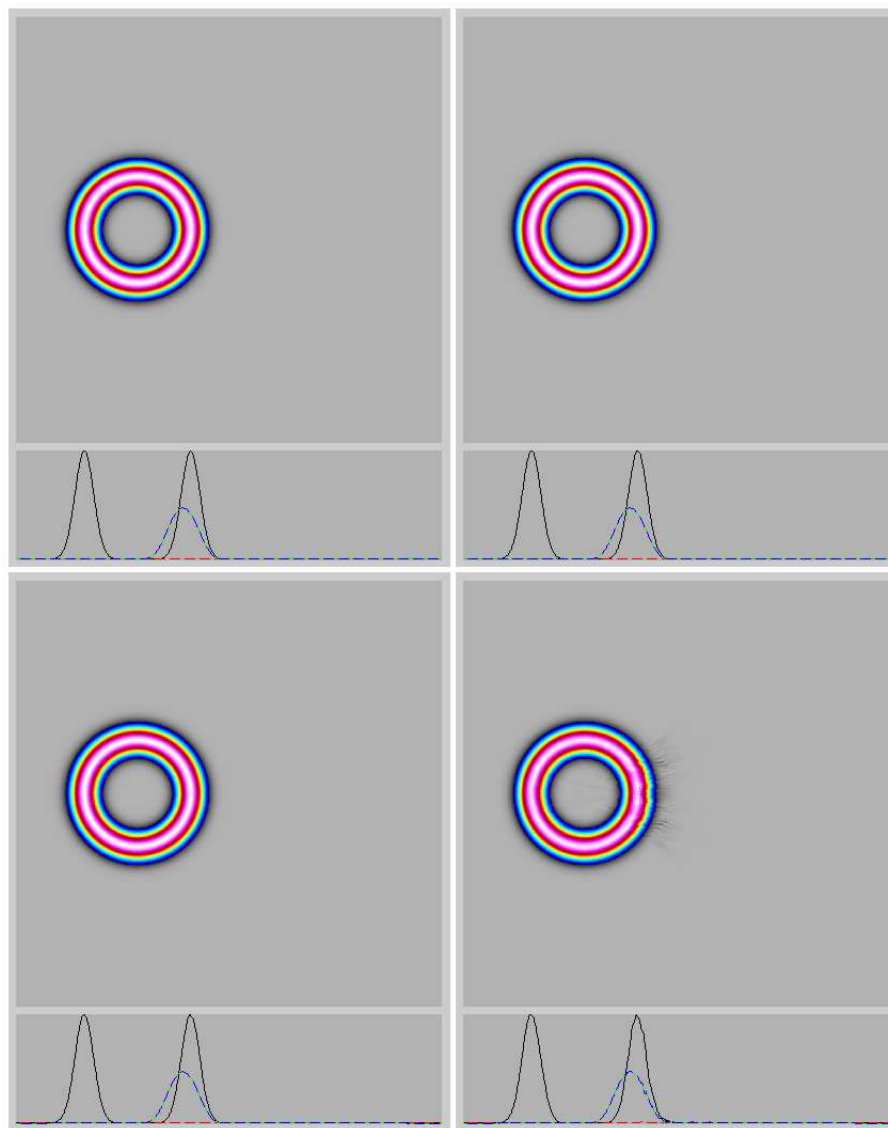


Figure 58: Reconstituted initial velocity profile after time reversal for the 2d “right” case with $\alpha = \sigma$ (upper left), $\alpha = \sigma/2$ (upper right), $\alpha = \sigma/4$ (lower left), $\alpha = \sigma/8$ (lower right).

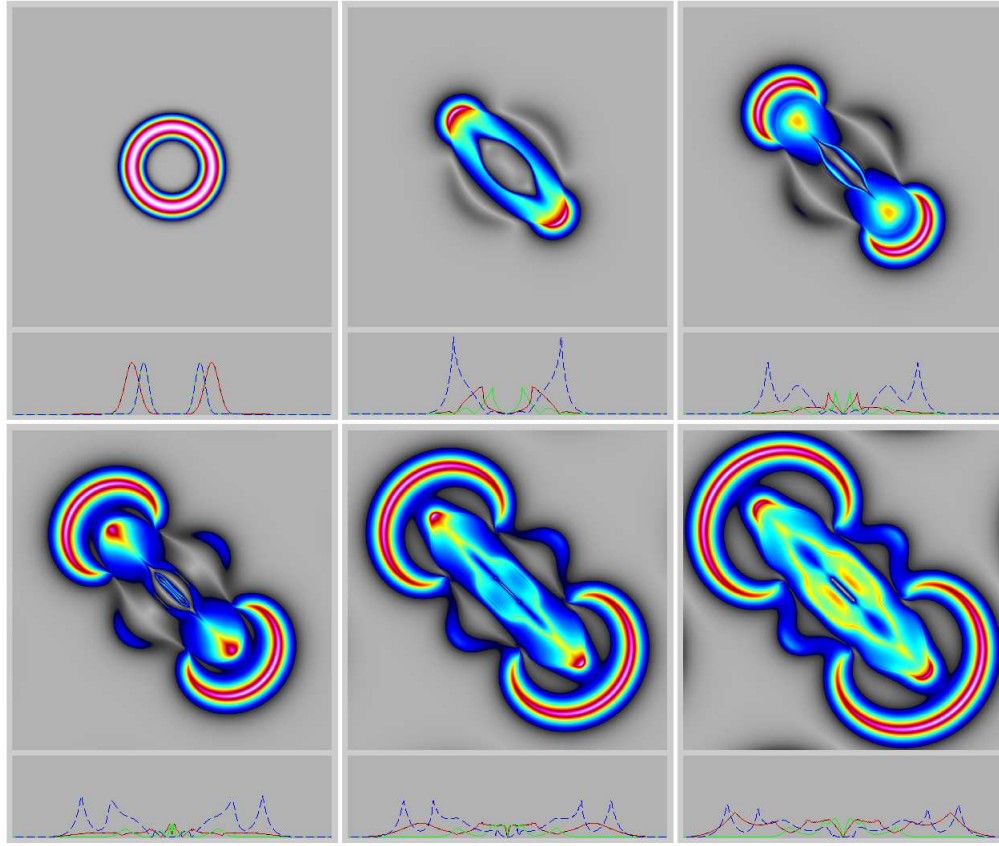


Figure 59: Evolution of the 2d “inout” initial velocity profile with $\alpha = \sigma$.

undergo head-on collisions, so that they annihilate, recreate and re-emerge moving along the positive diagonal.

The blue profiles in the lower panels of Figures 59-62 show the breakup of the outward motion into peakon profiles. The green profiles on the lower panel show the head-on collisions of the peakon profiles of the inward motion. The inward moving head-on collisions leave a residue of complex flow.

Time reversal in this case shows severe distortion of the initial condition for the smaller values $\alpha = \sigma/8$ and $\alpha = \sigma/4$, but not for the larger values $\alpha = \sigma/2$ and $\alpha = \sigma$. See Figure 63.

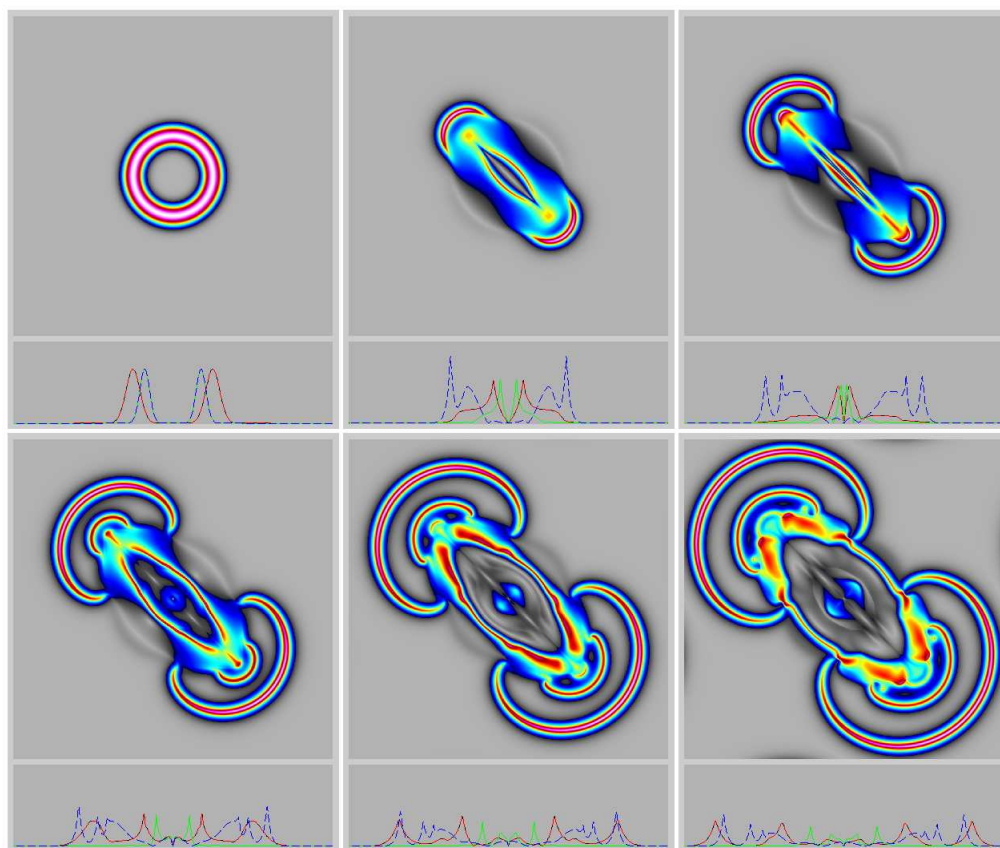


Figure 60: Evolution of the 2d “inout” initial velocity profile with $\alpha = \sigma/2$.

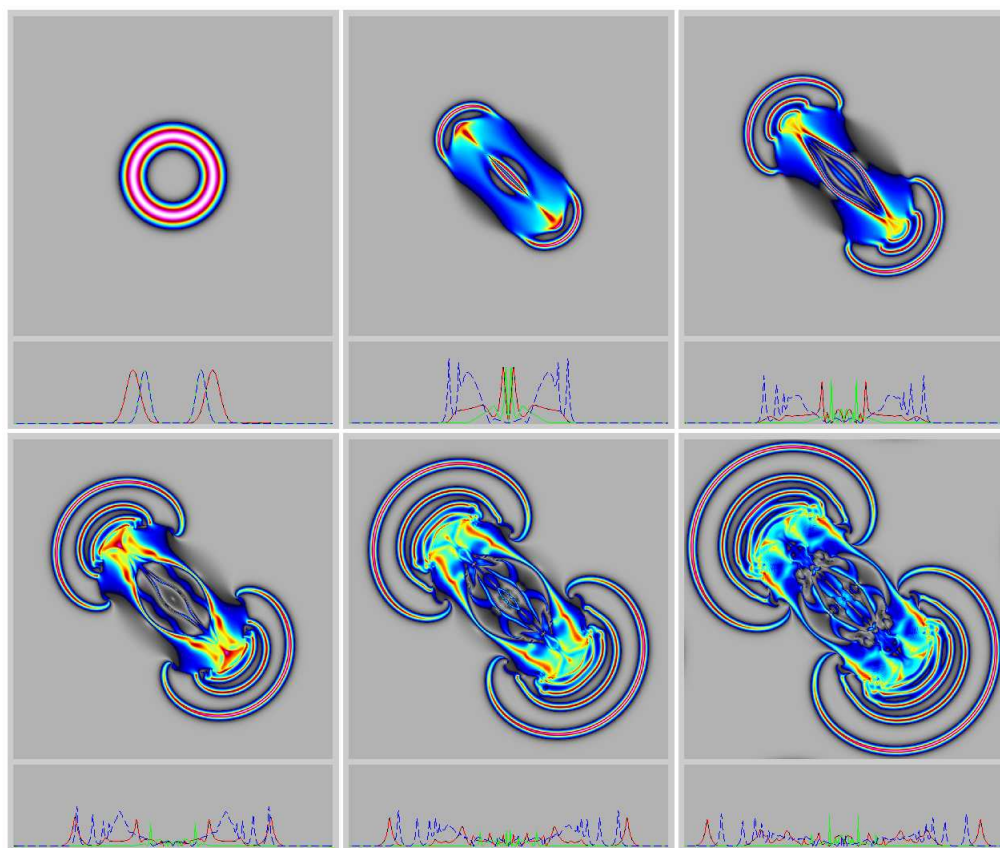


Figure 61: Evolution of the 2d “inout” initial velocity profile with $\alpha = \sigma/4$.

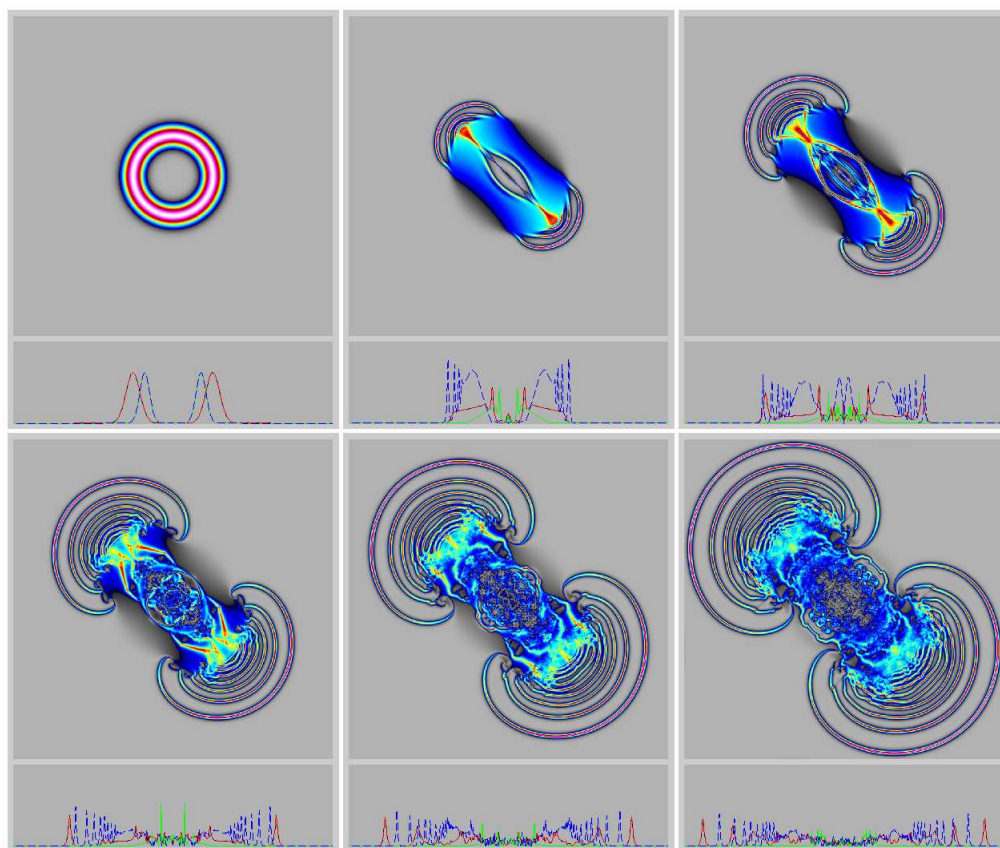


Figure 62: Evolution of the 2d “inout” initial velocity profile with $\alpha = \sigma/8$.

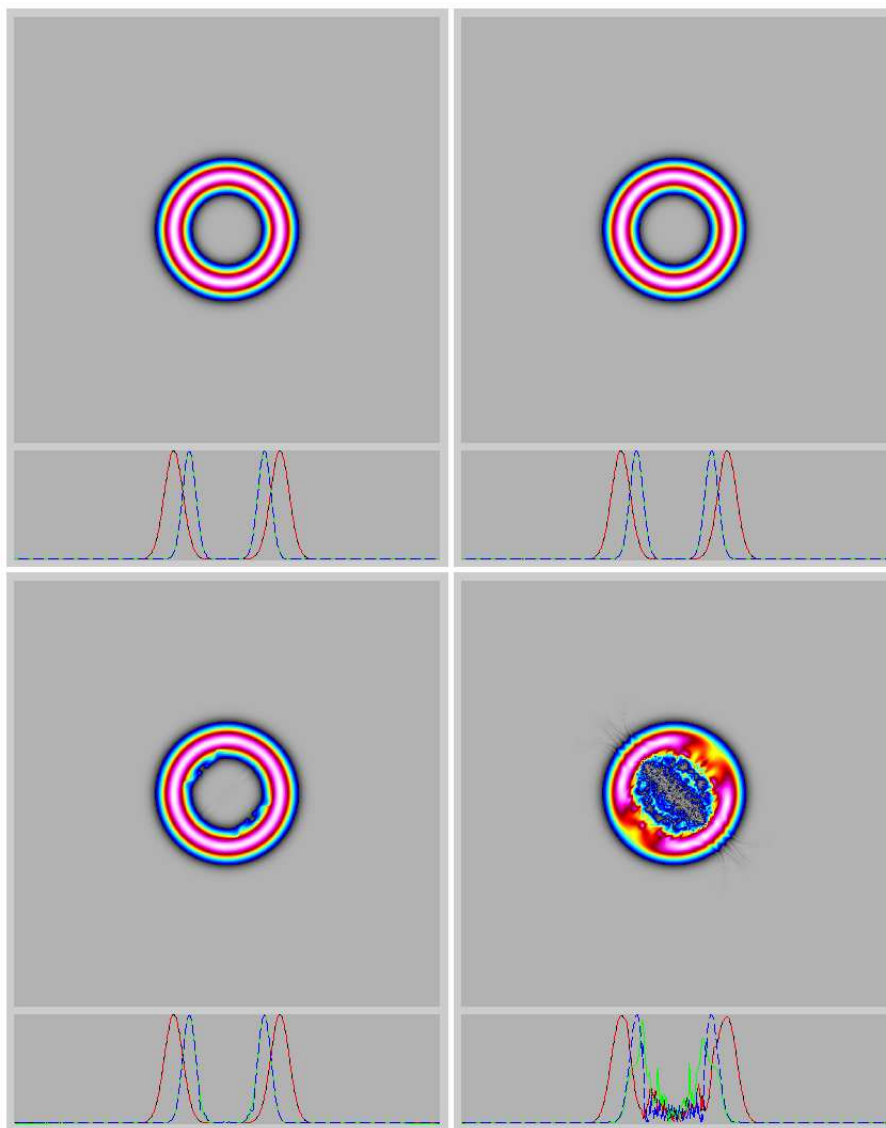


Figure 63: Reconstituted initial velocity profile after time reversal for the 2d "inout" case with $\alpha = \sigma$ (upper left), $\alpha = \sigma/2$ (upper right), $\alpha = \sigma/4$ (lower left), $\alpha = \sigma/8$ (lower right).

9.10 Time reversal

Table 1 summarizes how well the initial velocity profiles reconstitute upon reversing the EPDiff evolution from the final states. Numbers in each table entry are the L^1 norm, L^2 norm, and max norm of the difference between the initial velocity profile and its reconstituted (time reversed) value. The time reversed values are typically accurate to within one percent or less except in cases where head-on collisions occur. See text for further discussion.

10 Numerical results for EPDiff in 3d

Singular solutions of EPDiff in 3d. In this section, we extend our numerical solutions of EPDiff to 3d and discover that the codimension-one singular solution behavior of EPDiff persists. Namely, the singular solution behavior of EPDiff extends from curves in 2d to surfaces in 3d. To our knowledge, this is the first example of numerical simulations of the nonlinear interactions of contact discontinuities for fluid velocity in 3d. Of course, the singular surface solutions of EPDiff in 3d have no interpretation in the theory of internal waves. However, codimension-one singular solutions of EPDiff in 3d may have applications elsewhere, for example in the physics of liquid crystals in the inertial regime, as discussed for 1d evolution by Hunter and Saxton [30]. The 3d evolution of contact surfaces may also be regarded as “growth” from the viewpoint of imaging science, or evolution of shapes in 3d. The present work focuses on the role of convergence and momentum exchange in the evolution of contact surfaces.

Upcoming sections describe 3d simulations of evolution under EPDiff for each of twelve initial velocity distributions. For each simulation we have figures for $\alpha = \sigma$ and $\alpha = \sigma/2$. Due to memory and computational limitations, our 3d simulations were run at one-fourth the resolution of our 2d simulations (256^3 instead of 1024^2), and this lower resolution precluded us from performing accurate computations at the smaller values $\alpha = \sigma/4$ and $\alpha = \sigma/8$ that were simulated in 2d.

Each figure contains six frames, showing the initial magnitude (speed) of velocity, $|\mathbf{u}|$, in the upper left frame, followed by plots of $|\mathbf{u}|$ at future times, reading across and then down. For each simulation, the domain is $[-1, 1] \times [-1, 1] \times [-1, 1]$, and x is toward the right, y toward the back, and z toward the top. Individual plots contain colored, partially transparent level

Table 1: L^1 , L^2 , and max norm of the difference between the initial velocity profile and its reconstituted (time reversed) value for each 2d simulation.

Simulation	$\alpha = \sigma$	$\alpha = \sigma/2$	$\alpha = \sigma/4$	$\alpha = \sigma/8$
plate	3.62e-05	7.03e-05	0.000213	0.000577
	0.000142	0.000199	0.000624	0.00207
	0.00296	0.00279	0.00371	0.0147
parallel	7.86e-05	8.69e-05	0.00024	0.000844
	0.000204	0.000217	0.000616	0.00236
	0.00301	0.00283	0.00358	0.0161
skew	0.00134	0.000498	0.000719	0.00711
	0.0029	0.00111	0.00139	0.0177
	0.0199	0.0102	0.00727	0.148
wedge	0.000532	0.00061	0.00451	0.0567
	0.000705	0.00108	0.0123	0.111
	0.00395	0.00539	0.148	0.671
head-on	0.000179	0.00636	0.0274	0.0538
	0.000332	0.0165	0.0622	0.111
	0.00335	0.172	0.43	0.665
star	0.000207	0.00023	0.000604	0.00152
	0.000419	0.000442	0.000851	0.00237
	0.00531	0.00476	0.00515	0.00883
rotate	7.21e-05	2.54e-05	4.81e-05	0.000293
	8.17e-05	3.95e-05	8.23e-05	0.00059
	0.000301	0.000139	0.000339	0.0027
right	0.00021	0.000292	0.000583	0.0029
	0.000372	0.000615	0.00137	0.00696
	0.00545	0.00422	0.0106	0.0892
inout	0.000219	0.000245	0.0024	0.0348
	0.00048	0.000431	0.0103	0.087
	0.00621	0.00183	0.137	0.594

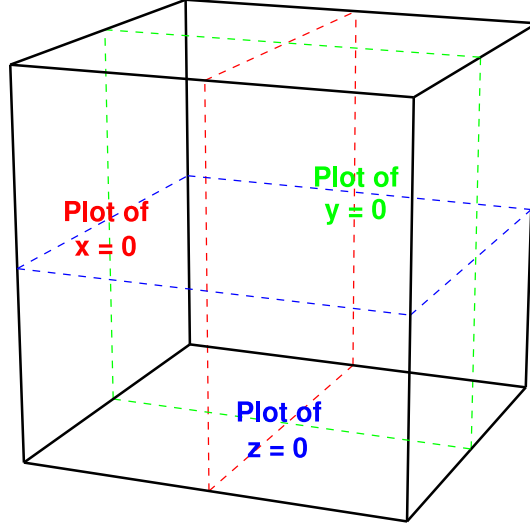


Figure 64: Locations of 2d slices of $|\mathbf{u}|$ shown in the left, back, and bottom panels in the upcoming 3d figures.

surfaces of $|\mathbf{u}|$ at 35% (purple), 25% (red), 15% (green), and 5% (blue) of its maximum value over all frames in the figure. The number of level surfaces, and the colors, amount of transparency, and fractions of $|\mathbf{u}|$ represented by each level surface, where chosen after considerable experimentation so that they reveal maximal information with minimal clutter.

The left, back, and bottom panels of each frame show color contour plots of 2d slices through the three dimensional data at $x = 0$, $y = 0$, and $z = 0$, respectively, as sketched in Figure 64. The same color scheme that was used for the 2d simulations, as described in Section 9 and illustrated in Figure 17, is used here for the 2d slices of the 3d simulations. Note that the colors used for the 2d slices do not correspond to the colors used for the 2d level surfaces. For example, red in the 2d slices does not represent the same value of $|\mathbf{u}|$ as the red level surface.

10.1 Plate

The analog of a segment in 2d is a disc, or plate, in 3d. Figures 65 and 66 show the evolutions at various values of α in 3d from a confined initial velocity distribution in the shape of a plate in speed and moving rightward

(in the positive x direction). The initial plate distribution is chosen so it falls off exponentially in the normal x direction and it falls off at the edges (or rim) of the plate as a Gaussian, as we did in 2d at the endpoints of the segments. Because the distribution moves with flow, it expands rightward and outward.

The bottom panels in Figures 65 and 66 show the propagation in a horizontal section (at the midplane) $x = 0$ of the cube of size 2. This is an invariant plane, by symmetry, for this initial value problem. The invariant midplane section essentially reproduces the 2d evolution of the peakon segments; note the similarity in patterns at late time on the bottom panel in 3d and the corresponding interactions in 2d.

The bottom panel in Figure 66 with $\alpha = \sigma/2$ shows the plate expanding and decomposing into several peakon contact surfaces. The left panel shows a vertical section at $x = 0$. The initial circular disc propagates rightward through this vertical section and maintains its circular symmetry as it expands. The back panel shows a vertical section at $y = 0$. By symmetry, the results on the vertical section shown on the back panel in this case are the same as those on the bottom panel ($z = 0$ horizontal section).

The disc shaped velocity distribution balloons out rightward and expands cylindrically into one peakon contact surface in Figure 65 for $\alpha = \sigma$, and into several peakon contact surfaces of width $\alpha = \sigma/2$ in Figure 66. Again, this is consistent with the similar evolution restricted to lower spatial dimensions.

10.2 Parallel

Figures 67 and 68 each show two plate-like velocity distributions of the same diameter, initialized moving rightward so that the one behind, with twice the speed, will overtake the one ahead. The discs are initially offset at 45 degrees in the y - z plane; so this evolution has no reflection symmetry about any of the midplanes.

Both plates balloon outward and decompose into peakon contact surfaces, and the overtaking collision shows two reconnections of the surfaces. One reconnection occurs at first contact and the other evolves late in the simulation, as seen on both the bottom and back panels. The left panel shows a transverse vertical section of the first reconnection. As the two discs propagate past the plane $x = 0$, their peakon contact surfaces develop into a perimeter that surrounds the interior interactions.

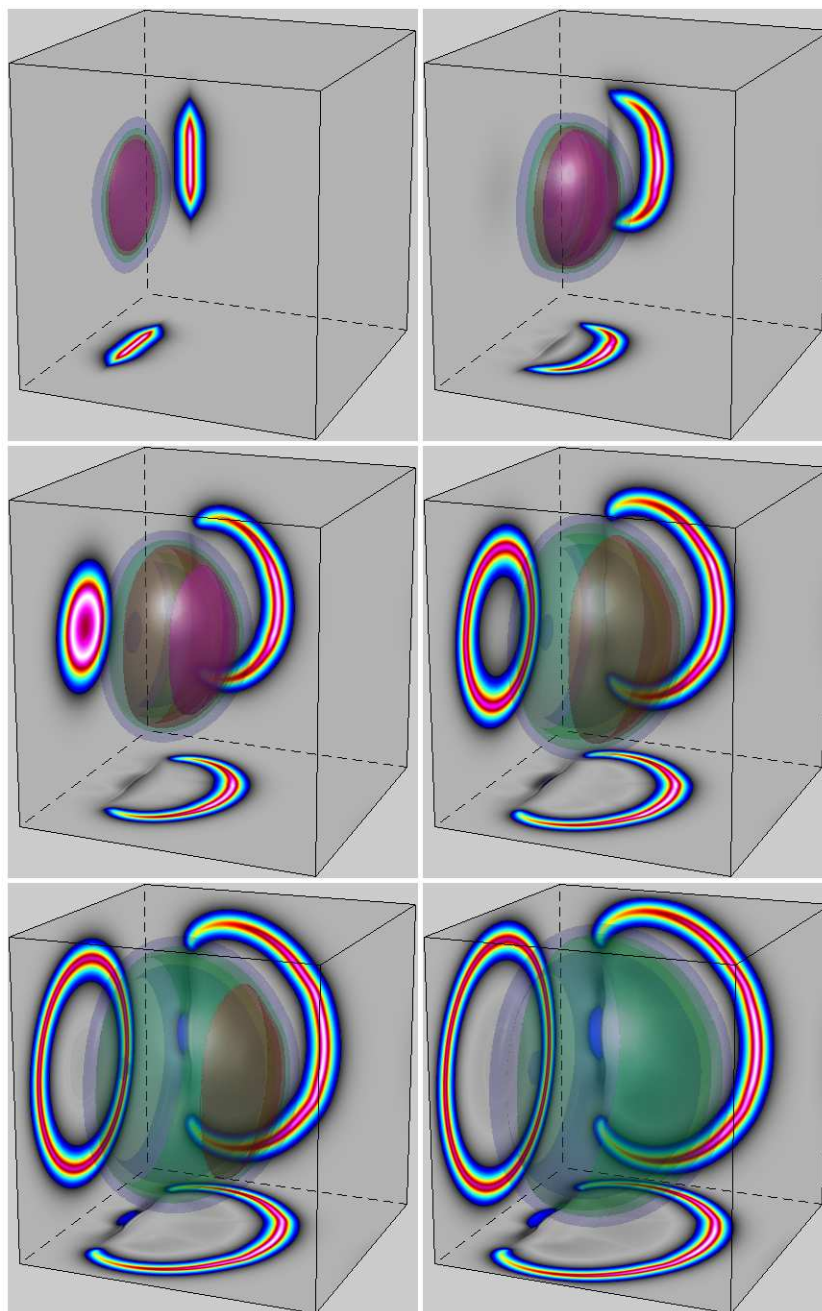


Figure 65: Evolution of the 3d “plate” initial velocity profile with $\alpha = \sigma$.

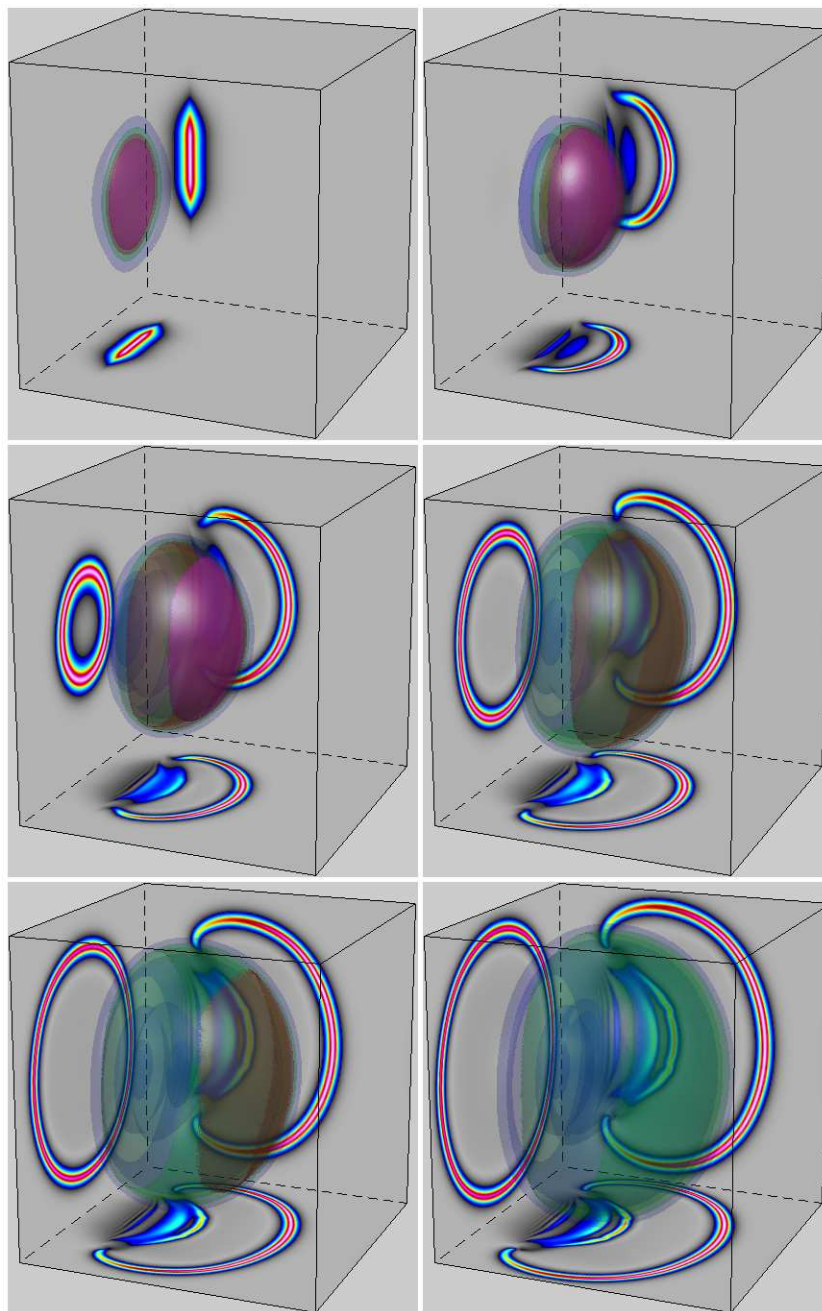


Figure 66: Evolution of the 3d “plate” initial velocity profile with $\alpha = \sigma/2$.

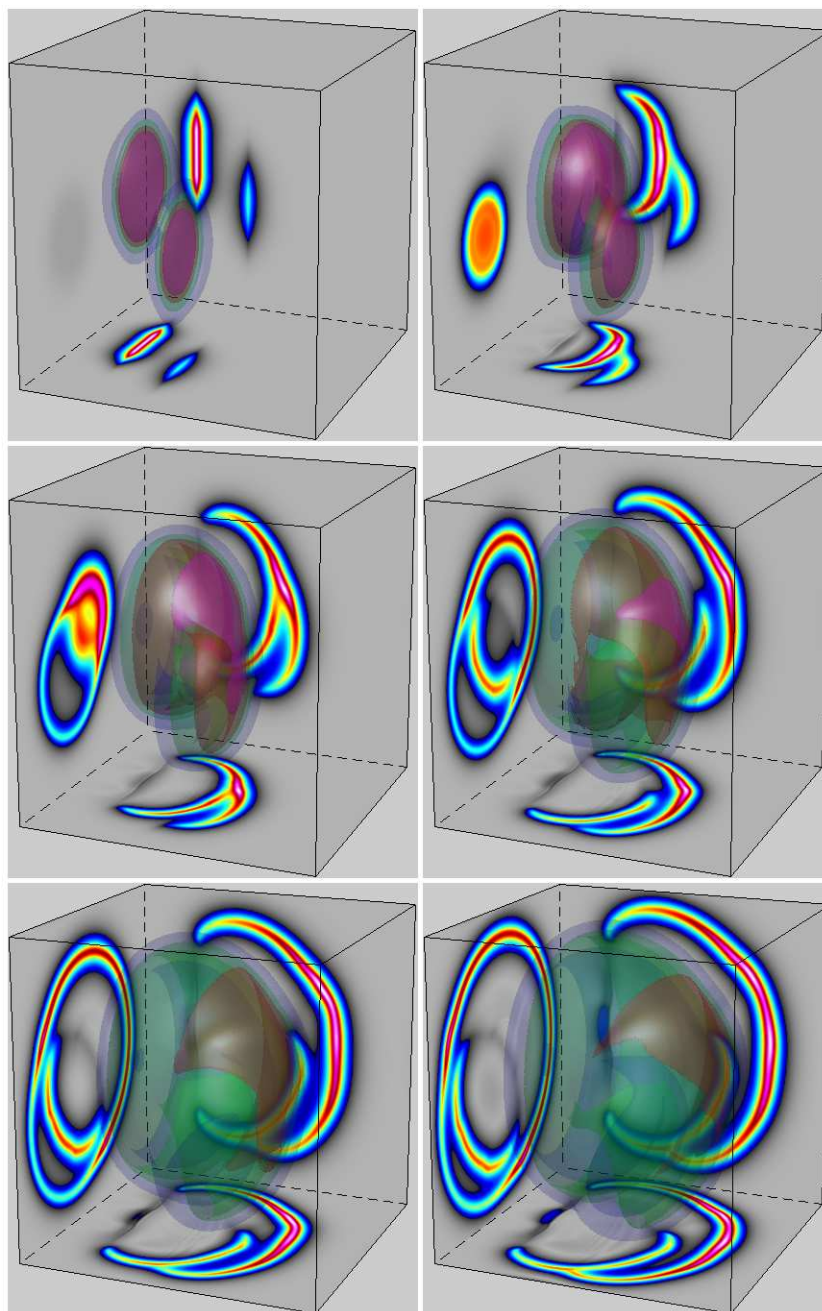


Figure 67: Evolution of the 3d “parallel” initial velocity profile with $\alpha = \sigma$.

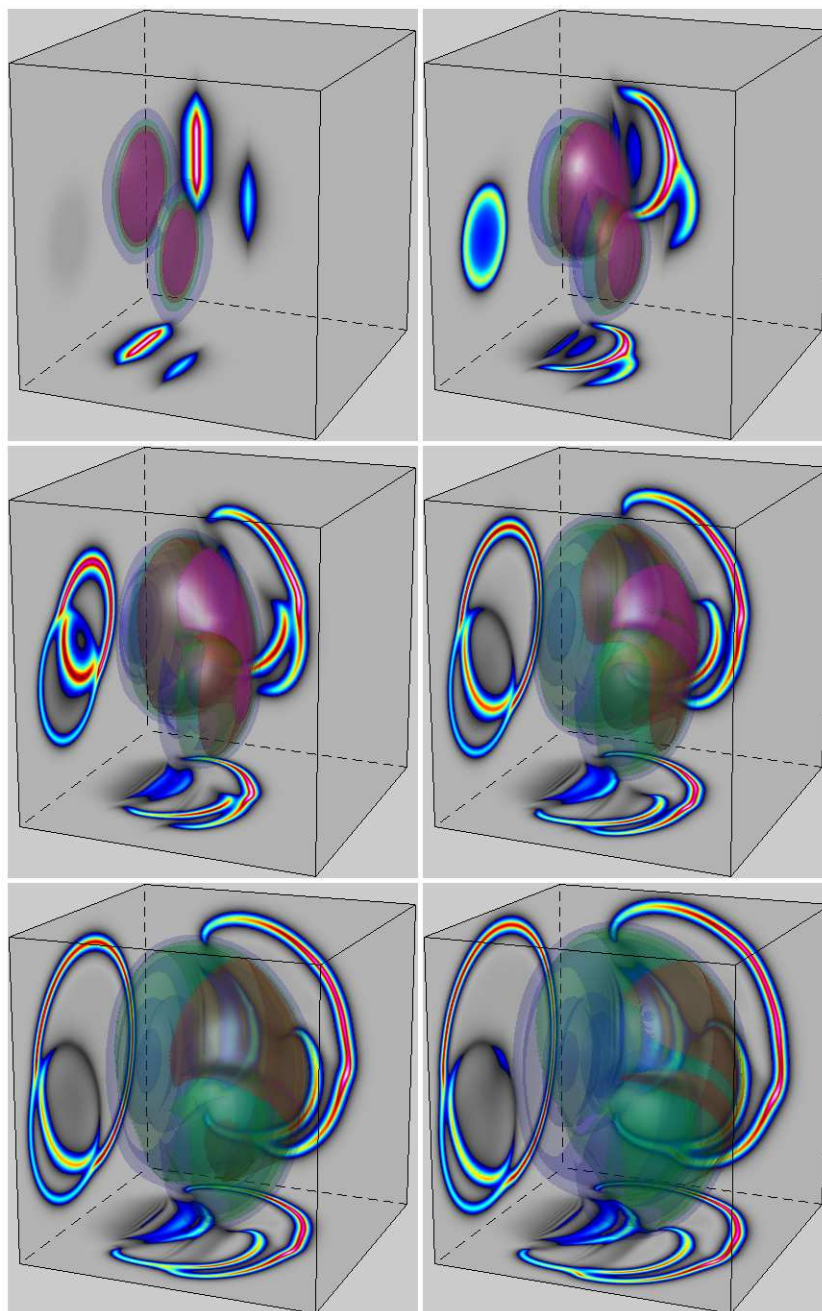


Figure 68: Evolution of the 3d “parallel” initial velocity profile with $\alpha = \sigma/2$.

10.3 Skew

The skew overtaking collision in Figures 69 and 70 show both the first and second reconnections as the two initial plate distributions collide and interact. Again, the sections shown on the bottom and back panels are very reminiscent of the corresponding skew collisions of peakon segments in 2d. The memory wisps that appear so clearly in the 2d skew overtaking collisions are less distinct here, likely because of the coarser resolution (256^3 , versus 1024^3 in 2d).

10.4 Wedge

In Figures 71 and 72, two plate distributions of velocity approach the $z = 0$ horizontal midplane from above and below, each at 45 degrees. Their “wedge” collision occurs at the horizontal midplane and has reflection symmetry about the xz vertical midplane, at $y = 0$.

The evolution shown on the back panels in these figures is similar to the 2d wedge collision of peakon segments. The bottom panel shows the creation of peakon contact surfaces which are reminiscent of the peakon contact segments in the 2d “right” figure. Namely, peakon contact surfaces emerge from the collision and reconnect to encircle the collision region. Each successive peakon contact surface (whose intersection with the horizontal midplane is shown as a curve in the bottom panel) reconnects at the rear and produces a wavefront that encircles the collision region. The wavefront motion is less intense in the rear because it is moving slower at the rear than in the front. We see one major collision at the midplane followed by an emission of rightward moving peakon contact surfaces and their later reconnections in the rear. At later times, the hot spots show pronounced trailing memory wisps.

10.5 Head-on

Figures 73 and 74 show the head-on collision of two identical plate-like distributions offset by the same distance at 45 degrees when projected into the yz plane. Hence, the evolution in the sections shown in the back and bottom panels are identical, and all three panels have reflection and rotation symmetries.

The back and bottom panels of Figures 73 and 74 have symmetry under reflection about one diagonal and rotation by π about the other. Likewise,

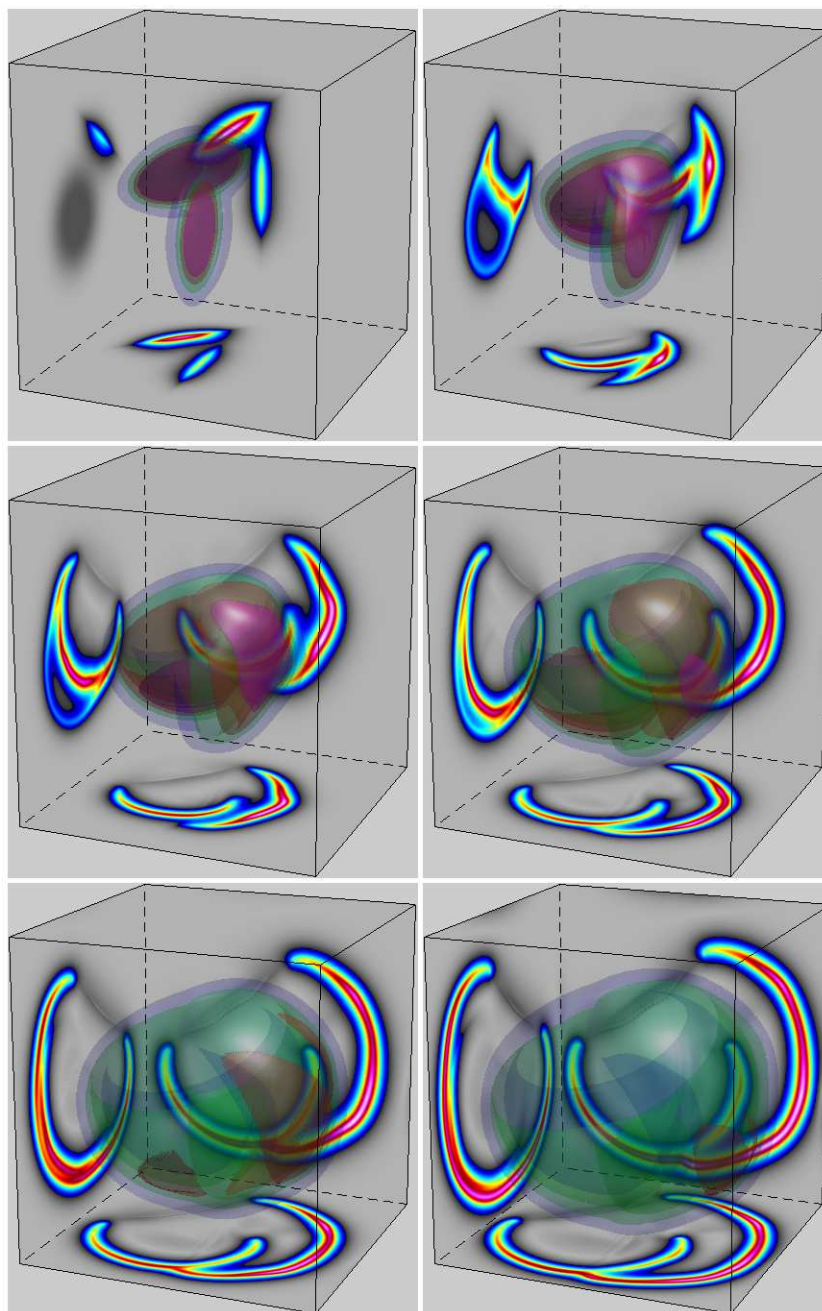


Figure 69: Evolution of the 3d “skew” initial velocity profile with $\alpha = \sigma$.

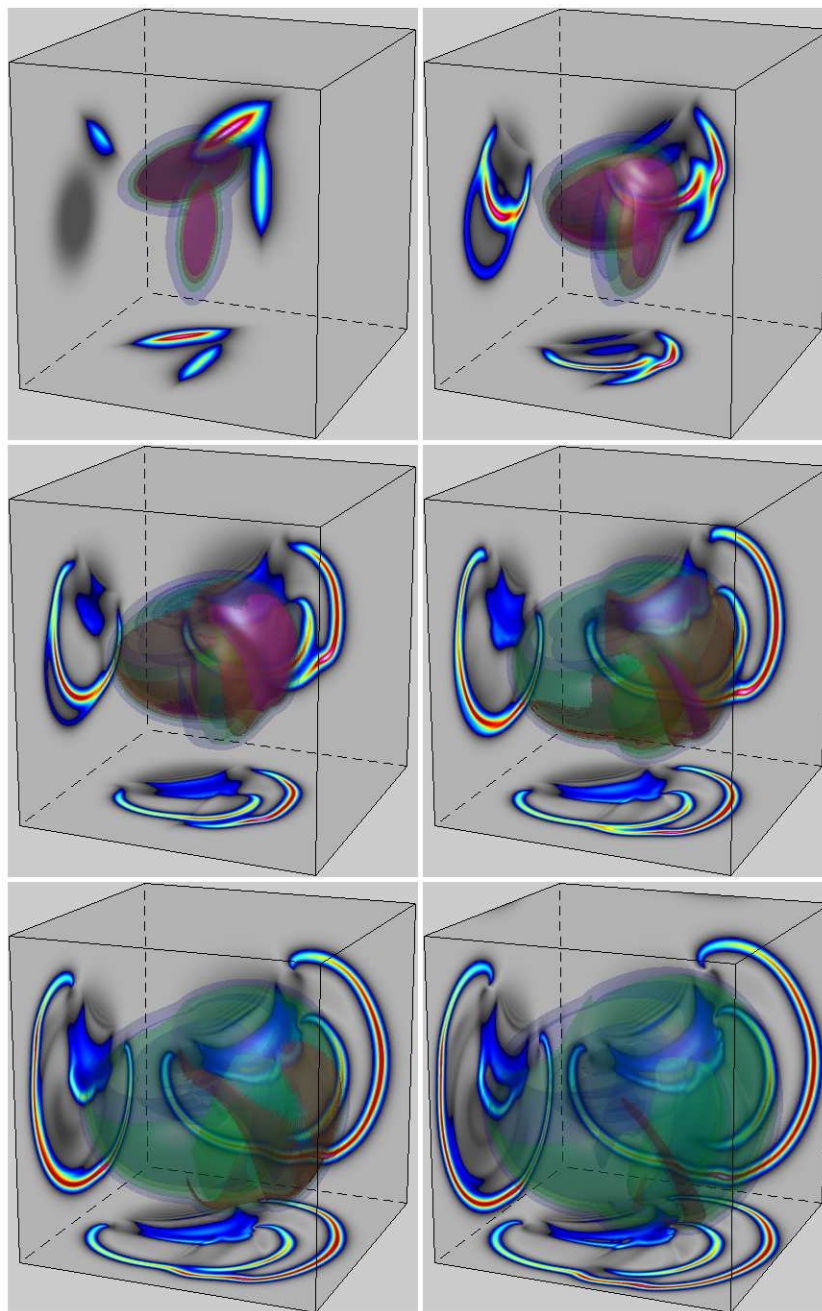


Figure 70: Evolution of the 3d “skew” initial velocity profile with $\alpha = \sigma/2$.

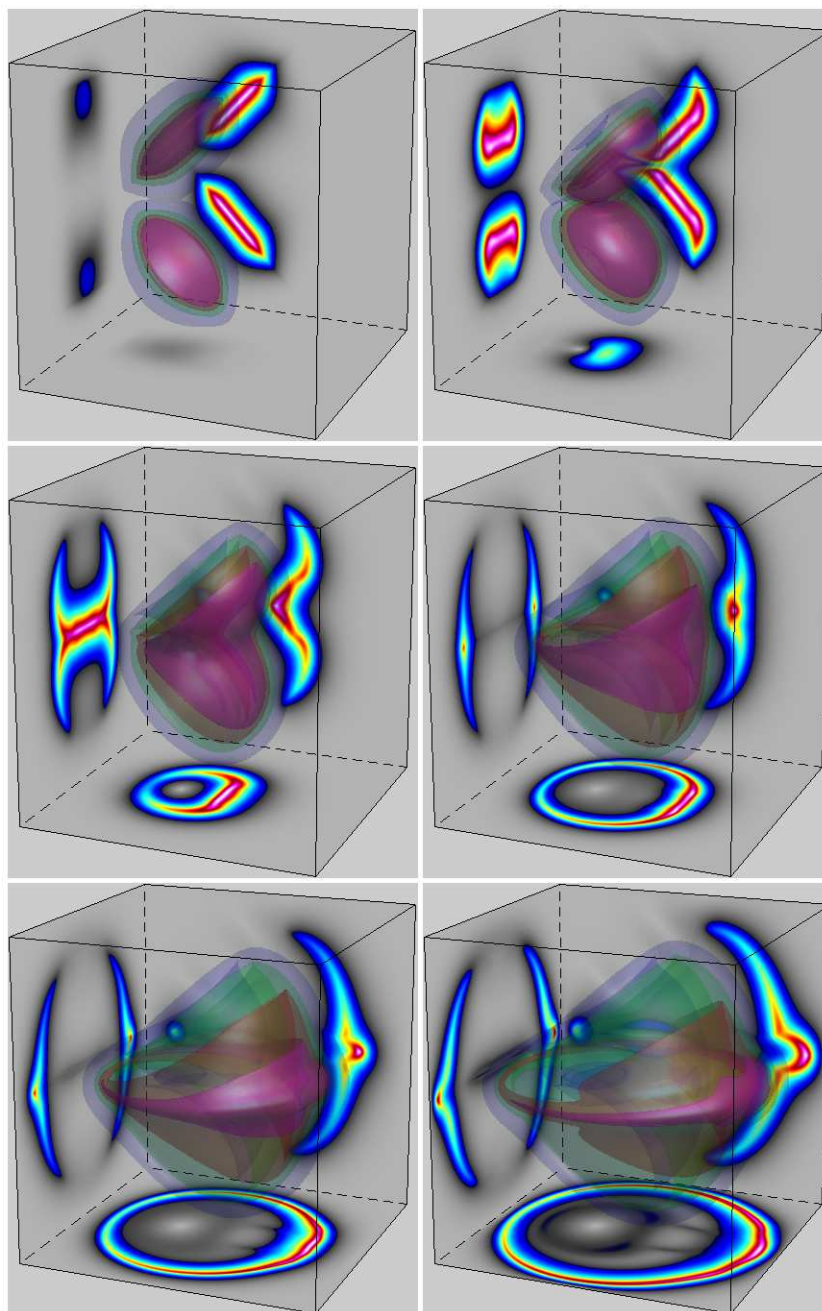


Figure 71: Evolution of the 3d “wedge” initial velocity profile with $\alpha = \sigma$.

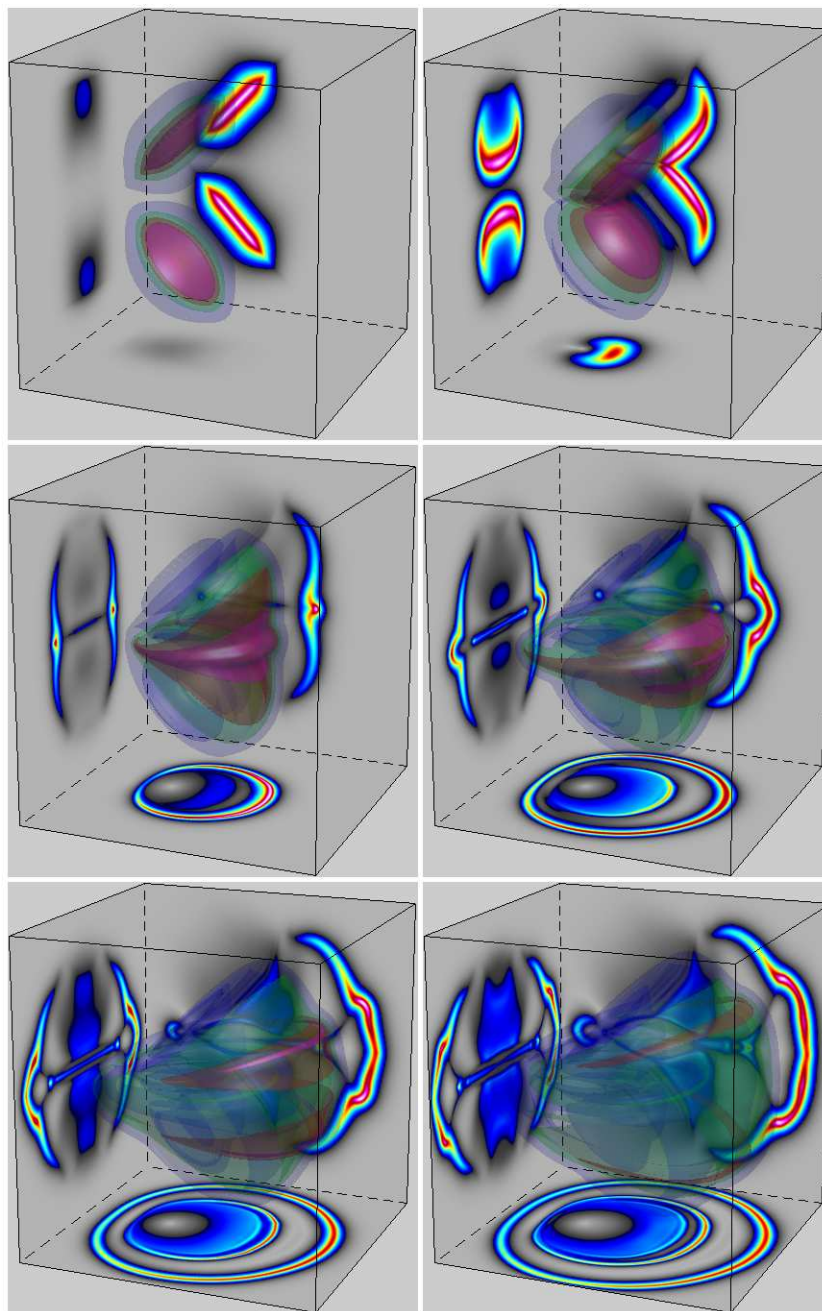


Figure 72: Evolution of the 3d “wedge” initial velocity profile with $\alpha = \sigma/2$.

the left panels are reflection symmetric about both diagonals. These symmetries help diagnose the complex evolution occurring as the two peakon contact segments balloon outward toward each other and collide head-on. As expected from earlier animations, the segments annihilate and re-emerge, leaving behind a complex residual flow where the head-on collision occurred.

The left panels of Figures 73 and 74 show that the reconnection after the collision occurs results in a peakon contact segment surrounding the central region.

10.6 Rotate

For the simulations shown in Figures 75 and 76, an initially spherical Gaussian shell is rigidly rotating about its vertical axis, like a planet. This angular motion couples to radial motion with cylindrical symmetry about the axis of rotation. The evolution remains cylindrically symmetric about this axis and shows convergence to it, as seen in the bottom panels of Figures 75 and 76. The left and back panels show identical emergence of peakon contact segments. This evolution shows the coupling between the angular and radial motion in the cylindrically symmetric case. The outward velocities expand essentially like an oblate sphere, and may become less oblate with time. The midplane $z = 0$ shown on the bottom panel is an invariant section, because of up-down symmetry, and it shows the cylindrical convergence and expansion driven by the initial angular rotation.

10.7 Right

In Figures 77 and 78, a Gaussian shell in speed is initially moving rightward. The peakon contact surfaces emerging on its outer right side are diverging, while those emerging on its inner left side are converging. The acceleration due to this convergence leads to an overtaking collision that imparts rightward momentum to the diverging peakon contact segments. By cylindrical symmetry about the x axis, the bottom and back panels show the same motion. The left panels show how this cylindrically symmetric motion moves through the vertical midplane at $x = 0$. The midplane $z = 0$ is invariant and the motion in this plane mimics the motion observed in the corresponding 2d problem.

This shared behavior is one of the main conclusions of this paper: 3d numerical results have planar slices which show the corresponding 2d mo-

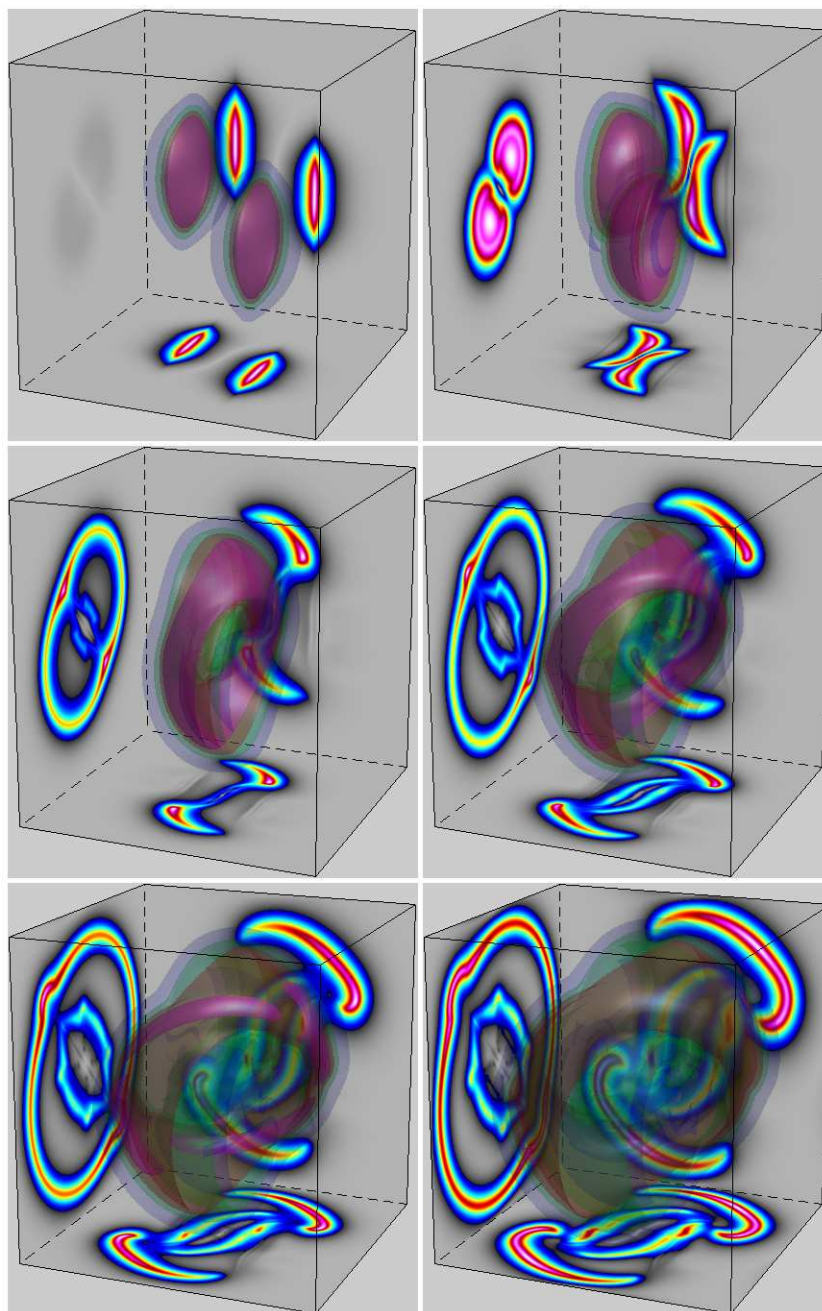


Figure 73: Evolution of the 3d “head-on” initial velocity profile with $\alpha = \sigma$.

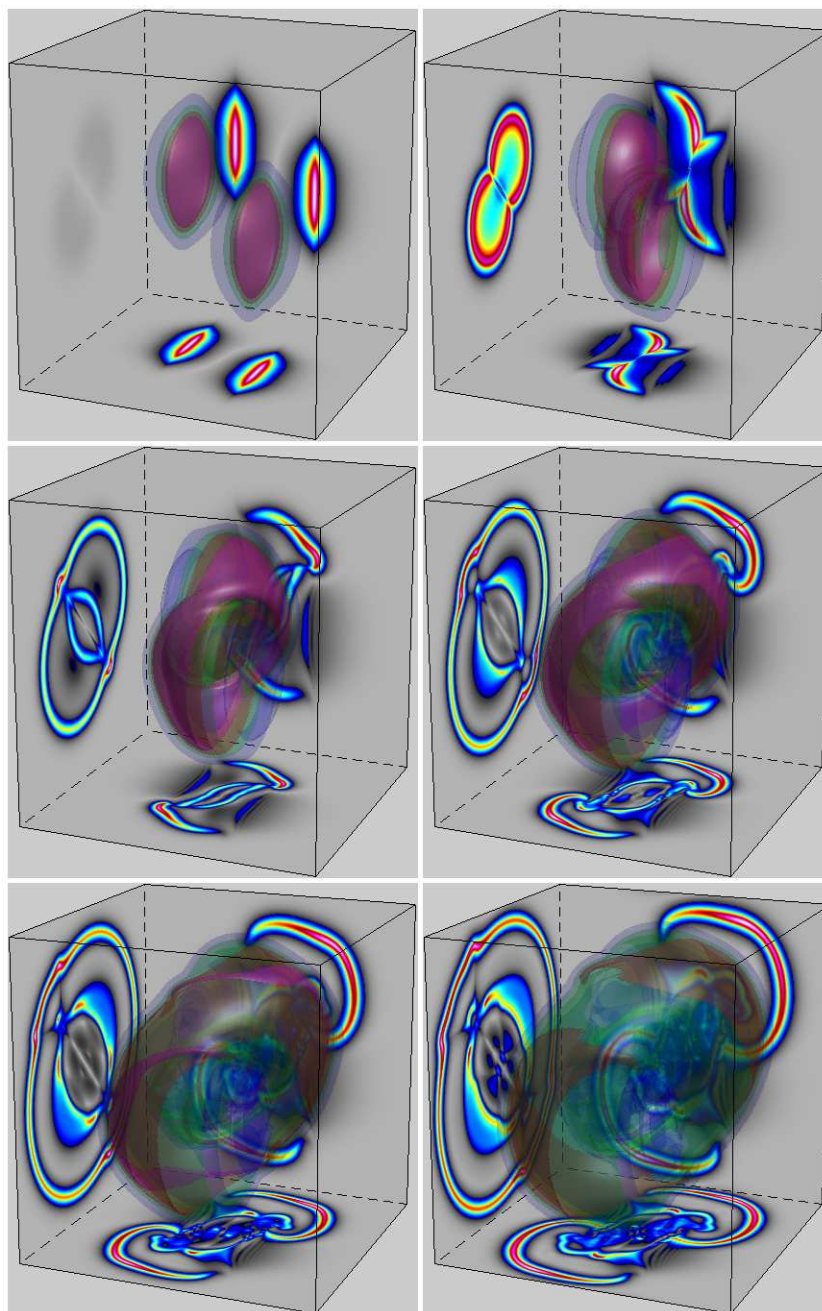


Figure 74: Evolution of the 3d “head-on” initial velocity profile with $\alpha = \sigma/2$.

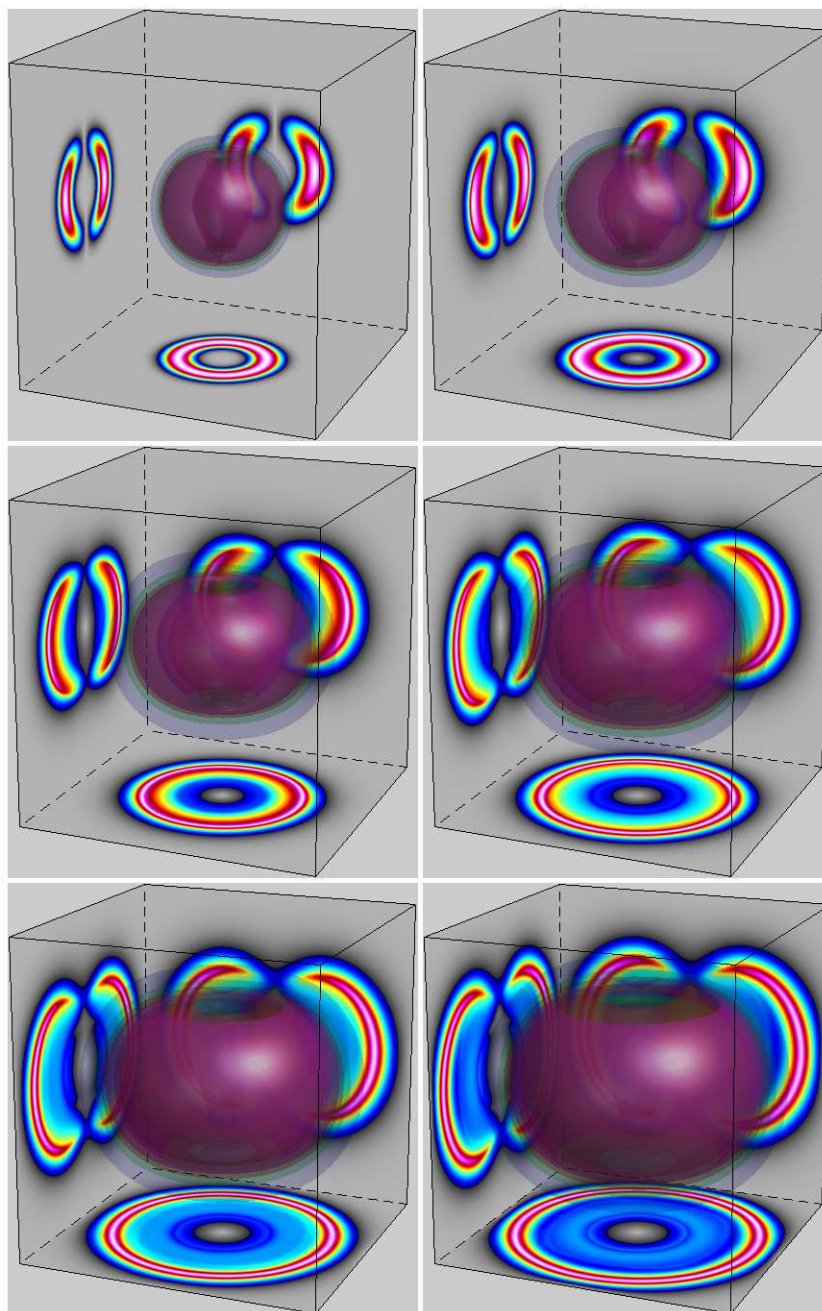


Figure 75: Evolution of the 3d “rotate” initial velocity profile with $\alpha = \sigma$.

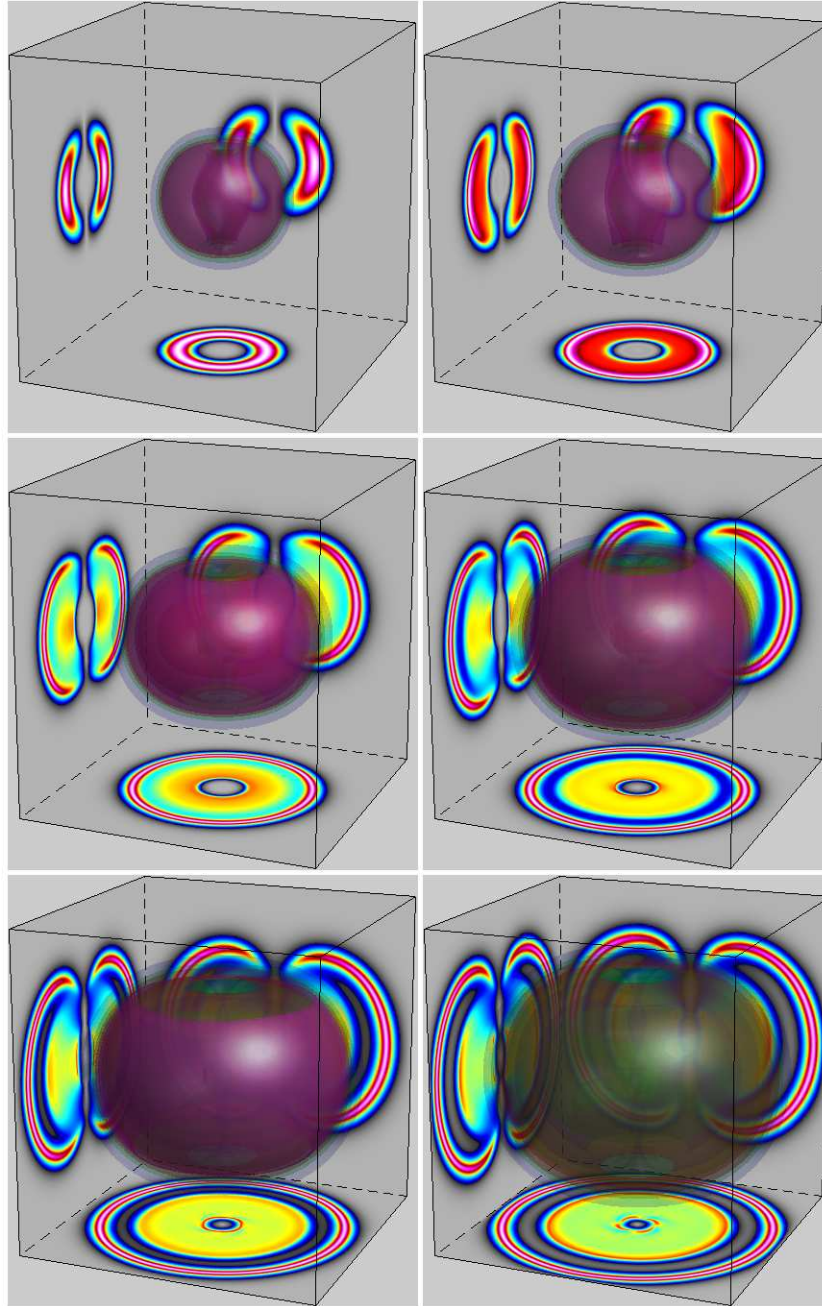


Figure 76: Evolution of the 3d “rotate” initial velocity profile with $\alpha = \sigma/2$.

momentum transfer behavior, and 2d numerical results have linear slices which show the corresponding 1d momentum transfer behavior. This reduction principle allows the complex interactions of contact wave surfaces to be analyzed as elastic collisions showing local momentum transfer. This is a feature of the collective behavior of singular solutions, because such solutions possess no internal degrees of freedom.

10.8 Inout

In Figures 79 and 80, a 3d Gaussian shell of speed is initially given the 2d “inout” velocity distribution, $-(\sin \theta, \cos \theta) \exp(-(r - r_0)^2/\sigma^2)$, on each horizontal plane, weighted by the cosine of the polar angle, as in the rigid rotation simulation. Consequently, the bottom panel shows the same “inout” 2d motion as before, now at one-fourth the resolution and only for $\alpha = \sigma/2$ and $\alpha = \sigma$. The left and back panels show identical motion, consisting of head-on collisions in the center and a wedge-like collision at the top and bottom. The bottom panel for $\alpha = \sigma/2$ seems to agree better with the corresponding 2d case, than for $\alpha = \sigma$, which has less of a collision that in the 2d case.

10.9 Wheel

In Figures 81 and 82, the speed is initially distributed as a Gaussian within a toroidal annulus rotating rigidly about its axis of rotational symmetry, oriented along the x axis. This “wheel” initial distribution has reflection symmetry about its axis of rotational symmetry, oriented along the midplane $x = 0$. The motion on this invariant symmetry plane $x = 0$ shows circularly symmetric collapse and radial expansion, seen in the left panel. (Some distortion is seen upon reflection from the x axis of cylindrical symmetry, again due to mesh effects.)

The identical back and bottom panels show a head-on collision occurring on the horizontal midplane, followed by re-emergence in 3d for $\alpha = \sigma/2$ and the development of a pair of strong hot spots (actually a funnel shape in 3d) followed by emergence of a perimeter of peakon contact segments surrounding the interior region.

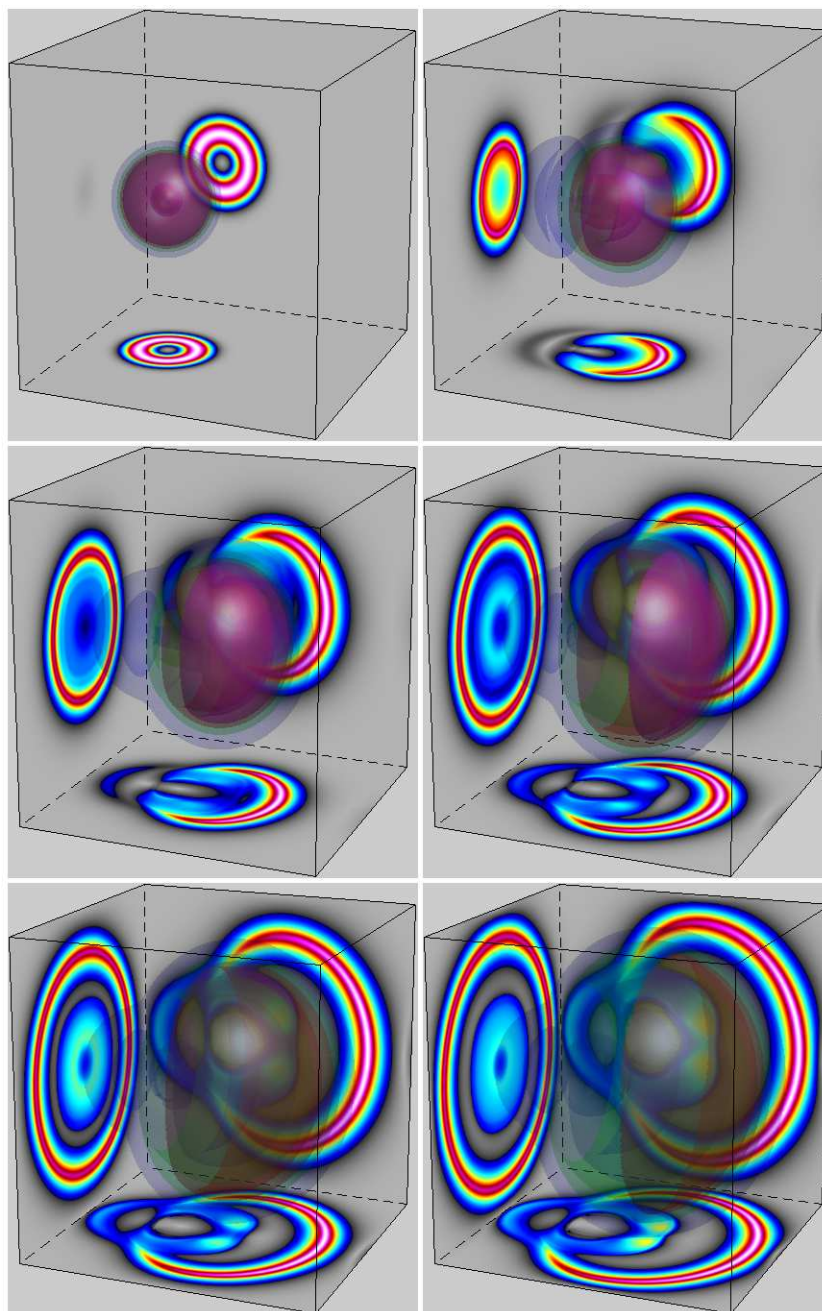


Figure 77: Evolution of the 3d “right” initial velocity profile with $\alpha = \sigma$.

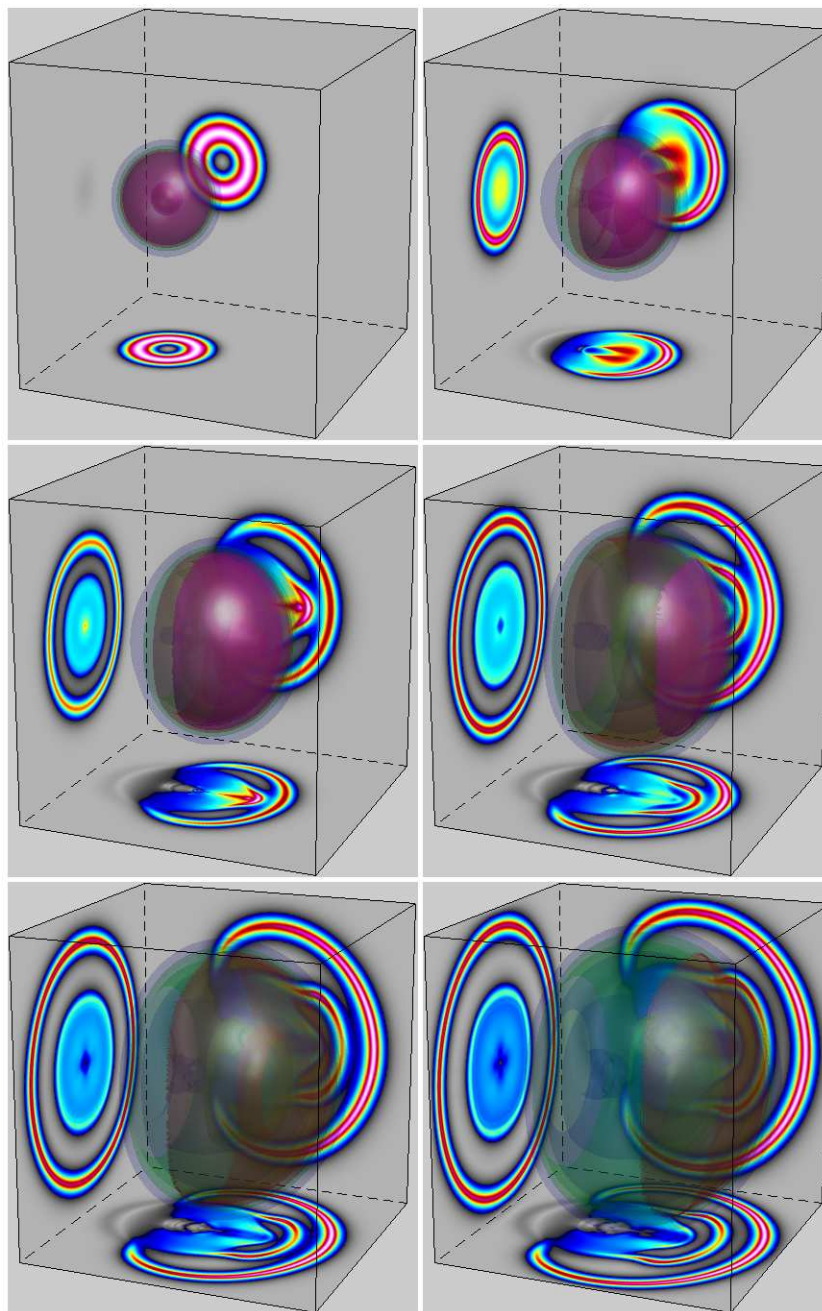


Figure 78: Evolution of the 3d “right” initial velocity profile with $\alpha = \sigma/2$.

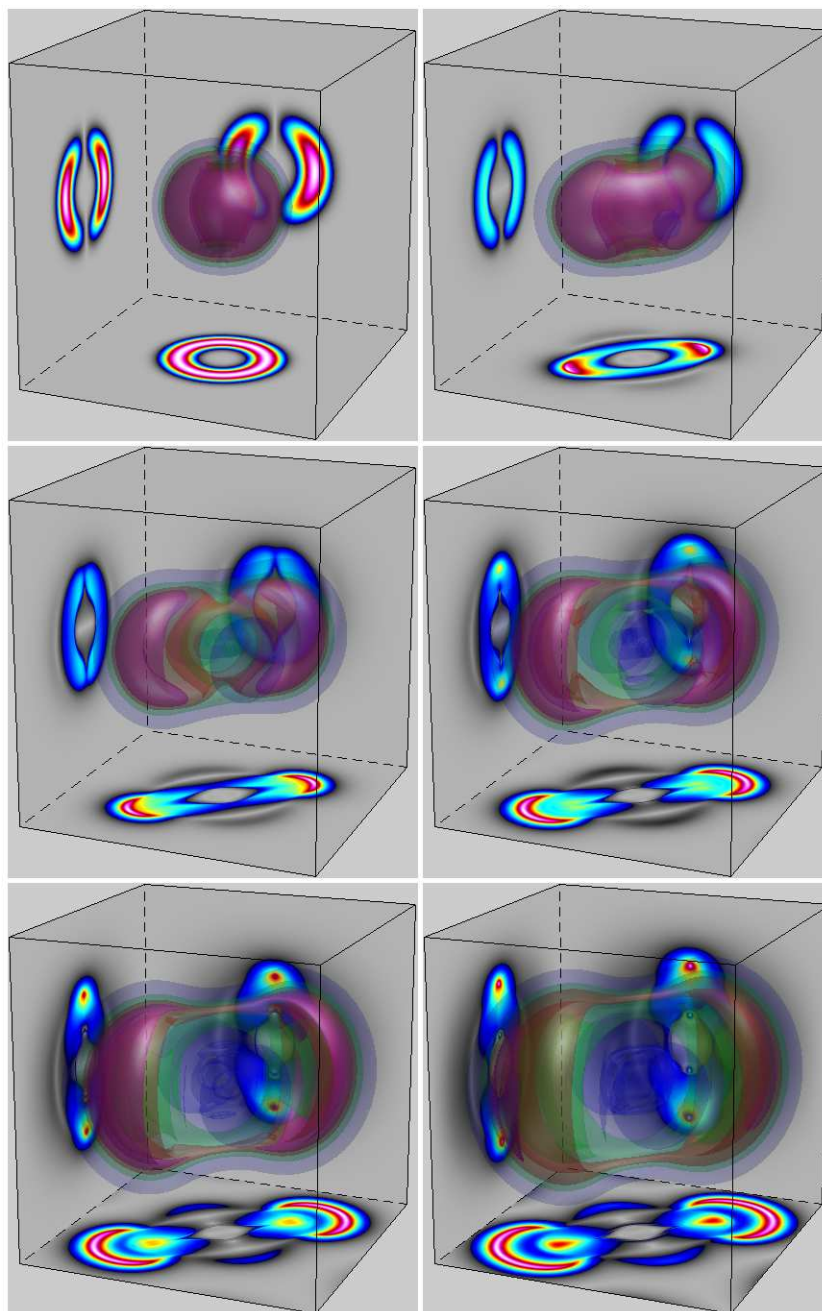


Figure 79: Evolution of the 3d “inout” initial velocity profile with $\alpha = \sigma$.

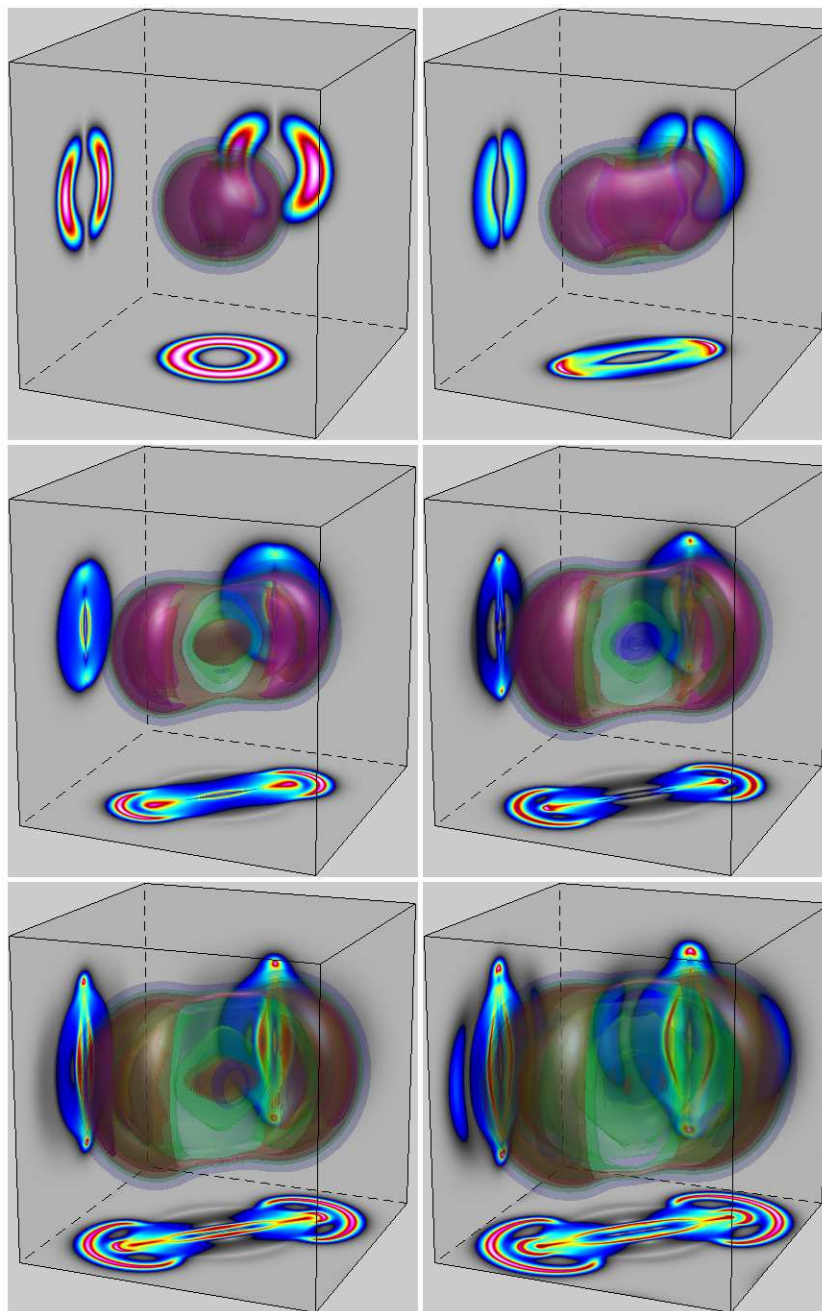


Figure 80: Evolution of the 3d “inout” initial velocity profile with $\alpha = \sigma/2$.

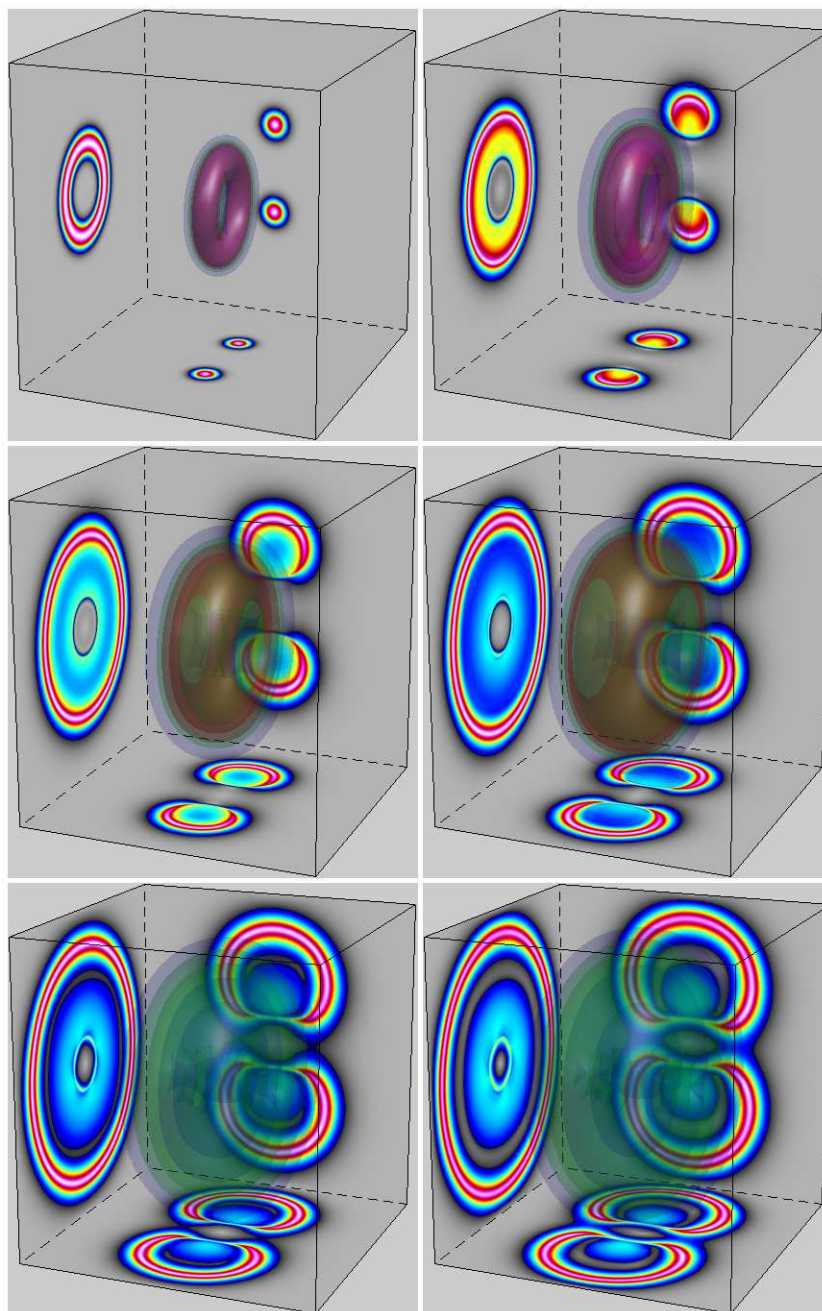


Figure 81: Evolution of the 3d “wheel” initial velocity profile with $\alpha = \sigma$.

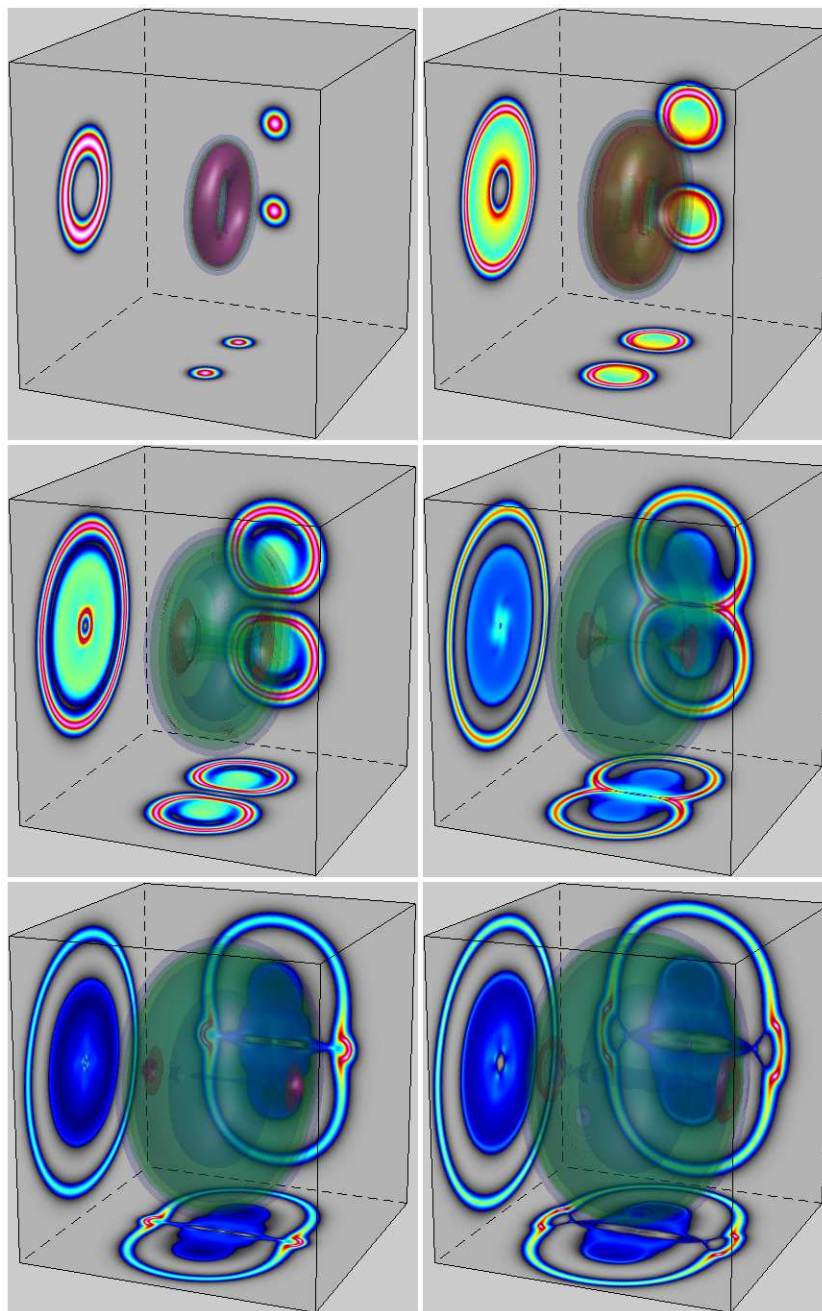


Figure 82: Evolution of the 3d “wheel” initial velocity profile with $\alpha = \sigma/2$.

10.10 Wheels

Figures 83 and 84 show simulations of the interactions of two coaxial tori (wheels) of velocity, both rotating about the x axis, but offset from each other in the x direction. The cylindrically symmetric evolution from this initial state shows axial convergence, radial expansion and reconnection of peakon contact surfaces, via a series of head-on collisions. The exchange of momentum in these interactions is especially dramatic. Eventually, an outward-expanding peakon contact surface emerges and surrounds the entire interaction region.

10.11 Torus

In Figures 85 and 86, a torus-shaped Gaussian velocity distribution (wheel) is initially moving uniformly rightward in the direction of its symmetry axis. Cylindrically symmetric rightward moving fronts form, then expand, collide, and reconnect at the axis of symmetry. This is a “cylindrically symmetric wedge” collision that funnels into the axis, then forms jets that accelerate in both forward and backward directions along the x axis.

The three dimensional images of peakon contact surfaces are particularly vivid in the animations to which Figures 85 and 86 belong. Because of the cylindrical symmetry, the back and bottom panels show the same motion in different perspectives. The left panel also shows the collapse to the axis of symmetry. Because of the curvature of the peakon contact surfaces, this cylindrical collision imparts axial momentum both forward and backward, which is especially clear in the case $\alpha = \sigma/2$.

10.12 Tori

In Figures 87 and 88, two linked tori of speed are started along their axes of rotational symmetry in orthogonal directions, one rightward and one upward. They undergo a series of wedge-like collisions leading to many reconnections. They also undergo overlapping collisions that impart momentum, but do not reconnect the peakon contact segments. Eventually, a single outward moving peakon contact segment will surround the interaction region.

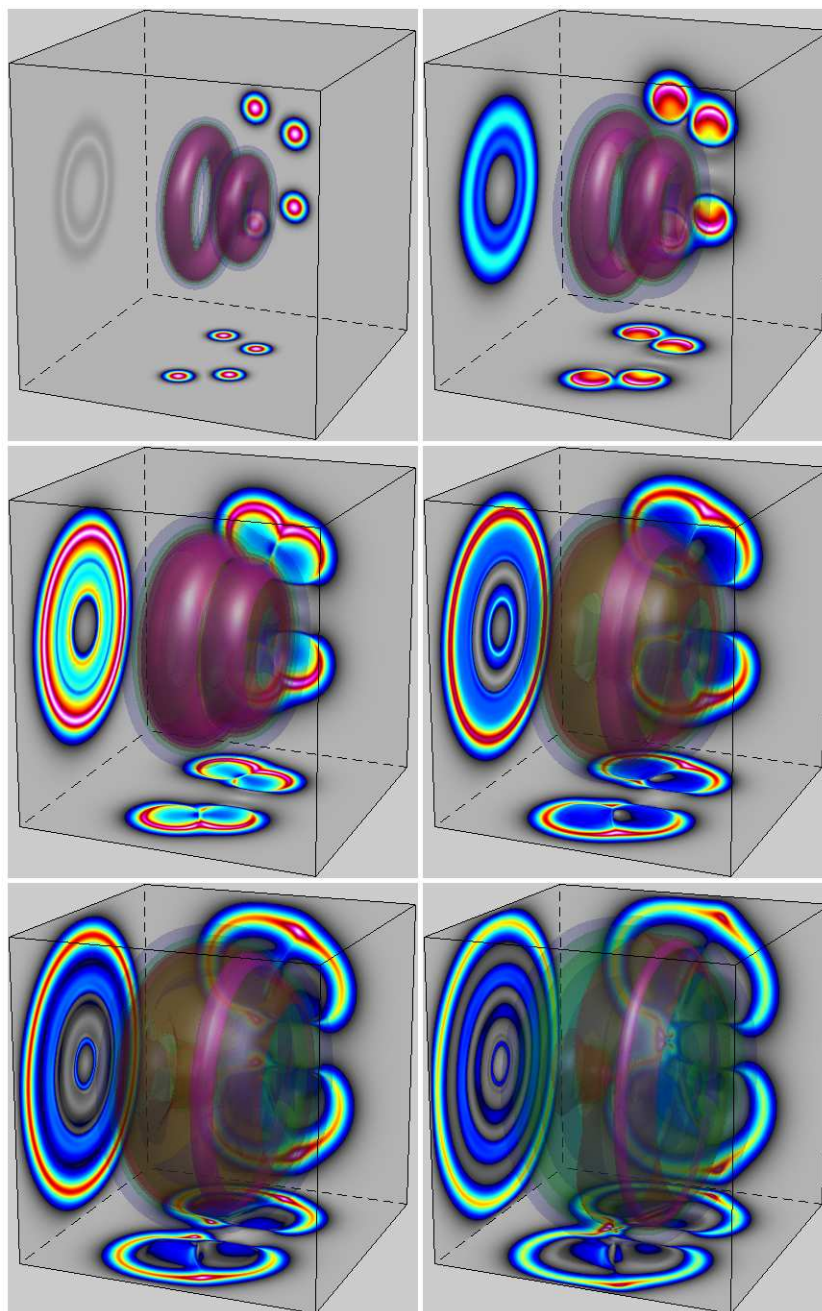


Figure 83: Evolution of the 3d “wheels” initial velocity profile with $\alpha = \sigma$.

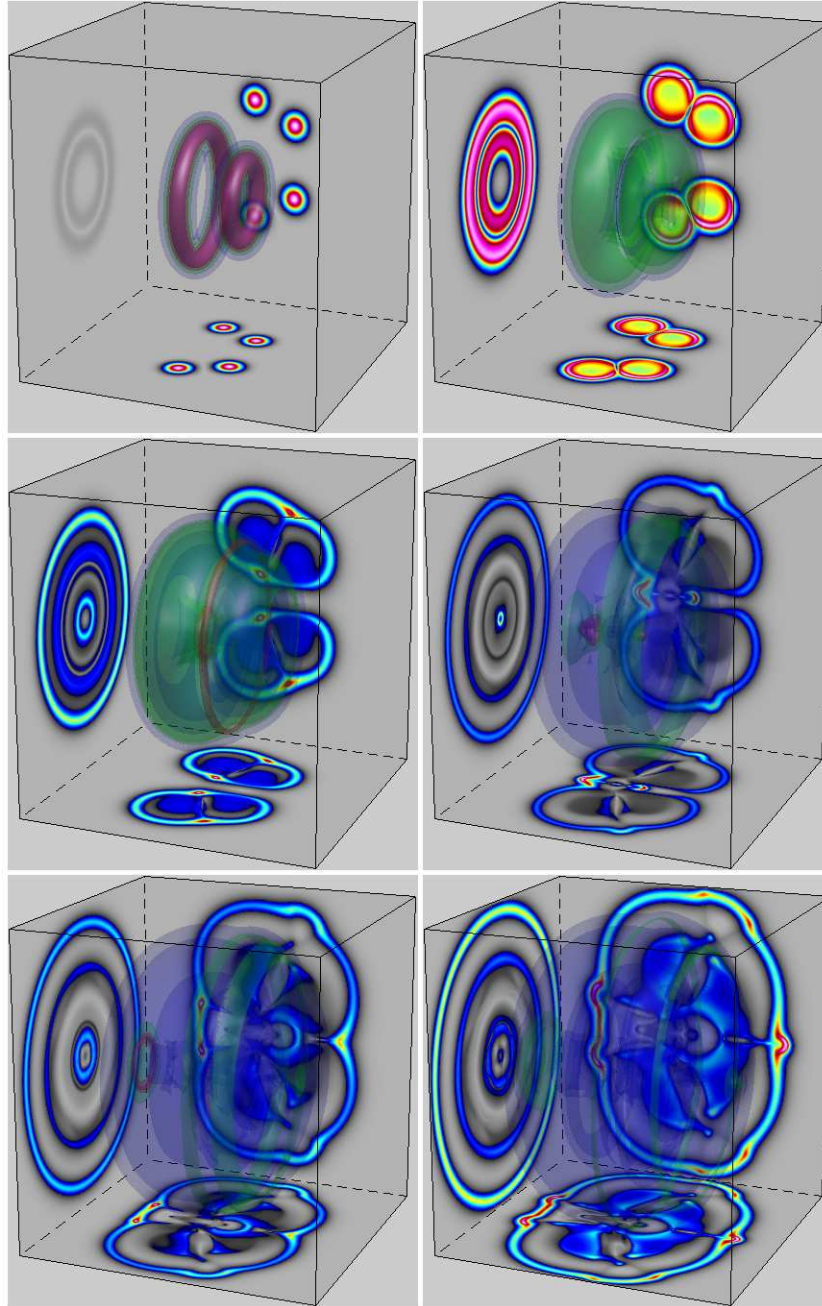


Figure 84: Evolution of the 3d “wheels” initial velocity profile with $\alpha = \sigma/2$.

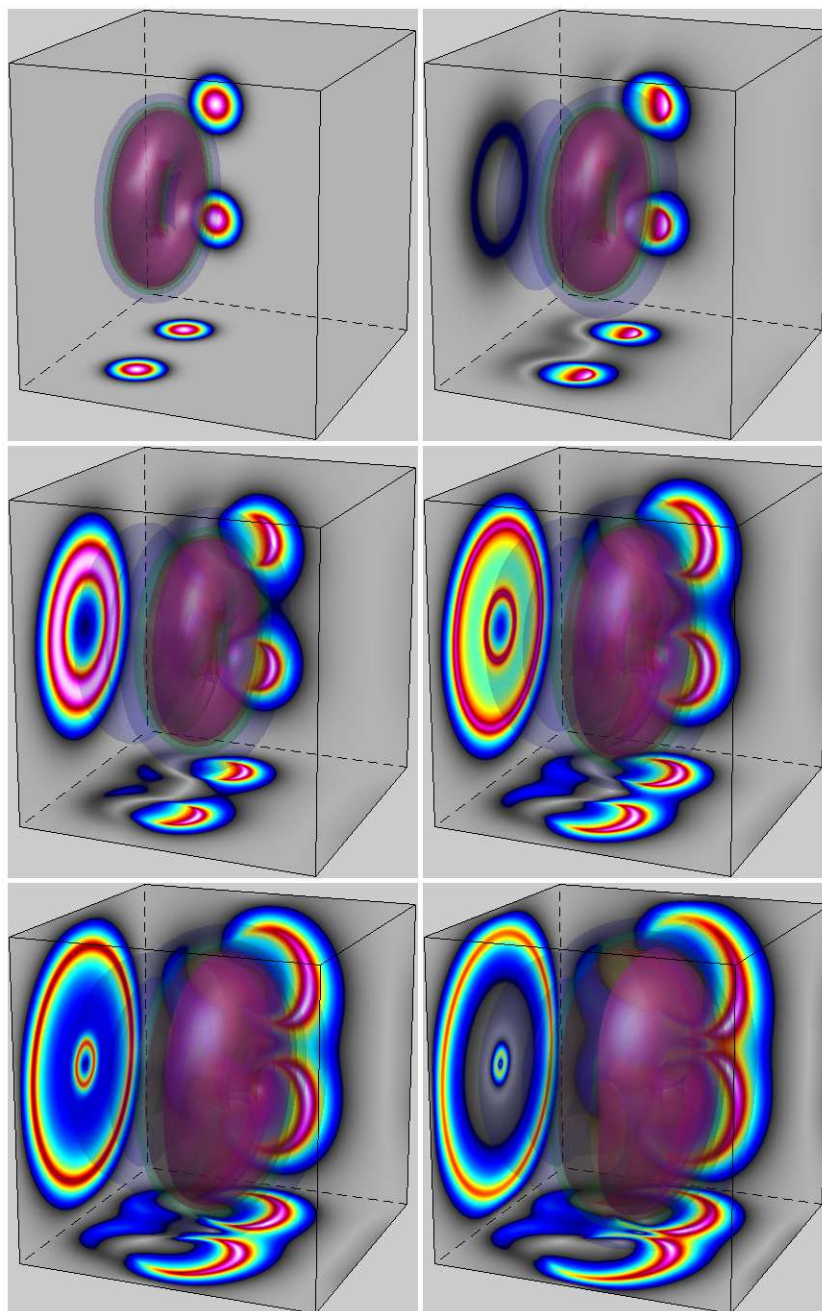


Figure 85: Evolution of the 3d “torus” initial velocity profile with $\alpha = \sigma$.

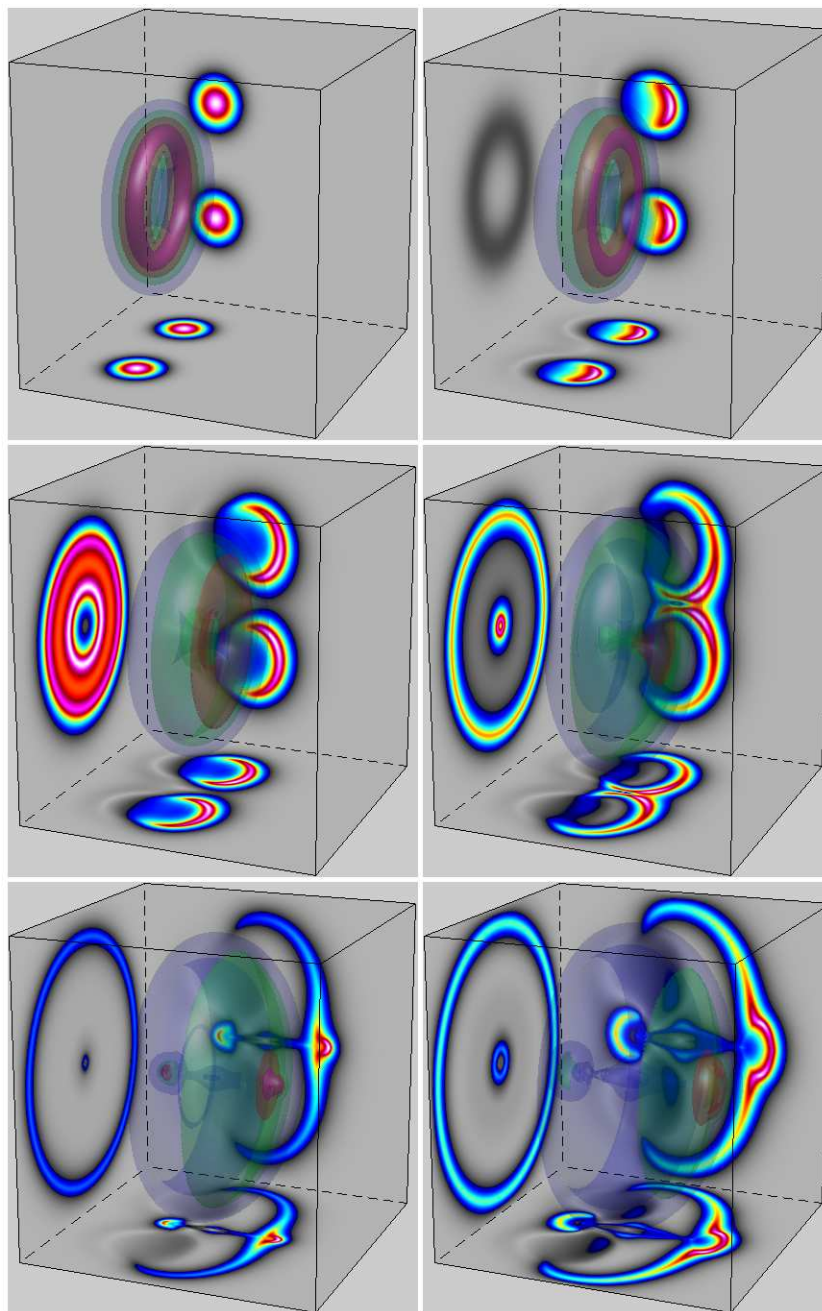


Figure 86: Evolution of the 3d “torus” initial velocity profile with $\alpha = \sigma/2$.

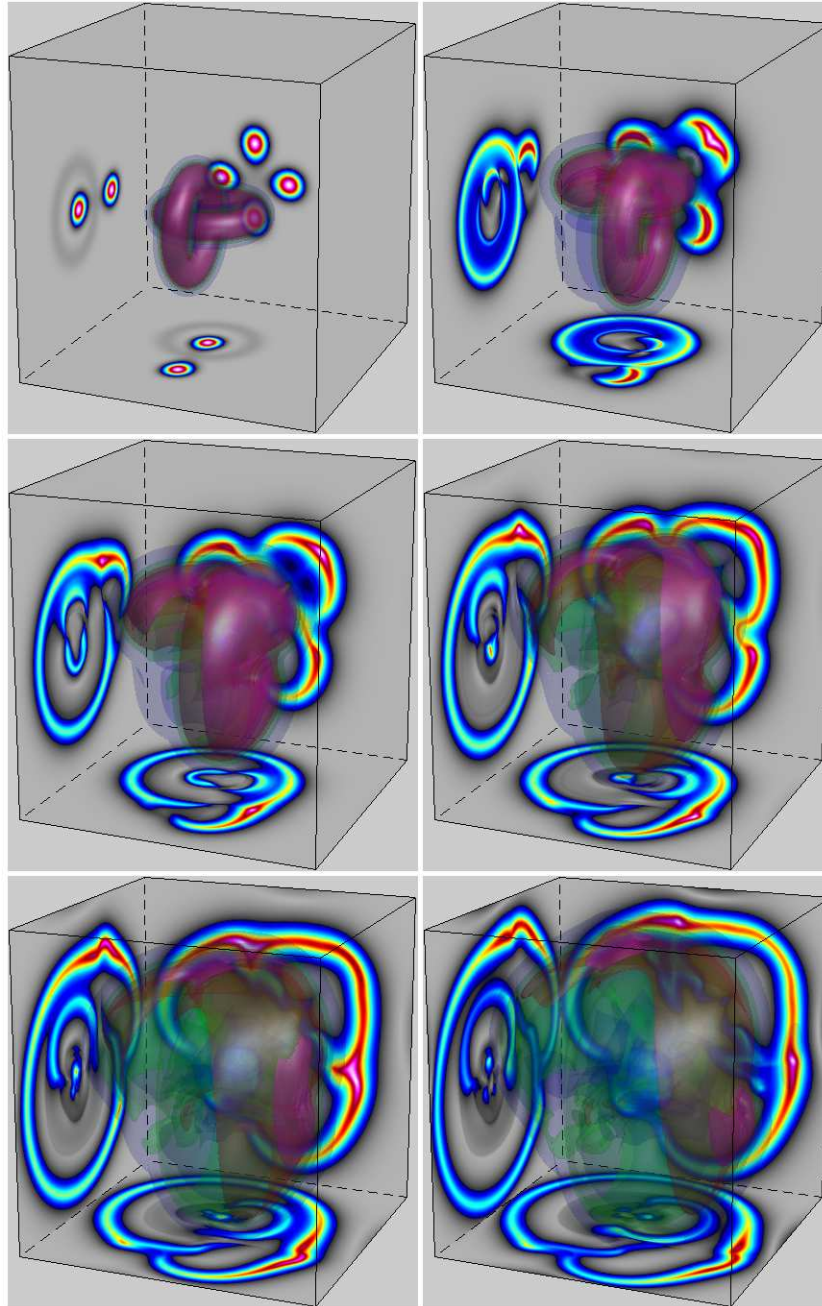


Figure 87: Evolution of the 3d “tori” initial velocity profile with $\alpha = \sigma$.

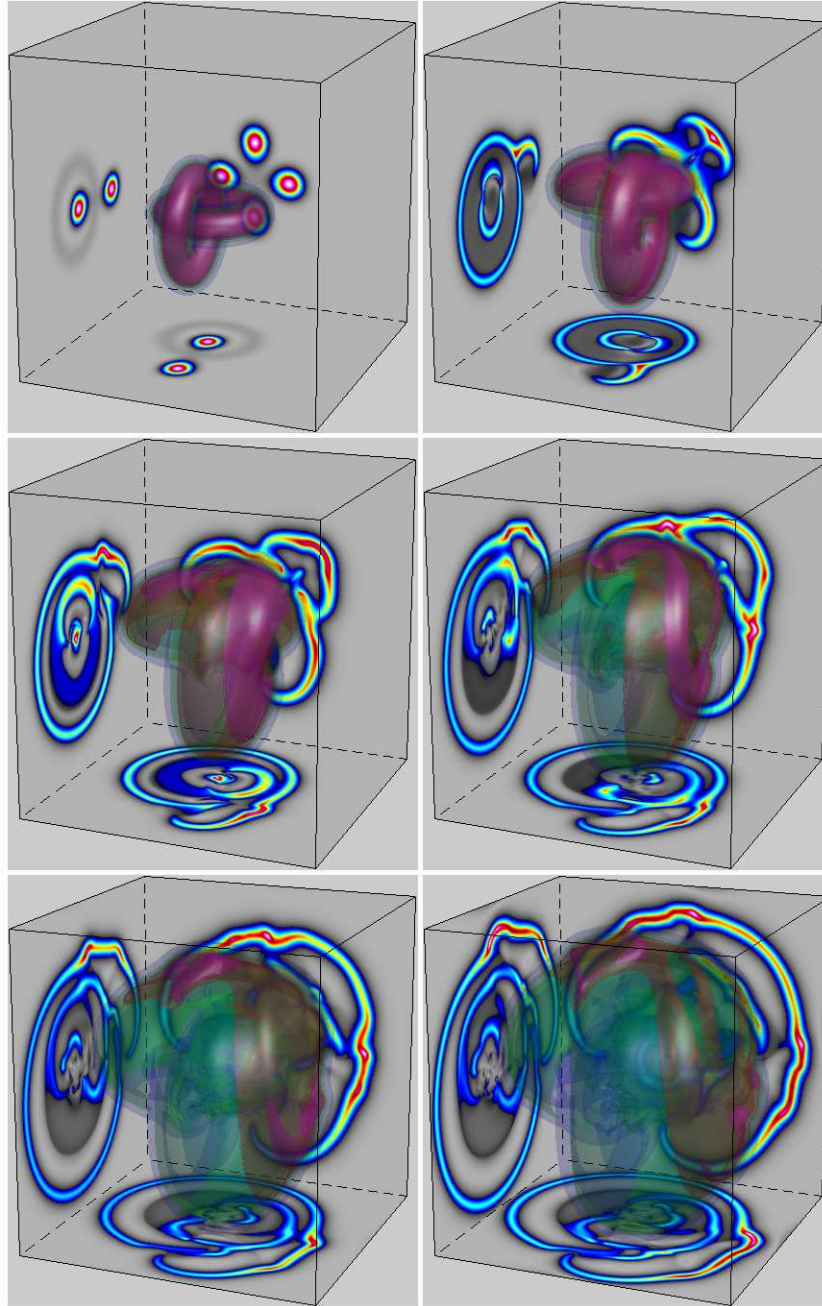


Figure 88: Evolution of the 3d “tori” initial velocity profile with $\alpha = \sigma/2$.

10.13 Time reversal

Table 1 summarizes how well the initial velocity profiles reconstitute upon reversing the EPDiff evolution from the final states. Numbers in each table entry are the L^1 norm, L^2 norm, and max norm of the difference between the initial velocity profile and its reconstituted (time reversed) value. We do not show contour plots of the time reversed runs in 3d because they are all visually indistinguishable at the larger values of α chosen for our 3d simulations. The time reversed values are typically accurate to within one percent or less.

11 Conclusions, future directions, and outstanding problems

By a sequence of approximations applied to the Euler-Poincaré variational principle for the multilayer columnar motion (MLCM) of an incompressible fluid, we derived a hierarchy of EP equations. Several new MLCM equations belong to this hierarchy, as well as the standard Boussinesq equations for shallow water waves, which are recovered upon specialization to weak nonlinearity.

The EPDiff equation (1) was derived in the limiting case of a single layer undergoing strongly nonlinear motion in the absence of linear dispersion. In 1d, the EPDiff equation restricts to the dispersionless case of the CH equation for nonlinear shallow water waves. The dispersionless CH equation possesses singular soliton solutions whose velocity possesses a sharp peak (jump in slope) moving at a speed equal to its height. The corresponding momentum for a train of such peakons is a set of delta functions at the locations of the peaks in velocity. Thus, this momentum density is distributed as points on the line which evolve under the action (by Ad^*) of the diffeomorphisms (smooth invertible maps).

A geometrical version of the soliton paradigm. The local description of the Ad^* action of the smooth invertible maps is the EPDiff ad^* equation (1), which holds in *any* number of dimensions. Hence, EPDiff allows comparison of the behavior of its singular solutions in 1d, 2d and 3d. Numerically, the singular solutions of EPDiff of codimension one (points on the line, curves on the plane, surfaces in a volume) are found to be stable. Moreover, they

Table 2: L^1 , L^2 , and max norm of the difference between the initial velocity profile and its reconstituted (time reversed) value for each 3d simulation.

Simulation	$\alpha = \sigma$	$\alpha = \sigma/2$
plate	0.000105	9.26e-05
	0.000595	0.000553
	0.0109	0.01
parallel	0.000165	0.000146
	0.000686	0.00064
	0.0109	0.01
skew	9.81e-05	8.68e-05
	0.000435	0.000411
	0.00793	0.00753
wedge	0.00029	0.000135
	0.000513	0.000398
	0.00545	0.00522
head-on	0.000193	0.000178
	0.000772	0.000738
	0.00885	0.00829
rotate	9.36e-05	6.13e-05
	0.000151	0.000102
	0.000625	0.000433
right	6.08e-05	4.01e-05
	0.000128	8.88e-05
	0.00131	0.00103
inout	9.4e-05	6.19e-05
	0.000151	0.000103
	0.00063	0.000436
wheel	5.87e-05	3.98e-05
	0.000176	0.000124
	0.0019	0.00138
wheels	0.000123	8.51e-05
	0.000259	0.000184
	0.00193	0.0014
torus	7.92e-05	5.45e-05
	0.000109	7.87e-05
	0.000523	0.000391
tori	0.00011	7.48e-05
	0.000248	0.000173
	0.0019	0.00137

are found to dominate the initial value problem, essentially by following the soliton paradigm. Namely, the “singular solution content” of a given initially continuous distribution of velocity emerges under the evolution of EPDiff and retains its integrity under collision interactions. In 1d, these singular solutions are true solitons (the peakons) for the dispersionless CH shallow water equation. In this case, the inverse scattering transform for CH determines its soliton content for an arbitrary initial condition and also gives the soliton collision rules. In 2d and 3d, the theory for determining how these singular solutions will emerge and how they will survive their collisions has not yet been developed. This is the major open problem for EPDiff. One clue for approaching it is to keep in mind that the singular solutions in (3) form an *invariant manifold* for the EPDiff equations.

Our numerical findings. We studied the initial value problem for EPDiff in various scenarios in 2d and 3d. We found that the key solution behavior of the IVP for EPDiff is the breakup of an initially smooth confined velocity distribution into singular solutions supported on codimension-one delta function densities moving with the velocity of the flow. We extended the solution ansatz for peakon momentum density supported on points on the line to the case of singular momentum density supported on smoothly embedded sets, e.g. curves in the plane, or surfaces in three dimensional space. We showed that this singular solution ansatz for EPDiff reduces to Hamilton’s canonical equations for the vector parameters defining these surfaces. The underlying geometrical reason why this reduction occurs was explained in Holm & Marsden [22] by recognizing that the singular solution ansatz (2) is a momentum map for the (right) action of diffeomorphisms on distributions defined as smoothly embedded subspaces of a manifold. Thus, the singular solutions evolve by Ad^* action on embedded subspaces along a curve $g(t)$ in the diffeomorphisms which is a geodesic path. As we explained, such a curve is a geodesic if and only if the corresponding momentum satisfies the EPDiff equation (1).

Remarkably, our numerical results showed that only the codimension-one singular solutions emerge in the IVP. Being defined on delta functions, these solutions have no internal degrees of freedom. Consequently, their local interactions may be characterized as elastic collisions of contact surfaces in which momentum is exchanged. Across these contact surfaces, the slope of the velocity has a jump which moves with the flow. The collision rules for

these interactions in 2d and 3d may be built up from the soliton collision rules in 1d. That is, a linear section transverse to a 2d solution shows 1d elastic momentum exchange behavior, and a planar section transverse to a 3d solution shows the corresponding 2d behavior. This reduction to lower dimensional behavior holds especially well on reflection-invariant sections. For example, the midplane $z = 0$ is invariant in Figure 78 and the motion in this plane projected on the bottom panel of Figure 78 mimics the motion observed in the corresponding 2d problem in Figure 55.

Thus, 3d numerical results have planar slices which show the corresponding 2d momentum transfer behavior. Likewise, 2d numerical results have linear slices which show the corresponding 1d momentum transfer behavior. Such a reduction principle allows the complex interactions of contact wave surfaces to be analyzed as elastic collisions showing local momentum transfer. This principle for collective behavior based on simple momentum exchange in collision interactions arises for the singular solutions, because such solutions possess no internal degrees of freedom.

Two new numerical features emerge in 2d and 3d. These are the reconnections of the wavefronts, which occur due to momentum exchange in these nonlinear collisions, and the remarkable “memory wisps” that arise to guarantee reversibility of those collisions. (These memory wisps are a bit reminiscent of the emission of neutrinos, which preserve detailed balance in beta decay.) The memory wisp feature of the reconnections remains to be explained in more detail, both numerically and analytically.

EPDiff applications: solitons, turbulence and medical images. From the viewpoint of nonlinear PDE analysis, the EPDiff equation, being nonlinear and nonlocal, escapes classification. Its nonlocality requires solving an elliptic problem for determining its velocity from its momentum at each time step. It’s worth repeating that the EPDiff nonlinearity is geometric, because this is the key to understanding its motion. Namely, it is reversible geodesic motion in the diffeomorphisms acting on smoothly embedded subspaces. Physically, the singular solutions are contact surfaces (jumps in the velocity derivative that move with the flow). The corresponding EPDiff equation on the volume-preserving diffeomorphisms is the Lagrangian Averaged Euler (LAE- α) equation derived first in [23], which was first derived as a geometrical extension of the CH equation. Upon adding Navier-Stokes viscosity, this became the LANS- α model for incompressible turbulence in

[9]. For a review of the properties of LANS- α solutions and their relation to Navier-Stokes analysis, see [16] and [44].

By a remarkable coincidence, L. Younes derived the EPDiff equation (1) as the evolution for the template matching approach in medical imaging in [52]. See also D. Mumford's discussion of the same problem in [48]. Thus, the singular solutions we discuss here, and their momentum exchange paradigm, should be expected to develop increasing interest in medical imaging science. Medical imaging must solve an optimization problem rather than the IVP. However, our solution of the IVP may help guide intuition in medical imaging, especially the idea of encoding information in an image by its momentum, rather than just by the positions of its outlines and their associated intensities. Thus, EPDiff represents a crossroads of endeavor in mathematics where methods of fluid dynamics and imaging science may transfer technologies. See [27] for more discussions of this new paradigm in image processing.

Many open questions remain. Many open problems and other future applications remain for the EPDiff equation. For example, its analysis requires additional developments of PDE methods. In particular, while its smooth solutions satisfy a local existence theorem analogous to the Ebin-Marsden theorem for the Euler fluid equations, its IVP inevitably develops singular solutions. The implications of this observation are mentioned in [22] as perhaps indicating an incompleteness of the geodesic flows on the diffeomorphisms, which opens many future opportunities for analysis of the emergence of measure valued solutions from smooth initial conditions in non-linear nonlocal PDEs.

In addition, many open questions remain for the practical problem of internal wavefronts emerging in shallow water dynamics. For example, there remains the issues of boundary and topography interactions, including diffraction and refraction. Moreover, for the applications in turbulence modeling there remains a variety of open questions about singular vortex interactions, which are responsible for the famous vortex stretching that drives the cascade of energy and vorticity in turbulence. A host of other problems also remains for the applications of EPDiff in medical imaging, particularly for the statistical treatment of the information encoded in the linear space of their momenta. Finally, the development of numerical approaches that are fully capable of tracking the singular solutions of EPDiff, perhaps by using geometrical methods which incorporate discrete exterior calculus and varia-

tional multisymplectic integration methods. See [12] and [36] for descriptions of these promising methods, which seem to lie on the horizon for the next applications of singular solutions.

Acknowledgements

We are grateful to many friends and colleagues for their enormous help and encouragement during the course of this work. These include R. Lowrie and B. A. Wingate, whose encouragement inspired the beginning of this endeavor in the context of Lagrangian averaged models of turbulence. We are also grateful to R. Camassa, A. Hirani, M. Leok, S. T. Li, J. E. Marsden, M. I. Miller, T. Ratnanather, and L. Younes for helpful discussions and challenging observations. Finally, we thank the Los Alamos Turbulence Working Group (TWG) and the members of the TWG external advisory committee for continuing discussions, challenges, and encouragement.

This work was supported by the United States Department of Energy under contracts W-7405-ENG-36 and the Applied Mathematical Sciences Program KC-07-01-01. We are also grateful for partial funding from Applied Mathematical Sciences Division, Office of Advanced Scientific Computing Research, DOE Office of Science.

References

- [1] This process may be extended to higher moments, at the cost of introducing additional variables, which we decline.
- [2] Note: The top and bottom boundary conditions influence stability characteristics.
- [3] Contributions arising when integrating by parts vanish, upon requiring the usual condition that the fluid velocities and their variations are tangential to the fixed horizontal boundaries.

- [4] The interfacial velocities \dot{h}_i appear in the variational derivatives of the Lagrangian ℓ explicitly as

$$\begin{aligned} \frac{1}{\rho_i D_i} \frac{\delta \ell}{\delta \mathbf{u}_i} &= \mathbf{u}_i + \frac{1}{D_i} \nabla \frac{D_i^2}{6} (2\dot{h}_i + \dot{h}_{i+1}) \\ &+ \frac{1}{2} (\dot{h}_i + \dot{h}_{i+1}) \nabla h_{i+1} + \nabla \sum_{j=1}^{i-1} \frac{D_j}{2} (\dot{h}_j + \dot{h}_{j+1}), \\ \frac{1}{\rho_i} \frac{\delta \ell}{\delta D_i} &= \frac{1}{2} \dot{h}_i^2 + \sum_{j=1}^{i-1} \left[\frac{1}{2} (\dot{h}_j^2 - \dot{h}_{j+1}^2) \right. \\ &\left. + (\mathbf{u}_i - \mathbf{u}_j) \cdot \nabla \frac{D_j}{2} (\dot{h}_j + \dot{h}_{j+1}) \right] + \frac{1}{2} |\mathbf{u}_i|^2 - g H_i. \end{aligned}$$

- [5] S.V. Bazdenkov, N.N. Morozov and O.P. Pogutse, 1985, Dispersive effects in two-dimensional hydrodynamics. *Dokl. Akad. Nauk SSSR* **293**, 818-822; [*Sov. Phys. Dokl.* **32**, 262-264].
- [6] R. Camassa and D. D. Holm, An Integrable Shallow Water Equation with Peaked Solitons. *Phys. Rev. Lett.* **71** (1993) 1661-1664.
- [7] R. Camassa, D. D. Holm and C. D. Levermore, Long-time effects of bottom topography in shallow water. *Physica D* **98** (1996) 258-286.
- [8] J. G. Charney and P. G. Drazin, Propagation of planetary scale disturbances from the lower into the upper atmosphere. *J. Geophys. Res.* **66** (1961) 83-109.
- [9] S.Y. Chen, C. Foias, E.J. Olson, E.S. Titi and S. Wynne, The Camassa-Holm equations as a closure model for turbulent channel and pipe flows. *Phys. Rev. Lett.* **81** (1998) 5338-5341.
- [10] W. Choi and R. Camassa, Long internal waves of finite amplitude. *Phys. Rev. Lett.* **77** (1996) 1759.
- [11] W. Choi and R. Camassa, Fully nonlinear internal waves in a two-fluid system. *J. Fluid Mech.* **396** (1999) 1-36.
- [12] Desbrun, M., A. N. Hirani, M. Leok and J. E. Marsden [2003], Discrete exterior calculus, (*preprint*).

- [13] H. R. Dullin, G. A. Gottwald and D. D. Holm, An integrable shallow water equation with linear and nonlinear dispersion. *Phys. Rev. Lett.* **87** (2001) 194501-04.
- [14] H. R. Dullin, G. A. Gottwald and D. D. Holm, Camassa-Holm, Korteweg-de Vries-5 and other asymptotically equivalent equations for shallow water waves. *Fluid Dyn. Res.* **33** (2003) 73-95.
- [15] H. R. Dullin, G. A. Gottwald and D. D. Holm, On asymptotically equivalent shallow water wave equations. *Physica D* **190** (2004) 1-14.
- [16] C. Foias, D. D. Holm and E. S. Titi, The Navier-Stokes-alpha model of fluid turbulence. *Physica D* **152** (2001) 505-519.
- [17] M.F. Gobbi, J.T. Kirby and G. Wei, A fully nonlinear Boussinesq model for surface waves. Part 2. Extension to $O(kh)^4$. *J. Fluid Mech.* **405** (2000) 181-210.
- [18] A. E. Green and P. M. Naghdi, A derivation of equations for wave propagation in water of variable depth. *J. Fluid Mech.* **78** (1976) 237-246.
- [19] A. N. Hirani, Discrete Exterior Calculus. Caltech Ph.D. thesis, 2003. <http://resolver.caltech.edu/CaltechETD:etd-05202003-095403>.
- [20] D. D. Holm, Hamiltonian structure for two-dimensional hydrodynamics with nonlinear dispersion. *Phys. Fluids* **31** (1988) 2371-2373.
- [21] D. D. Holm, Variational multilayer Green-Naghdi fluid equations. In preparation.
- [22] D. D. Holm and J. E. Marsden, Momentum Maps and Measure-valued Solutions (Peakons, Filaments and Sheets) for the EPDiff Equation. In *The Breadth of Symplectic and Poisson Geometry*, (Marsden, J. E. and T. S. Ratiu, eds), Festschrift for Alan Weinstein. Birkhäuser Boston, to appear.
- [23] D. D. Holm, J. E. Marsden and T. S. Ratiu, The Euler-Poincaré equations and semidirect products with applications to continuum theories. *Adv. in Math.*, **137** (1998) 1-81
- [24] D. D. Holm, J. E. Marsden, T. Ratiu and A. Weinstein, Nonlinear stability of fluid and plasma equilibria. *Physics Reports* **123** (1985) 1-116.

- [25] D. D. Holm, J. Munn and S. N. Stechmann, Reduced singular solutions of EPDiff equations on manifolds with symmetry. In preparation for *Nonlinearity*.
- [26] D. D. Holm, V. Putkaradze and S. N. Stechmann, Rotating concentric peakons. Submitted to *Nonlinearity*.
- [27] D. D. Holm, T. Ratnanather, A. Trouvé and L. Younes, Soliton dynamics in computational anatomy, *NeuroImage* (2004), To appear.
- [28] D. D. Holm and M. F. Staley, Wave Structures and Nonlinear Balances in a Family of Evolutionary PDEs. *SIAM J. Appl. Dyn. Syst.* **2** (3) (2003) 323-380.
- [29] M.-K. Hsu and A. K. Liu, Nonlinear Internal Waves in the South China Sea. *Canadian J. Rem. Sens.* **26** (2000) 72–81.
- [30] J. K. Hunter and R. H. Saxton, Dynamics of director fields. *SIAM J. Appl. Math.* **51** (1991) 1498-1521.
- [31] J. M. Hyman and M. Shashkov, *The Adjoint Operators for the Natural Discretizations of the Divergence, Gradient, and Curl on Logically Rectangular Grids*, IMACS J. Appl. Num. Math., 25, pp. 413–442 (1997).
- [32] Institute for Mathematics and its Applications (IMA) “Hot Topics” Workshop: Compatible Spatial Discretizations for Partial Differential Equations, May 11-15, 2004. <http://www.ima.umn.edu/complex/spring/discretization.html>.
- [33] B. Khesin and G. Misiolek, Euler equations on homogeneous spaces and Virasoro orbits. *Adv. Math.* **176** (2003) 116-144.
- [34] S. Kouranbaeva, The Camassa-Holm equation as a geodesic flow on the diffeomorphism group. *J. Math, Phys.* **40** (1999) 857-868.
- [35] M. Leok, Foundations of Computational Geometric Mechanics. Caltech Ph.D. thesis, 2004. <http://resolver.caltech.edu/CaltechETD:etd-03022004-000251>.
- [36] Lew, A., J. E. Marsden, M. Ortiz and M. West [2003], Asynchronous variational integrators, *Archive for Rat. Mech. An.* **167**, 85–146.

- [37] S. T. Li, private communication.
- [38] R. Liska, L. Margolin and B. Wendroff, Nonhydrostatic two-layer models of incompressible flow. *Computers Math. Applics.* **29** (1995) 25-37.
- [39] R. Liska and B. Wendroff, Analysis and computation with stratified fluid models. *J. Comp. Phys.* **137** (1997) 212-244.
- [40] A. K. Liu, Y. S. Chang, M.-K. Hsu, N. K. Liang, Evolution of nonlinear internal waves in the east and south China Seas. *J. Geophys. Res.* **103** (1998) 7995-8008.
- [41] P. J. Lynett and P. L.-F. Liu, A two-dimensional, depth-integrated model for internal wave propagation over variable bathymetry. *Wave Motion* **36** (2002) 221-240.
- [42] P. A. Madsen and Y. Agnon, Accuracy and convergence of velocity formulations for water waves in the framework of Boussinesq theory. *J. Fluid Mech.* **477** (2003) 285-319.
- [43] L. G. Margolin, B. T. Nadiga and P. K. Smolarkiewicz, Various approximations of the shallow flow over an obstacle. *Phys. Fluids* 1996.
- [44] J. E. Marsden and S. Shkoller Global well-posedness for the Lagrangian averaged Navier-Stokes (LANS- α) equations on bounded domains. *Phil. Trans. R. Soc. Lond. A* **359** (2001) 1449-1468.
- [45] J. Miles and R. Salmon, Weakly dispersive nonlinear gravity waves. *J. Fluid Mech.* **157** (1985) 519-531.
- [46] M. I. Miller, A. Trouné and L. Younes, On the metrics and Euler-Lagrange equations of computational anatomy. *Ann. Rev. Biomed. Engin.* **4** (2002) 375-405.
- [47] G. Misiolek, A shallow water equation as a geodesic flow on the BottVirasoro group. *J. Geom. Phys.* **24** (1998) 203-208.
- [48] D. Mumford, Pattern theory and vision. In *Questions Mathématiques En Traitement Du Signal et de L'Image*, chapter 3, pages 7-13. Institut Henri Poincaré, Paris, 1998.
- [49] J. Pedlosky, *Geophysical Fluid dynamics*. Springer (1987).

- [50] C. H. Su and C. S. Gardner, Korteweg-de Vries Equation and Generalizations. III. Derivation of the Korteweg-de Vries Equation and Burgers Equation. *J. Math. Phys.* **10** (1969) 536-539.
- [51] G. B. Whitham, Variational methods and applications to water waves. *Proc. R. Soc. London, Ser. A* **299** (1967) 6.
- [52] L. Younes, Computable elastic distances between shapes. *SIAM J. Appl. Math.* **58** (1998) 565-586
- [53] J. Ziegenbein, Spatial observations of short internal waves in the Strait of Gibraltar. *Deep Sea Res.* **17** (1970) 867-875.